

# **Acid Leaching of SHS Produced MgO/TiB<sub>2</sub>**

By

Jonathan Y. Lok

Thesis submitted to the Faculty of the  
Virginia Polytechnic Institute and State University  
in partial fulfillment of the requirements for the degree of

Master of Science

In

Materials Science and Engineering

APPROVED:

Dr. Kathryn V. Logan, Chair

Dr. Stephen L. Kampe

Dr. Gary R. Pickrell

October 10, 2006

Blacksburg, Virginia

Keywords: Acid Leaching, Titanium Diboride, Magnesium Oxide, Thermite Reaction

# Acid Leaching of SHS Produced MgO/TiB<sub>2</sub>

Jonathan Y. Lok

## ABSTRACT

The stoichiometric Self-propagating High-temperature Synthesis (SHS) thermite reaction involving magnesium oxide (MgO), titanium dioxide (TiO<sub>2</sub>), and boron oxide (B<sub>2</sub>O<sub>3</sub>) forms titanium diboride (TiB<sub>2</sub>) and MgO as final products. Selective acid leaching is used to remove the MgO leaving high purity TiB<sub>2</sub> powder. The SHS method to produce TiB<sub>2</sub> is attractive because of the relatively low temperature required to initiate the reaction, fast reaction time, and product purity. This study investigates the acid leaching of SHS produced MgO/TiB<sub>2</sub> and a stoichiometric mixture of commercial MgO and TiB<sub>2</sub> powders. Leaching was conducted at 90°C, 60°C, and 30°C at pH levels of 4.0, 2.5, and 1.0 by introduction of concentrated aliquots of HNO<sub>3</sub>. This method maintains a minimum pH target throughout the leaching process, thereby sustaining a dynamic concentration to remove the oxide. The optimal leaching conditions were determined to be at 90°C at a minimum pH target of 2.5 for the SHS produced product. At these conditions, conversion percentages of 83%-84% of MgO were measured with only trace amounts of TiB<sub>2</sub> measured in the solution (less than 100 ppm). Conversion percentages for each leaching condition and dissolution mass of solid MgO and TiB<sub>2</sub> at each pH are also reported. Results from powder XRD confirm the removal of MgO and minimal dissolution of TiB<sub>2</sub>, and indicate the formation of unidentified compounds. Inductively coupled plasma mass spectrometry (ICP) was used to analyze the ionic composition and extent of leaching. Scanning electron microscopy (SEM) was used to observe the particle morphology of the leached powders.

Dedicated to my wife and our future family

## Acknowledgements

Milestones are rarely accomplished without the contributions, support, and generosity of others along the way. This project was an undertaking of which one university, a research institution, a national laboratory, a government agency, and countless individuals influenced the direction this work would take. Because of such diversity, acknowledgements and thankyou's are more numerous than usual. To each individual I have come across through the course of the project, I offer my gratitude, whether mentioned in the following or in passing.

I would like to thank my advisor, Dr. Kathryn Logan for allowing me to work at some of the most visible places for materials research. My formal academic career concludes on a high note, influenced by her revered optimism and pleasure sought out of life. I would like to thank the National Institute of Aerospace for providing the infrastructure and research environment, and the NASA Langley Research Center for the analytical tools to complete my thesis. The Applied Research Center at Jefferson National Labs opened their laboratory facilities and accommodated our experimental needs. Without these working in concert, this work would not be possible.

I am grateful to Dr. Stephen Kampe for his encouragement and assistance during the early stages of adapting to the academic realm from the working world. I am also thankful to Dr. Gary Pickrell for taking the time to serve as part of my committee. To the department head, Dr. David Clark and the rest of the MSE faculty, thank you for allowing me to attend such a fine institution to complete my graduate work.

At the NIA, I would like to thank Dr. Robert Lindberg and the founders of the institution for their pioneering spirit in bringing six member universities together. Anton Schuszler of the Metals and Thermal Structures Branch at the LaRC made his staff available for analytical expertise. I would like to include Dr. Michael Kelley at the College of William & Mary for his guidance during the experimental portion of this work, and for making our presence possible at Jefferson Labs.

Personal relationships played a large role in the past two years. I would like to especially like to thank Jairaj Payyapilly who always found the time and patience to help me in my transition into materials science. As well as being a good friend, his influence is found throughout this project. Dr. Carlos Suchicital, Sharon Jefferies, Brad Hopkins, and the rest of the Multi-functional Aerospace Materials Research Group (MAMRG) provided the support and structure of a research group.

My new and loving wife, Elizabeth, was a constant source of encouragement and provided strength at a time when newlyweds typically have other priorities. She was the steady force that saw this project to the end. To my brother Benjamin, the professor, who helped me prepare for graduate school. I have a greater appreciation for what he does, and respectfully don't understand why. I send my thanks to my sister who maintains our childhood closeness on the opposite coast. Finally, to my parents, who support all I do, big or small, great or mundane, their unconditional support keeps me balanced and loving life.

## Table of Contents

ABSTRACT.....	ii
Acknowledgements.....	iv
Table of Contents.....	v
List of Figures.....	vii
List of Tables.....	x
1 CHAPTER ONE – GENERAL INTRODUCTION.....	1
2 CHAPTER TWO – LITERATURE REVIEW.....	3
2.1 Introduction.....	3
2.2 Synthesis of TiB <sub>2</sub> .....	3
2.2.1 Carbothermic / Borothermic Reduction.....	3
2.2.2 Self-Propagating High-Temperature Synthesis (SHS) Thermite Reactions.....	5
2.2.3 Other Methods of TiB <sub>2</sub> Synthesis.....	8
2.3 Leaching.....	9
2.3.1 Leaching Candidates.....	9
2.3.2 Dissolution of MgO in Acid and Kinetic Models.....	10
2.3.4 Hydration of MgO.....	13
2.4 Purification of Borides.....	15
3 CHAPTER THREE – EXPERIMENTAL PROCEDURE.....	17
3.1 Introduction.....	17
3.2 Particle Size and Morphology of Stock Powders.....	17
3.3 Synthesis.....	18
3.4 Processing.....	19
3.5 Testing.....	20
3.5.1 Candidate Selection.....	20
3.5.2 Leaching by Minimum pH.....	21
3.5.2.1 Experimental Design.....	23
3.6 Characterization.....	25
3.6.1 ICP-MS.....	25
3.6.2 SEM/EDS.....	25
3.6.3 XRD.....	26
3.7 Materials and Equipment Used.....	26
3.7.1 Synthesis.....	26
3.7.2 Processing.....	28
3.7.3 Testing.....	28
4 CHAPTER FOUR – RESULTS AND DISCUSSION.....	30
4.1 Extent of Ball Milling.....	30
4.1 Commercial Stoichiometric Mixture.....	31
4.1.1 Percent Conversion and Dissolution of Products.....	31
4.1.2 SEM.....	33
4.2 SHS Produced MgO/TiB <sub>2</sub> .....	35
4.2.1 Percent Conversion and Dissolution of Products.....	35
4.2.2 SEM/EDS.....	40
4.2.3 XRD.....	51
4.3 Qualitative Comparisons.....	53
4.3.1 D(pH)/Dt.....	53

4.3.2	Average pH .....	55
5	CHAPTER FIVE – CONCLUSIONS AND FUTURE WORK .....	58
5.1	Optimal Dissolution of MgO and TiB <sub>2</sub> .....	58
5.2	Leaching Dynamics of SHS produced MgO/TiB <sub>2</sub> .....	58
5.3	Proposed Future Work .....	58
	APPENDIX .....	60
A.1	SEM .....	60
A.1.1	Stock Powders .....	60
A.1.2	Ball Milling .....	63
A.1.3	Leaching Results .....	66
A.2	Particle Size Analysis .....	79
A.3	XRD .....	80
A.4	pH Strip Charts .....	81
	REFERENCES .....	89

## List of Figures

Figure 1: Oscillatory pH in response to addition of acid is characteristic of a buffer solution [9].....	21
Figure 2: Leaching process including solids separation.....	22
Figure 3: Reaction chamber lined with refractory brick and walls.....	27
Figure 4: (left) NiCr wire just touching powders (right) product removed from crucible	27
Figure 5: Stages of 38.9g Mg SHS thermite reaction. (left) NiCr glowing red, ~4.8V (center) SHS reaction initiated, ~7.2V-9.6V (right) Reaction completed.....	28
Figure 6: (left) Acid leaching setup (right) Vacuum-assisted filtration.....	29
Figure 7: SEM Micrograph of dried MgO/TiB <sub>2</sub> as-reacted powders.....	30
Figure 8: After 18 hours of milling, MgO/TiB <sub>2</sub> agglomerates have been reduced.....	31
Figure 9: Stoichiometric MgO Conversion in HNO <sub>3</sub> in low and high pH conditions.....	32
Figure 10: Conversion percentage of stoichiometric mixture of commercial MgO and TiB <sub>2</sub> based on ICP-MS data during leaching.....	33
Figure 11: Commercial TiB <sub>2</sub> leached at minimum pH of 4.0 at 90°C.....	34
Figure 12: Commercial TiB <sub>2</sub> leached at minimum pH of 2.5 at 90°C.....	34
Figure 13: Commercial TiB <sub>2</sub> leached at minimum pH of 1.0 at 90°C.....	35
Figure 14: Conversion percentage of SHS produced MgO/TiB <sub>2</sub> from ICP-MS.....	36
Figure 15: Conversion of TiB <sub>2</sub> from leaching commercial and SHS powders at 90°C....	36
Figure 16: D(pH)/Dt curves of pH 4.0 and 2.5 second cycle plotted versus relative MgO moles.....	39
Figure 17: Percent dissolution of SHS Produced TiB <sub>2</sub> during second leaching cycle.....	40
Figure 18: As-milled SHS MgO/TiB <sub>2</sub> prior to leaching - 50,000x.....	41
Figure 19: As-milled SHS MgO/TiB <sub>2</sub> prior to leaching - 100,000x.....	41
Figure 20: SHS TiB <sub>2</sub> leached at minimum pH 4.0 at 90°C – 10,000x.....	42
Figure 21: SHS TiB <sub>2</sub> leached at minimum pH 4.0 at 90°C - 100,000x.....	42
Figure 22: SHS TiB <sub>2</sub> leached at minimum pH 4.0 at 90°C - Second Cycle – 50,000x....	43
Figure 23: SHS TiB <sub>2</sub> leached at minimum pH 4.0 at 90°C - Second Cycle – 100,000x..	43
Figure 24: EDS spectra of SHS TiB <sub>2</sub> leached at minimum pH 4.0 at 90°C.....	44
Figure 25: SHS TiB <sub>2</sub> leached at minimum pH 2.5 at 90°C – 50,000x.....	45
Figure 26: SHS TiB <sub>2</sub> leached at minimum pH 2.5 at 90°C – 100,000x.....	45
Figure 27: SHS TiB <sub>2</sub> leached at minimum pH 2.5 at 90°C – Second Cycle– 50,000x....	46
Figure 28: SHS TiB <sub>2</sub> leached at minimum pH 2.5 at 90°C – Second Cycle – 100,000x..	46
Figure 29: EDS spectra of SHS TiB <sub>2</sub> leached at minimum pH 2.5 at 90°C.....	47
Figure 30: SHS TiB <sub>2</sub> leached at minimum pH 1.0 at 90°C – 50,000x.....	48
Figure 31: SHS TiB <sub>2</sub> leached at minimum pH 1.0 at 90°C – 100,000x.....	48
Figure 32: SHS TiB <sub>2</sub> leached at minimum pH 1.0 at 90°C – Second Cycle – 50,000x...	49
Figure 33: SHS TiB <sub>2</sub> leached at minimum pH 1.0 at 90°C – Second Cycle – 100,000x..	49
Figure 34: EDS spectra of SHS TiB <sub>2</sub> leached at minimum pH 1.0 at 90°C.....	50
Figure 35: Powder x-ray diffraction scan for minimum pH 4.0 leaching.....	51
Figure 36: Powder x-ray diffraction scan for minimum pH 2.5 leaching.....	52
Figure 37: Powder x-ray diffraction scan for minimum pH 1.0 leaching.....	52
Figure 38: D(pH)/Dt for all powders at 90C. Indicated with arrows, the single-hashed and double-hashed lines represent leaching of commercial MgO-only at pH 4.0 and pH of 1.0, respectively.....	54
Figure 39: Average pH for minimum pH levels 2.5 and 1.0 including second cycle.....	56

Figure 40: Average pH for minimum pH level 4.0 including second cycle .....	56
Figure 41: SHS reactant Mg flake at 650x magnification .....	60
Figure 42: SHS reactant amorphous B <sub>2</sub> O <sub>3</sub> at 300x magnification .....	61
Figure 43: SHS reactant pigment grade TiO <sub>2</sub> at 15,000x magnification .....	61
Figure 44: Commercial carbothermic TiB <sub>2</sub> from H.C. Starck at 7,000x magnification...	62
Figure 45: Commercial MgO used in stoichiometric mixture at 2,000x magnification...	62
Figure 46: As-reacted MgO/TiB <sub>2</sub> at 100x magnification .....	63
Figure 47: As-reacted MgO/TiB <sub>2</sub> at 5,000x magnification .....	64
Figure 48: As-reacted MgO/TiB <sub>2</sub> at 50,000x magnification .....	64
Figure 49: As-reacted MgO/TiB <sub>2</sub> milled for 18 hours at 100x magnification.....	65
Figure 50: As-reacted MgO/TiB <sub>2</sub> milled for 18 hours at 5,000x magnification.....	65
Figure 51: As-reacted MgO/TiB <sub>2</sub> milled for 18 hours at 50,000x magnification.....	66
Figure 52: SHS MgO/TiB <sub>2</sub> – min pH 4.0 at 90°C at 500x magnification .....	67
Figure 53: SHS MgO/TiB <sub>2</sub> – min pH 4.0 at 90°C at 10,000x magnification .....	67
Figure 54: SHS MgO/TiB <sub>2</sub> – min pH 4.0 at 90°C at 100,000x magnification .....	68
Figure 55: SHS MgO/TiB <sub>2</sub> – min pH 4.0 at 90°C at 500x magnification – 2 <sup>nd</sup> Cycle .....	68
Figure 56: SHS MgO/TiB <sub>2</sub> – min pH 4.0 at 90°C at 10,000x magnification – 2 <sup>nd</sup> Cycle .....	69
Figure 57: SHS MgO/TiB <sub>2</sub> – min pH 4.0 at 90°C at 100,000x magnification – 2 <sup>nd</sup> Cycle .....	69
Figure 58: SHS MgO/TiB <sub>2</sub> – min pH 2.5 at 90°C at 500x magnification .....	70
Figure 59: SHS MgO/TiB <sub>2</sub> – min pH 2.5 at 90°C at 10,000 magnification .....	70
Figure 60: SHS MgO/TiB <sub>2</sub> – min pH 2.5 at 90°C at 100,000x magnification .....	71
Figure 61: SHS MgO/TiB <sub>2</sub> – min pH 2.5 at 90°C at 500x magnification – 2 <sup>nd</sup> Cycle .....	71
Figure 62: SHS MgO/TiB <sub>2</sub> – min pH 2.5 at 90°C - 10,000x magnification – 2 <sup>nd</sup> Cycle ..	72
Figure 63: SHS MgO/TiB <sub>2</sub> – min pH 2.5 at 90°C - 100,000x magnification – 2 <sup>nd</sup> Cycle ..	72
Figure 64: SHS MgO/TiB <sub>2</sub> – min pH 1.0 at 90°C - 500x magnification.....	73
Figure 65: SHS MgO/TiB <sub>2</sub> – min pH 1.0 at 90°C – 10,000x magnification .....	73
Figure 66: SHS MgO/TiB <sub>2</sub> – min pH 1.0 at 90°C – 100,000x magnification .....	74
Figure 67: SHS MgO/TiB <sub>2</sub> – min pH 1.0 at 90°C - 500x magnification – 2 <sup>nd</sup> Cycle.....	74
Figure 68: SHS MgO/TiB <sub>2</sub> – min pH 1.0 at 90°C – 10,000x magnification – 2 <sup>nd</sup> Cycle ..	75
Figure 69: SHS MgO/TiB <sub>2</sub> – min pH 1.0 at 90°C – 100,000x magnification – 2 <sup>nd</sup> Cycle ..	75
Figure 70: Commercial Powders – min pH 4.0 at 90°C - 500x magnification.....	76
Figure 71: Commercial Powders – min pH 4.0 at 90°C – 10,000x magnification .....	76
Figure 72: Commercial Powders – min pH 2.5 at 90°C – 500x magnification .....	77
Figure 73: Commercial Powders – min pH 2.5 at 90°C – 10,000x magnification .....	77
Figure 74: Commercial Powders – min pH 1.0 at 90°C – 500x magnification .....	78
Figure 75: Commercial Powders – min pH 1.0 at 90°C – 10,000x magnification .....	78
Figure 76: Mg flake particle size distribution from certificate of analysis.....	79
Figure 77: Amorphous B <sub>2</sub> O <sub>3</sub> particle size distribution .....	79
Figure 78: Pigment grade TiO <sub>2</sub> particle size distribution .....	79
Figure 79: Summary of all scans with respect to diffraction scan of as-reacted SHS product .....	80
Figure 80: SHS MgO/TiB <sub>2</sub> leaching strip chart for minimum pH 4.0 at 90°C.....	81
Figure 81: SHS MgO/TiB <sub>2</sub> leaching strip chart for minimum pH 4.0 at 90°C – 2 <sup>nd</sup> Cycle .....	82
Figure 82: SHS MgO/TiB <sub>2</sub> leaching strip chart for minimum pH 2.5 at 90°C.....	82

Figure 83: SHS MgO/TiB <sub>2</sub> leaching strip chart for minimum pH 2.5 at 90°C – 2 <sup>nd</sup> Cycle	83
Figure 84: SHS MgO/TiB <sub>2</sub> leaching strip chart for minimum pH 1.0 at 90°C	83
Figure 85: SHS MgO/TiB <sub>2</sub> leaching strip chart for minimum pH 1.0 at 90°C – 2 <sup>nd</sup> Cycle	84
Figure 86: Commercial powder leaching strip chart for minimum pH 4.0 at 90°C	84
Figure 87: Commercial powder leaching strip chart for minimum pH 4.0 at 60°C	85
Figure 88: Commercial powder leaching strip chart for minimum pH 4.0 at 30°C	85
Figure 89: Commercial powder leaching strip chart for minimum pH 2.5 at 90°C	86
Figure 90: Commercial powder leaching strip chart for minimum pH 2.5 at 60°C	86
Figure 91: Commercial powder leaching strip chart for minimum pH 2.5 at 30°C	87
Figure 92: Commercial powder leaching strip chart for minimum pH 1.0 at 90°C	87
Figure 93: Commercial powder leaching strip chart for minimum pH 1.0 at 60°C	88
Figure 94: Commercial powder leaching strip chart for minimum pH 1.0 at 30°C	88

## List of Tables

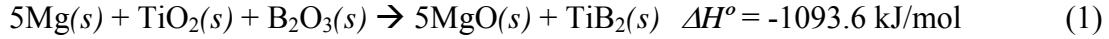
Table 1: Experimental matrices for minimum pH leaching.....	23
Table 2: Solubility properties calculated from handbook values [1].....	37
Table 3: $R^2$ values for $D(\text{pH})/Dt$ curves of pH 4.0 and 2.5 second leaching cycles.....	39
Table 4: $R^2$ values for $D(\text{pH})/Dt$ curves .....	54
Table 5: Constant pH settings corresponding to the minimum pH used in this work .....	57

# 1 CHAPTER ONE – GENERAL INTRODUCTION

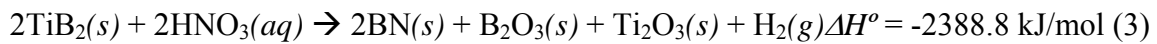
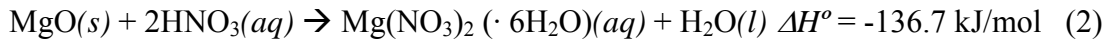
Titanium diboride ( $\text{TiB}_2$ ) is a refractory ceramic known for its high hardness, strength to density ratio, and wear resistance [23]. Potential applications include cutting tool inserts, wear resistant coatings, and ballistic armor. Industries are interested in  $\text{TiB}_2$  for the chemical/environmental passivity, tribological properties, electrical conductivity, and thermal shock resistance [40]. The aerospace community is interested in potentially using  $\text{TiB}_2$  in spacecraft hull design for micrometeoroid shielding. Petrochemical and refinery operations embed  $\text{TiB}_2$  into reactor linings to minimize wear from slurry unit operations. Military applications include  $\text{TiB}_2$  composites as ceramic armor that can withstand the impact from a long-rod penetrator.

Production reliability and quality control are foremost concerns in the fabrication of ceramics, especially refractory compounds. This is due to the variability in the parameters critical to the physical properties. Porosity, average particle size, and irregular particle shape can influence the end piece during powder pressing [6]. Thermite reactions use the thermal energy evolved from the exothermic reaction to drive the reaction to completion. A heat source is used to ignite the reactants which combust along a reaction wave front. The advantages in producing refractory materials via SHS thermite reactions are numerous. Self-sustaining energy generation from a relatively low energy input is an attractive alternative to the high energy costs of carbothermic/borothermic reduction [40]. Long reaction times and high energy requirements are characteristic of refractory materials. The relatively fast reaction times and product purity are other advantages in using thermite reactions to produce refractory ceramics. However, the potential for an uncontrolled reaction has limited the production of ceramics using SHS thermite reactions.

The magnesium thermite reaction produces stoichiometric amounts of  $\text{MgO}$  and  $\text{TiB}_2$  according to Equation 1. The as-reacted powders are made up of agglomerates with the  $\text{MgO}$  binding the hexagonal  $\text{TiB}_2$  platelets together [21]. Post reaction processing involves milling the agglomerates for acid leaching.



Acid leaching was performed with nitric acid. The interactions between MgO and HNO<sub>3</sub> are well studied. However, literature on nitric acid interactions with TiB<sub>2</sub> were absent, and therefore investigated with FactSage™ Thermochemical Software. The results from the software simulations are shown below.



Ideally, optimal acid leaching conditions will drive the solid MgO into solution, while minimizing the attack on TiB<sub>2</sub>.

The scope of this thesis is to define the conditions for leaching stoichiometric amounts of MgO/TiB<sub>2</sub> based on the SHS magnesium thermite reaction. Product conversion rates will be investigated at each temperature and pH combination. The results obtained will be compared to a commercial stoichiometric MgO/TiB<sub>2</sub> mixture.

The rest of the thesis is organized by the following:

Chapter two is a literature review on the synthesis of TiB<sub>2</sub>, SHS thermite reactions, and acid leaching. Concepts of dissolution, kinetics, and hydration are presented as well. Chapter three details the experimental procedures used for SHS MgO/TiB<sub>2</sub> production, post reaction processing, and acid leaching. Chapter four discusses the results from analytical methods used to characterize the samples from acid leaching. In addition to quantitative results, qualitative observations are discussed based on trend behavior. Chapter five presents the conclusions from this study and future directions this project may take.

## 2 CHAPTER TWO – LITERATURE REVIEW

### 2.1 Introduction

This chapter covers the state of the art in TiB<sub>2</sub> synthesis and acid leaching in three sections. The first section examines the prominent methods of synthesizing pure TiB<sub>2</sub>, covering carbothermic/borothermic reduction and SHS thermite reactions. The next section covers the literature on leaching. The last section looks into the purification of TiB<sub>2</sub> using three strong acids, HCl, H<sub>2</sub>SO<sub>4</sub>, and HNO<sub>3</sub>. Here, kinetics and mechanisms of dissolution are investigated, as they apply to particle size, temperature, and acid concentration.

### 2.2 Synthesis of TiB<sub>2</sub>

Carbothermic/borothermic reduction and SHS thermite reactions are prominent methods used to synthesize pure TiB<sub>2</sub>. Both methods will be discussed as well as the benefits and drawbacks of production on a commercial scale. Other methods such as solvothermal reduction, and reduction of titanium tetrahalide-boron halide will be discussed at the end of the section [5].

#### 2.2.1 Carbothermic / Borothermic Reduction

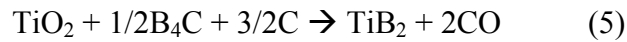
Carbothermic and borothermic reduction have been successfully used to produce TiB<sub>2</sub>. The carbothermic reduction of TiB<sub>2</sub> is the most prominent technique to produce TiB<sub>2</sub> on a commercial scale and is shown in Equation 4.



As written, the reaction is thermodynamically favorable from 1173-1923°C ( $\Delta H^\circ = 1250$  kJ/mol), but kinetically unfavorable. Powders are combined in a crucible and heated for about 15 hours. Above 2073°C, the powders react within one hour and the reacted mixture is allowed to cool to ambient temperature in argon to prevent oxidation of TiB<sub>2</sub>. CO is evolved during the reaction, leaving TiB<sub>2</sub> to be milled and sintered [19, 46].

Impurities from unreacted carbon can adversely affect the mechanical properties of the product which cannot easily be removed. The evolution of five moles of CO for every mole of TiB<sub>2</sub> produced is an environmental concern, further limiting its commercial viability.

The borothermic reduction method to synthesize TiB<sub>2</sub> is a two step process and is shown in Equation 5. Borothermic reduction takes place in the initial step, forming TiBO<sub>3</sub> and B<sub>2</sub>O<sub>3</sub> intermediates. The second step is a carbothermic reduction, forming TiB<sub>2</sub> and CO.



While B<sub>4</sub>C is a more valuable and costly commodity than B<sub>2</sub>O<sub>3</sub>, it is more thermodynamically favorable ( $\Delta H^\circ = -84$  kJ/mol) at 1400K and evolves less CO than the carbothermic reduction method [42].

The process of carbothermic and borothermic reduction to synthesize TiB<sub>2</sub> is energy intensive, but exhibits excellent control of the reaction dynamics. Pigment grade TiO<sub>2</sub>, carbon powder, and either boron carbide or boric anhydride powders are blended and pelletized with a volatile binder. After the mixing agents are evaporated, the powders are fed into a graphite furnace. The powders are heated to approximately 1400°C and then rapidly to 2000°C to initiate the carbothermic reduction. Argon is used as the inert atmosphere to prevent oxidation of TiB<sub>2</sub>. The resulting powders are agglomerates of TiB<sub>2</sub> crystallites that are milled to reduce prior to sintering [19].

The relatively long reaction times have been reduced by rapid carbothermal reduction by Saito *et al.* A powder precursor was made from H<sub>3</sub>BO<sub>3</sub> and TiO<sub>2</sub> with cornstarch as the source for carbon. The powders were fed into a vertical column, where the reactants contacted an argon atmosphere heated to 1786-1791°C. Subsequent exposure in a H<sub>2</sub> atmosphere for up to 18 hours was used to reduce the carbon content of the TiB<sub>2</sub> [30].

The relatively large energy cost and the evolution of CO have resulted in efforts to reduce TiO<sub>2</sub> by more economical means. Mechanical alloying is a low-energy, dry process that has been used to synthesize TiB<sub>2</sub>. With magnesium as the reducing agent,

TiO<sub>2</sub> (rutile) and boron oxide have been milled for up to 15 to 100 hours and leached with a 0.5M-1.0M HCl solution. Stoichiometric amounts of the reactant powders were used based on Equation 1. The reaction took place in evacuated jars and verified using DTA and TGA [28, 44, 45].

### 2.2.2 Self-Propagating High-Temperature Synthesis (SHS) Thermite Reactions

Thermite reactions are self-sustaining from the thermal energy released in the reaction. A heat source is used to ignite the reactants which combust along a reaction wave front. The reaction front progresses through the length of the reactant sample, and generates the necessary heat to propagate to completion. SHS thermite reactions are vigorous, but can be engineered to react in a controlled manner. The advantages in producing refractory materials via SHS thermite reactions are numerous. Self-sustaining energy generation from a relatively low energy input is an attractive alternative to the high energy costs of carbothermic/borothermic reduction. Refractory materials typically require hours of furnace firing, but time is significantly reduced with fast reaction times. However, because of the relatively large temperature gradients and heating and cooling rates, defect concentrations and nonequilibrium phases present challenges to this classification of reactions [22].

In the production of TiB<sub>2</sub> by SHS, there are two basic types of reactions, direct combination, and oxidation-reduction. The direct combination method to form TiB<sub>2</sub> follows the reaction below [21].



For this type of combination of binary systems, Munir and Subrahmanyam state the enthalpy of reaction can be determined from the adiabatic temperature,  $T_{ad}$ . This is the maximum theoretical temperature that the reactants reach, and determined from Equations 7 and 8. The latter equation applies to a phase change occurring between initial temperatures and  $T_{ad}$ .

$$\Delta H = \int_{298}^{T_{ad}} C_p dT \quad (7)$$

$$\Delta H = \int_{298}^{T_m} C_{p,solid} dT + \Delta H_f + \int_{T_m}^{T_{ad}} C_{p,liquid} dT \quad (8)$$

Under the adiabatic condition, one assumes a completely insulated and closed system. Equations 7 and 8 are used under the Kopp rule where the difference in enthalpies of the reactants and products due to temperature change is zero [12]. Thus, the  $T_{ad}$  is dependent on the enthalpy of the reaction and preheating of reactants.

Reactants are converted to products at the wave front as the reaction propagates through the sample. The exothermic nature of the reactions evolves the necessary heat to the unreacted powder ahead of the front through conduction. However, some heat is lost to the surroundings through convection and radiation. Therefore the adiabatic assumption is an approximation as the system strays from ideal conditions. This impacts the adiabatic temperature and actual conditions reveal maximum temperatures much less than  $T_{ad}$  [21, 39].

The magnesium thermite reaction is classified as a solid-liquid combustion system. This is defined by Subrahmanyam under the condition that one of the components ( $B_2O_3$ ) is in the liquid state at the time of combustion. The SHS of borides typically utilize solid-liquid reactions, with the metal element in the liquid state at  $T_{ad}$  ( $T_{mp}$  of magnesium =  $650^\circ C$ ,  $T_{ad} = 3350K$ ). In solid-liquid SHS systems, a low combustion temperature may be a result of an increase in metal particle size, and can cause incomplete conversion in SHS boride reactions. This is confirmed in the SHS production of TiC and TiN, where Shkiro reports the effect of increasing the metal particle size decreases the degree of conversion. According to Subrahmanyam, self-sustaining reactions come down to enthalpy, initial temperature, dilution, and particle size. Each affects the ability to achieve a homogeneous combustion front and a high degree of conversion [39].

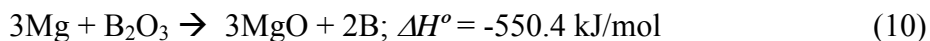
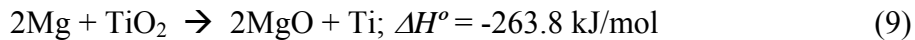
Subrahmanyam identifies several experimental factors pertaining to sample preparation that affect the SHS reaction. Non-stoichiometric mixtures decrease the achievable  $T_{ad}$ . Sample diameter is favorable if constant throughout the path of the reaction front, as heat loss could be facilitated by small sample diameters. The density, or porosity, of the powders changes the thermal conductivity and specific heat of the

sample as a whole. Oscillatory combustion or complete extinction of the reaction is possible if the reaction front encounters low density areas of the sample. If density is too high, or porosity too low, erratic reaction fronts are possible due to the rapid heat transfer away from the localized combustion zone. This also has an effect similar to a heating rate low enough where significant losses are present through conduction, convection, and radiation. As mentioned earlier, the effect of a particle size on combustion and degree of conversion is a parameter in boride systems, where an increase in metal particle size typically decrease  $T_{ad}$  [39].

The ignition of the powders can have a significant effect on the ability for the SHS reaction to self-sustain or compromise the degree of conversion. Rates of chemical reactions follow conventional Arrhenius kinetic behavior, where the exponential dependence on temperature is critical in SHS reactions. If the powders are heated slowly, the products form at a low rate, and a significant amount of heat is lost to the surroundings. This adversely impacts the  $T_{ad}$  by not fully utilizing the exothermicity of the reaction. With a sufficient heating rate, the thermal energy released further increases the temperature of the system, completing the self-sustaining reaction loop.

When the rate of reaction (rate of heat generation) exceeds the rate of heat loss to the environment, self-sustaining conditions are present. The ignition source must be able to raise the localized reactants to the ignition temperature that corresponds to the required heating rate, and must be rapid enough to prevent significant conversion of reactants prior to ignition [39].

Sundaram *et al.* have studied the reaction path of oxidation-reduction thermite reactions in the synthesis of pure  $TiB_2$  and  $Al_2O_3/TiB_2$  composites. The reaction path for the magnesium thermite reaction was studied in air and argon by ignition and by DTA on the following stoichiometric reactions.



The adiabatic temperatures for the above reactions were determined from the enthalpies of formation and latent heats of fusion as mentioned earlier.  $T_{ad}$  for the reactions above were 2210K, 2460K, and 3350K respectively [40].

In an argon atmosphere, DTA traces of Equation 11 show amorphous  $B_2O_3$  ( $T_{mp} = 450^\circ C$ ) having adequate time to flow between Mg and  $TiO_2$  by capillary action. This resulted in the formation of  $Mg_2TiO_4$  and  $Mg_3B_2O_6$ . Therefore the velocity of the reaction front is critical in the magnesium thermite reaction. From XRD analysis of Equation 11 in air, Mg and  $TiO_2$  in contact react, forming elemental Ti and MgO. Ti then reacted with amorphous  $B_2O_3$ , forming  $TiB_2$ . This is emphasized by the lack of Mg and  $B_2O_3$  reaction when heated to  $1200^\circ C$  in Equation 10 [40].

The intermediate step of the formation of elemental Ti and MgO from Mg and  $TiO_2$  in contact is critical in the subsequent formation of  $TiB_2$ . The formation of oxide layers on Mg during preparation of the sample and pre-ignition heating can inhibit the yield of  $TiB_2$  due to a shift from stoichiometric conditions. The extent of oxidation is worth investigation, especially at elevated temperatures during pre-ignition heating. This was evident in DTA traces in air with Equations 9 and 10 and with Mg alone. Of particular interest were three exotherms present at  $551^\circ C$ ,  $572^\circ C$ , and  $737^\circ C$ . These exotherms are attributed to oxide layer formation on Mg which crack due to lattice mismatch (Mg (0001) HCP and MgO (111) rocksalt), exposing fresh Mg to the oxidizing atmosphere [40, 43].

### 2.2.3 Other Methods of $TiB_2$ Synthesis

Submicron  $TiB_2$  powders can be produced by the reduction of titanium tetrahalide and boron halide. The reactants are mixed with stream of hydrogen heated in a plasma heater, which reduces the halides, forming submicron (50 nm)  $TiB_2$  [14]. To produce  $TiB_2$  at lower temperatures and larger quantities, homogeneous gas phase reactions were studied using a two-step reaction involving  $TiCl_4(g)$  and  $Ti(s)$  by Brynestad *et al.*  $TiCl_4$  gas was heated to 1500K and flowed over Ti metal, forming  $TiCl_3(g)$ . The  $TiCl_3$  was then mixed with  $BCl_3(g)$  at 1500K, forming  $TiB_2(s)$ ,  $TiCl_4(aq)$  and excess  $BCl_3(aq)$  at ambient conditions. The solid  $TiB_2$  was separated from the other products by distillation, leaving pyrophoric  $TiB_2$  (0.1-1.0nm) [5]. Chen *et al.* have produced nanocrystalline  $TiB_2$  using a solvothermal reactions. Boron was reduced with metallic sodium and

magnesium, and with a one-step reaction with  $\text{TiCl}_4(l)$  and  $\text{NaBH}_3(s)$ . All required long (6-12 hrs) heating treatments at relatively high temperatures ( $400^\circ\text{C}$ - $700^\circ\text{C}$ ) [7, 8, 13, 38].

## 2.3 Leaching

Leaching refers to the removal of a soluble fraction from an insoluble fraction in the form of a solution. Leaching processes involve the selective dissolution of a compound of interest. In the fundamental example of a water wash, leaching is the displacement of one interstitial liquid by another, where the soluble species may be solid or liquid. The general mechanism of leaching may be based on physical solution or chemical reaction, and takes place in five basic steps: diffusion of reactive molecules to the surface, adsorption on the surface, reaction on the surface, desorption of reacted products, and diffusion of the desorbed products [24]. The acid leaching in the scope of this thesis focused on the chemical reaction limited effects by assuming a homogenized solution throughout the leaching process. This approximation is based on the elimination of a concentration gradient within the system due to vigorous mixing.

### 2.3.1 Leaching Candidates

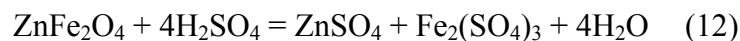
Different solutions, or leachants, can be used to selectively remove the desired species into solution. Selection is dependent on thermodynamics, kinetics, and empirical observation. To determine potential leachants, Sangwal *et al.* studied the mechanistic steps of acids, alkalis, and aqueous salts in the etching of the (100) surface of MgO. The acids used in the study were  $\text{HNO}_3$ ,  $\text{HCl}$ ,  $\text{H}_2\text{SO}_4$ , and  $\text{H}_3\text{PO}_4$ , while the alkali solutions included  $\text{NaOH}$  and  $\text{KOH}$ . Melts of neutral salts and alkali solutions were also tested [36]. The strong acids resulted in good etch pits and being thermodynamically favorable. None of the salts and alkali solutions resulted in dissolution, and this was not expected due to the reactions being thermodynamically unfavorable. None of the melts of neutral salts resulted in favorable etching. It can be suggested from this study that to obtain thermodynamically favorable etching of the reactive (100) MgO surface, strong acids are better candidates than alkali solutions or aqueous salts. Sangwal's findings agree with predicted dissolution behavior from handbook values by Samsonov [31].

Handbook literature by Samsonov *et al.* catalogs the resistance of powdered refractory compounds to molten metals, acidic, and alkali solutions. In the case of molten metals, TiB<sub>2</sub> showed resistance up to 1000°C to a variety of environments. TiB<sub>2</sub> in moderate concentrations of H<sub>2</sub>SO<sub>4</sub> (10wt%-20wt%) showed significant resistance at low leaching times (89%-96% recovery). At longer times or near the boiling point, however, significant losses were observed (5.5%-58% recovery). In HCl, a similar pattern was observed in which percent recovery was a strong function of concentration. Only at relatively low concentrations of HCl and short leaching times of 30 minutes, was recovery significant (~93.5%). All recoveries were excellent (95.5% and greater) for dilute concentrations of HNO<sub>3</sub> except leaching for 2 hours in 1.43M at the boiling point [32].

### 2.3.2 *Dissolution of MgO in Acid and Kinetic Models*

The dissolution of a surface is generally characterized in a series of steps that are either diffusion or reaction-controlled. Sangwal *et al.* proposed a nine-step model more specific to the dissolution of a surface with an acid. (1) Availability of H<sup>+</sup> ions and the associated anions to the surface of the oxide, (2) Capture and migration of H<sup>+</sup> ions and associated anions on the surface, (3) Formation of a complex, (4) Adsorption of the complex onto the surface, (5) Formation of an activated complex, (7) Dissociation of the activated complex into reaction products, (8) Desorption of the reaction products from the surface, and (9) Diffusion of reaction products into solution. Steps (1) and (9) are diffusion rate limited, while steps (2)-(8) are reaction controlled. The slowest step determines the dissolution rate, and therefore may be diffusion controlled or reaction rate controlled [34].

Kershaw reported on the development of a high-acid leaching upgrade to the zinc oxide leaching process at the Pasmaenco Metas-EZ zinc plant [18]. The upgrade was designed to increase zinc extraction from calcine based on Equation 12 using a second leaching stage.



Concentrations used varied from 0.05M-0.1M H<sub>2</sub>SO<sub>4</sub> during the high-acid leaching stages at 85°-95°C. However it was reported that concentrations around 0.05M were difficult to control because of process conditions. 84% of the zinc ferrite solids were extracted after the first leaching step and 85% after the final leaching wash. The dissolution was increased to 87% when the flowrate of spent electrolyte was increased by an unspecified amount to the final leaching stage. This electrolyte solution is a dilute sulfuric acid stream that aids in lowering the pH. pH ranges were not specified for the high-acid leaching washes.

Rashman *et al.* investigated the dissolution of MgO using ammonium chloride at constant pH. A pH-stat was used to maintain a pH of 4.5 during the leaching process that followed the reaction in Equation 13.



It was determined that the dissolution rate was sensitive to leaching temperature, from 30°C-70°C. The effects of magnesium chloride and ammonium chloride concentrations on dissolution rate were studied. No dependence on magnesium chloride concentration was observed, however, two distinct rates were present for ammonium chloride concentrations up to 1.0M and greater than 1.0M. Complete conversion was observed after 500s for concentrations greater than 1.0M and ~700s for concentrations less than 1.0M. Interestingly, measured data showed no dependence of the rate of reaction on pH (3.0-6.0) [25].

Rashman and Jones did studies on the dissolution of MgO in HCl with particular attention to the initial kinetics. Rashman studied the effects in the presence of excess acid and reported the kinetics based on a shrinking particle model. H<sup>+</sup> ions were proposed to diffuse through the liquid-solid boundary layer to the surface, react, and then diffuse back into the bulk solution. In aqueous HCl, MgO reacts to form magnesium chloride. Leaching experiments were carried out in HCl concentrations from 1.0M-5.3M at 45°C-75°C. As in the previous study with ammonia chloride, the rate of dissolution of MgO was a strong function of temperature and the rate of dissolution decreased with increasing concentration [26]. This decrease in rate indicates that the reaction is the rate

controlling step. However, this finding is in disagreement with previous work done by Jones *et al.* which found two regimes in dissolution. The initial dissolution rate increased rapidly despite a decrease in pH, and a second regime in which the rate decreases with increasing pH [16, 27].

The derivation of the pre-exponential factor and activation energy of the overall dissociation of MgO is available in the literature [34]. Equations 14-16 are the result of the derivation as applied to the MgO and strong acid system for dissolution at the surface (*s*).

$$v_s = A_s e^{\left(\frac{-E_s}{kT}\right)} \quad (14)$$

$$A_s = (3.66E5) \left( \frac{f\phi c \alpha}{Zr_f} \right) \quad (15)$$

$$E_s = \left[ \frac{1}{4}(E_1 + E_2) + \frac{1}{2}E_3 + E_4 + \frac{1}{2}\Delta H^\circ \right] \quad (16)$$

$v_s$  is the dissolution rate of MgO in  $\text{g cm}^{-2} \text{h}^{-1}$  at the surface,  $A_s$  is the pre-exponential factor, and  $E_s$  is the activation energy.  $\phi$  is defined as the function that dictates the adsorption of a pair of  $\text{H}^+$  ions onto the surface, and  $Z$  is the number of free pairs of bonds on the surface. Specific to the acid used,  $\alpha$  is the degree of dissociation, and  $c$  is the concentration. There are two terms in Equation 16 that are ratios in reference to the reactive (100) face.  $f$  is the ratio of the depth of the pit,  $r_f$  is the ratio of  $[\text{Mg}^{2+}]$  ions [34]. Experimentally, the pre-exponential factor and activation energy were determined for various concentrations using Arrhenius plots. The activation energy was determined to be 0.59 eV for  $\text{HNO}_3$  and  $\text{HCl}$  at 0.5M and 6.0M. The activation energy was found for  $\text{H}_2\text{SO}_4$  at concentrations less than 18M. Therefore from Equation 14, it can be concluded that the pre-exponential factor showed a clear dependence on concentration.

Much of the work by Sangwal *et al.* has focused on the dissolution kinetics and mechanism of MgO through the etching of selected surfaces with strong acids. Over a range of temperatures (21-84°C), their work showed that the activation energy of dissolution was constant (0.59 eV). This observation was made over a relatively wide

range of acid concentrations, 0.1N-18N H<sub>2</sub>SO<sub>4</sub>, 0.5N-6.0N HNO<sub>3</sub>, and 0.5N-6.0N HCl. The rate of dissolution had a linear dependence on the inverse temperature, suggesting activation energy was independent of concentration [35].

The effect of concentration of the strong acids on the overall dissolution rate was also studied by Sangwal *et al.* Their observations at room temperature were of particular interest, but dissolution rates at elevated temperatures for H<sub>2</sub>SO<sub>4</sub> displayed similar behavior. The maximum dissolution rate of MgO occurred in about 6.0N HNO<sub>3</sub>, 6.0N HCl, and 18.0N H<sub>2</sub>SO<sub>4</sub>. Above 18N H<sub>2</sub>SO<sub>4</sub>, Sangwal *et al.* report the dissolution rate is diffusion controlled. The rates at low concentrations were of particular interest, allowing concentrations low enough for selective leaching applications, while maintaining reasonable dissolution rates. It is observed that leaching with 0.5N-1.5N strong acids will allow for relatively fast reaction rates, while reducing the potential for attack on the desired compounds [35].

A final point must be made regarding the reaction between species in a leaching environment in the presence of inorganic salts. Inorganic salts in aqueous solutions have been known to affect the pH and thus may impact the macroscopic dissolution rate of MgO. The presence of acidic salts in an aqueous solution can decrease the pH with increasing salt concentration. During etching studies, these salts can contribute to an acidic condition. To further understand the affect acidic salts and inorganic salts have on the dissolution of MgO, Sangwal *et al.* studied the mechanism in various concentrations of aqueous salt.

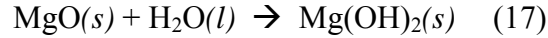
Focusing on chlorides, hydrated forms of CuCl<sub>2</sub>·2H<sub>2</sub>O and FeCl<sub>3</sub>·6H<sub>2</sub>O were used in the study. It was determined that the activation energies of the macroscopic dissolution rate were larger than the activation energies for diffusion-controlled dissolution. This agrees with their previous work that showed the dissolution of MgO was a reaction rate controlled process. This suggests that the dissolution of MgO in the presence of inorganic salts did not change the absolute values of the activation energy [33, 37].

#### 2.3.4 Hydration of MgO

There is considerable debate as to the spontaneity and completeness of the dissolution of MgO on the stable (100) surface in water. Some have reported the MgO

(100) surface dissociates water at adsorbing sites consisting of five-coordinated ions. This thermodynamically favored process ( $\Delta G^\circ = -27.58$  kJ/mol) results in a hydroxylated surface. However, others have reported calculations that predict defect-free MgO (100) surfaces to not dissociate water. This implies dissociation occurs on defects [3, 15, 41]. For the purposes of this study, the relative amounts of MgO and Mg(OH)<sub>2</sub> present during leaching are of importance rather than the exact amounts of conversion. Thus, the hydration of MgO will be presented from the scope of the general mechanism and the amount of conversion.

Magnesium hydroxide, Mg(OH)<sub>2</sub>, is produced from the hydration of MgO, according to the following reaction:



According to Rocha *et al.*, the reaction mechanism involves the dissolution of MgO followed by Mg(OH)<sub>2</sub> precipitation. The authors proposes a mechanism in which water molecules are assumed to chemisorb onto the oxide surface, creating a surface layer of Mg(OH)<sub>2</sub>. This in turn inhibits the hydration of MgO. This has been modeled based on the mass balance of Mg(OH)<sub>2</sub> produced during the hydration of MgO.

$$C_{\text{Mg}(\text{OH})_2}(t) = C_{\text{MgO}}^\circ - C_{\text{MgO}}^\circ \exp\left[\frac{b}{a}(1 - \exp(at))\right] \quad (18)$$

Assuming the initial concentration of Mg(OH)<sub>2</sub> is zero,  $a$  is the rate constant ( $\text{h}^{-1}$ ) related to the change in porosity with time at a temperature,  $T$ , and  $b$  relates the physical and kinetic properties as defined in Equation 19.

$$\varepsilon(t) = \frac{\varepsilon^\circ}{\varepsilon^\circ + (1 - \varepsilon^\circ)\exp(-at)} \quad (19)$$

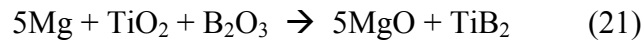
$$b = \frac{\varepsilon^\circ a}{1 - \varepsilon^\circ} k_0 \exp\left(-\frac{E}{RT}\right) \quad (20)$$

The experimental results of the hydration of MgO showed an exponential increase in Mg(OH)<sub>2</sub> conversion above 35°C. Linear behavior took over at around two hours at 90°C and three hours at 70°C. At 35°C, the trend was nearly linear throughout the entire test period. The data points were compared to work by Birchal *et al.* From the model, the physical and kinetic parameters, *a* and *b* in Equations 18-20 were determined and an activation energy of 62.3 kJ/mol calculated [4, 10, 11, 29].

The dissolution of Mg(OH)<sub>2</sub> in acidic water has been performed by Jordan *et al.* in an effort to determine the dissolution behavior of single crystals of Mg(OH)<sub>2</sub>. Quantitative kinetic data and dissolution mechanisms were determined based on observations made at monolayer level resolution. Dissolution rates were measured up to 35°C and kinetic parameters calculated using the classical Arrhenius equation. Based on activation energies and dissolution rates, it was determined the dissolution of Mg(OH)<sub>2</sub> in acidic water was surface reaction controlled rather than diffusion controlled [11, 17].

#### 2.4 Purification of Borides

Others have used mechanical milling to produce TiB<sub>2</sub> from the oxidation-reduction reaction:



The resulting MgO/TiB<sub>2</sub> was leached in relatively low HCl concentrations. Welham *et al.* successfully leached 20mg 50µm MgO/TiB<sub>2</sub> powders in 1.0M HCl solution for 2 hrs, and the solids were removed by centrifugation. The solids were washed with deionized water and dried at 110°C for 24 hrs. Only elemental analysis was performed on the solids [45]. Ricceri *et al.* synthesized 0.05-0.1µm TiB<sub>2</sub> according to Equation 21. The milled products were leached for 2 hrs in 0.5M HCl and solids analyzed. Fe and MgO were successfully leached into solution based on XRD analysis [28].

In a related study of the formation of TiN and TiC using mechanical milling, Welham *et al.* leached 20mg <50µm MgO/Fe/TiC powders and MgO/TiN powders for 18 hrs and used 3% HCl. According to XRD analysis, Fe and MgO were successfully leached, leaving behind the hard TiC and TiN [47].

Pressureless densification has been used by researchers [48] with  $\text{ZrB}_2$  powders. WC and  $\text{B}_4\text{C}$  additives were evaluated to remove  $\text{B}_2\text{O}_3$  and  $\text{ZrO}_2$  and increase  $\text{ZrB}_2$  purity. During sintering, the  $\text{B}_2\text{O}_3$  vapor pressure was low enough to facilitate a phase change into the gaseous phase. The Gibbs free energy for WC and  $\text{B}_4\text{C}$  indicated that the reaction with  $\text{ZrO}_2$  would be favorable at  $1850^\circ\text{C}$  and  $1200^\circ\text{C}$ , respectively. From x-ray diffraction analysis, WC did not remove all  $\text{ZrO}_2$  even after heating in excess of  $2000^\circ\text{C}$ .  $\text{B}_4\text{C}$  effectively removed all  $\text{ZrO}_2$  at  $1450^\circ\text{C}$  [48].

## **3 CHAPTER THREE – EXPERIMENTAL PROCEDURE**

### **3.1 Introduction**

This chapter presents the synthesis, processing, testing, characterization, and equipment used in the acid leaching of commercial and SHS produced powders. Synthesis covers the magnesium SHS thermite reaction in detail. Processing describes the post-reaction milling technique used prior to acid leaching. Testing covers the candidate selection and defines minimum pH leaching. The Experimental Design is included here which details the experimental matrix and the acid leaching procedure. Leaching was conducted at 30°C, 60°C, and 90°C at pH levels of 1.0, 2.5, and 4.0 for the commercial stoichiometric mixture of powders. Similarly, leaching was performed at 90°C at the same pH levels for the SHS produced MgO/TiB<sub>2</sub>. This method of leaching was chosen to investigate the effects of leaching at a minimum pH on particle morphology, as well as the extent of MgO/TiB<sub>2</sub> conversion. A set of exploratory experiments were performed to analyze the effect of a second leaching cycle. This third matrix was performed at the same temperature and pH targets as the SHS products. The equipment section covers the hardware and facilities used in this study. Particle size and morphology are of stock powders are discussed as well.

### **3.2 Particle Size and Morphology of Stock Powders**

In this section, particle morphology and particle size are presented in brief. The complete results including SEM micrographs and particle size analysis can be found in the Appendix. SEM was done on a Leo 1550 equipped with a Gemini column. EDS was performed on a Jeol JSM-6400 SEM/EDAX running SemAfore 3.0 Pro. For stock powders, a Jeol JSM-3500 was used for particle size and morphology. Particle size analysis was done on a HORIBA Laser Scattering Particle Size Distribution Analyzer LA-950 for the Mg SHS reagents.

The stoichiometric mixture of commercial powders described to in this study refer to a mixture of commercial TiB<sub>2</sub> and MgO. Commercial carbothermic TiB<sub>2</sub> was

purchased from H.C. Starck (Lot No. 50842-BS). The purity was listed as 98.11% with an average particle size of 2.417 $\mu\text{m}$  according to the certificate of analysis. The crystal structure is hexagonal closed-packed with a  $c/a$  ratio of 1.066 at room temperature [23]. MgO was purchased from Alfa Aesar (Lot No. F09P29). The purity was listed as 99.9996% according to the certificate of analysis, with an average particle size of 44 $\mu\text{m}$  from the product data sheet

The stock powders used in the magnesium SHS thermite reaction were purchased in bulk quantities. Pigment grade TiO<sub>2</sub> was purchased from Fisher Scientific (Lot No. 040167). The purity was listed as 99.673% according to the certificate of analysis. The mean particle size was 1.004  $\mu\text{m}$  from the particle size analysis. Amorphous B<sub>2</sub>O<sub>3</sub> was purchased from Fisher Scientific (Lot No. 015532). The purity was listed as 98.5000% according to the certificate of analysis. The mean particle size was determined to be 189.5115 $\mu\text{m}$ . Finally, magnesium flakes were purchased from Reade Manufacturing Company (CAS No. 7439-95-4). The purity was listed as 98.80% minimum and a mean particle size of 45 $\mu\text{m}$  according to the certificate of analysis.

### 3.3 Synthesis

Stoichiometric amounts of the reactant powders were mixed according to Equation 22.



Three 130.0g batches (96.665g MgO and 33.335g TiB<sub>2</sub> theoretical yield) were used to produce all powders used in this study. 38.3129g TiO<sub>2</sub> and 33.3982g B<sub>2</sub>O<sub>3</sub> were weighed and mixed in an alumina mortar and pestle. A light shearing motion was used to homogenize the powders. Once homogenized, 58.2965g Mg was weighed and added to the mortar. Again, a light shearing, motion was used to homogenize the mixture. A glass stir rod was used to facilitate mixing, as the TiO<sub>2</sub>/B<sub>2</sub>O<sub>3</sub> mixture tended to clump at the bottom of the mortar. Mixing was continued until a light-gray mixture was achieved. The powders were transferred to a fused silica crucible, cast from silica slip in a plaster of Paris mold. The crucible holding the reactant mixture was set inside the refractory-lined

reaction chamber. A second crucible was placed on top of the crucible with a Kaowool™ gasket separating the pieces. A 1 kg weight was placed on top of the cover to keep the powders within the closed system.

To initiate the reaction, a 20.3cm piece of 18 gauge (1.023mm OD) NiCr wire was connected to a variable transformer (120V), and placed in the crucible, just touching the top of the reactant powders. Just prior to ignition, the reaction chamber door was closed and sealed from the environment. A forced-air ventilation system with a two-stage particle filter was used to handle vapors evolved from the reaction. The variable transformer was used to increase the voltage at a rate of about 2%/5s. Each reaction initiated at 7%-8% of maximum. Pictures of the reaction setup are included in the equipment used section of this chapter.

### **3.4 Processing**

The cemented agglomerates were ball milled to break apart agglomerates for acid leaching. Particle size effects of acid leaching are not part of the scope of this work, and are a fixed parameter. The guidelines for ball milling recommend filling the void spaces with powders until the grinding media is barely covered by the charge volume [2]. Optimal milling speed for the single-tier roller mill from U.S. Stoneware was determined to be 65% of maximum. A single 38.9g Mg SHS produced batch of as-reacted product was placed in a 4.92L Type 304 stainless steel milling jar from U.S. Stoneware. The powders were milled with 1.27cm OD Type 302/304 stainless steel balls from Glenn Mills Inc. Milling was performed for 30 hours and samples taken at predetermined time intervals (2h, 4h, 6h, 8h, 12h, 18h, 24h, and 30h).

The powder to media ratio of the 38.9g sample was scaled up to approximate the mass of grinding media required to mill 366.14g of powders produced from the three 130g Mg SHS reactions. About 2822g of grinding media was removed so that the charge just covered the grinding media. The powders were milled for 20 hours with 553 balls. 345.6g of powders were recovered. The powders were dried in an oven at 110°C for 12 hours.

### 3.5 Testing

This section describes in detail the experimental procedure used for acid leaching and candidate selection. A minimum pH target is selected to quantify the amount of MgO and TiB<sub>2</sub> leached into solution. This minimum pH method is explained in detail covering the experimental design and characterization techniques.

#### 3.5.1 Candidate Selection

Leaching agents were chosen for this study were selected based on experimental and commercial factors. From Sangwal *et al.*, alkaline solutions, and salts were shown to have unfavorable thermodynamics ( $\Delta G > 0$ ) [36]. A summary of the referenced work is discussed in Chapter 2. Samsanov's handbook on oxides confirms the dissolution behavior of MgO in acids referenced above. Strong and weak acids were candidates considered for this work [31].

The strong acids considered include HCl, H<sub>2</sub>SO<sub>4</sub>, and HNO<sub>3</sub>. All have been used to leach MgO from TiB<sub>2</sub> by others and all are thermodynamically favorable [28, 45, 47]. HCl and H<sub>2</sub>SO<sub>4</sub> react with MgO to form MgCl<sub>2</sub> and MgSO<sub>4</sub>, respectively. Sources of chlorides and sulfides pose a significant environmental concern, especially when dealing with commercial scale volumes.

Leachant candidate selection also considered interactions with TiB<sub>2</sub>. Samsanov's handbook on refractory compounds lists the insoluble percentage of TiB<sub>2</sub> with different reagents. HNO<sub>3</sub> showed to have the highest retention of TiB<sub>2</sub> at all temperatures and concentrations. Work by Welham *et al.* used 1.0M HCl to leach MgO from the MgO/TiB<sub>2</sub> synthesized from ball milling. They report dissolution of significant amounts of TiB<sub>2</sub> and that leaching of a different reagent would result in higher levels of TiB<sub>2</sub> recovery [44]. Experimental observation of using HCl created a pyrophoric TiB<sub>2</sub>, causing spontaneous ignition of the powders produced in this particular system. Sulfide impurities have been observed after H<sub>2</sub>SO<sub>4</sub> leaching which can adversely affect the structural integrity of the TiB<sub>2</sub> [20]. HNO<sub>3</sub> reacts with MgO to produce a more benign Mg(NO<sub>3</sub>)<sub>2</sub>. HNO<sub>3</sub> is also commonly used as the solvent in ICP-MS, making ionic characterization more feasible.

Weak acids were considered as leaching agents. Some were eliminated from consideration due to the exposure risk such as HCN and HF. Others such as  $\text{H}_2\text{CO}_3$  and  $\text{CH}_3\text{COOH}$  may introduce impurities to the  $\text{TiB}_2$ . The pKa of others such as  $\text{H}_3\text{BO}_3$  were so high (pKa = 9.27) that the achievable pH would not be low enough to leach MgO. Of the weak acids,  $\text{H}_3\text{PO}_4$  seemed most promising. Work by Sangwal *et al.*, showed poor single crystal MgO dissolution with  $\text{H}_3\text{PO}_4$ , but may serve well as a polishing agent [36].

### 3.5.2 Leaching by Minimum pH

This method of acid leaching involves the removal of MgO in a solution at a fixed temperature using aliquots of  $\text{HNO}_3$ . In this “open system”, stoichiometric amounts of powders are first added to deionized water at 30°C, 60°C, and 90°C. Aliquots of  $\text{HNO}_3$  are then added to the system, resulting in a minimum achievable pH. Samples were taken at predetermined acid volumes and ionic presence determined from ICP-MS. The schematic below illustrates the leaching behavior at a pH of 1.0.

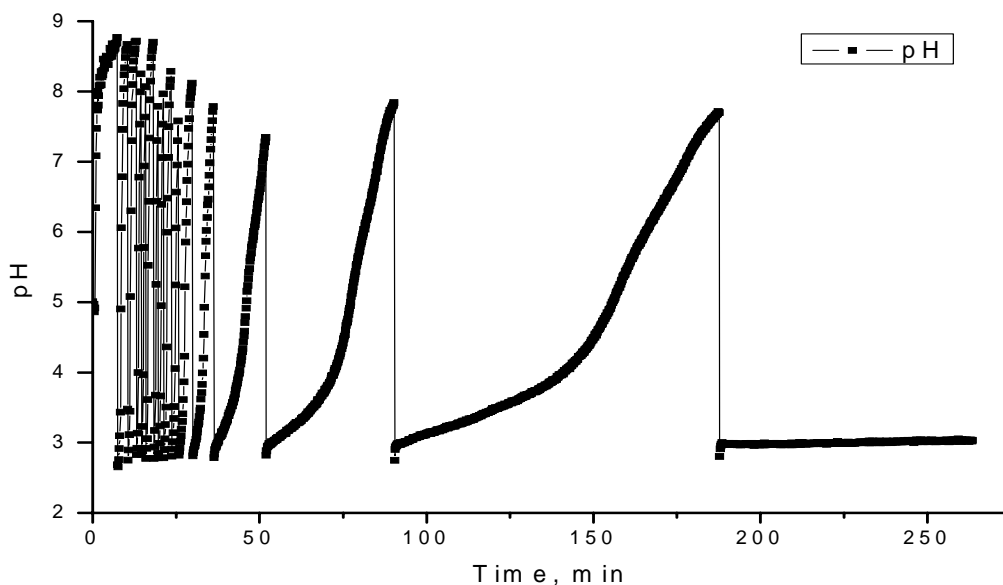


Figure 1: Oscillatory pH in response to addition of acid is characteristic of a buffer solution [9]

The saw-tooth behavior shown above is characteristic of a buffer solution, resisting change in pH as  $\text{HNO}_3$  is added to the system [9]. As acid is introduced, the pH drops, but this is countered as  $\text{MgO}$  reacts with the acid. The  $\text{H}^+$  concentration decreases and consequently, pH increases. This cycle continues until the concentration of  $\text{MgO}$  has dropped to a point where further addition of acid leaches  $\text{TiB}_2$ .

The benefits of this method of leaching include a minimal amount of  $\text{TiB}_2$  leached and the commercial scale-up feasibility. The addition of acid by small aliquot volumes defines a minimum pH target, where acid is not in excess until the point at which  $\text{TiB}_2$  is leached. Thus, the leaching of  $\text{TiB}_2$  into solution is minimized. This method is also attractive on the commercial scale since the concentration of acid being added to the system is irrelevant, as the concentration of  $\text{H}^+$  ions supplied to the system is controlled.

Accurate pH control is a challenge with this leaching approach which can impact the repeatability in a non-steady state open system. This was also experienced by Kershaw on a large scale where localized concentration becomes significant in large reactors [18]. Controlling the addition of acid impacts the number of moles present in the leaching solution. In addition, kinetic data of either reactant with  $\text{HNO}_3$  is unavailable with this approach since time which is dependant on the flow rate of acid does not remain constant. A schematic of the leaching process is shown in Figure 2.

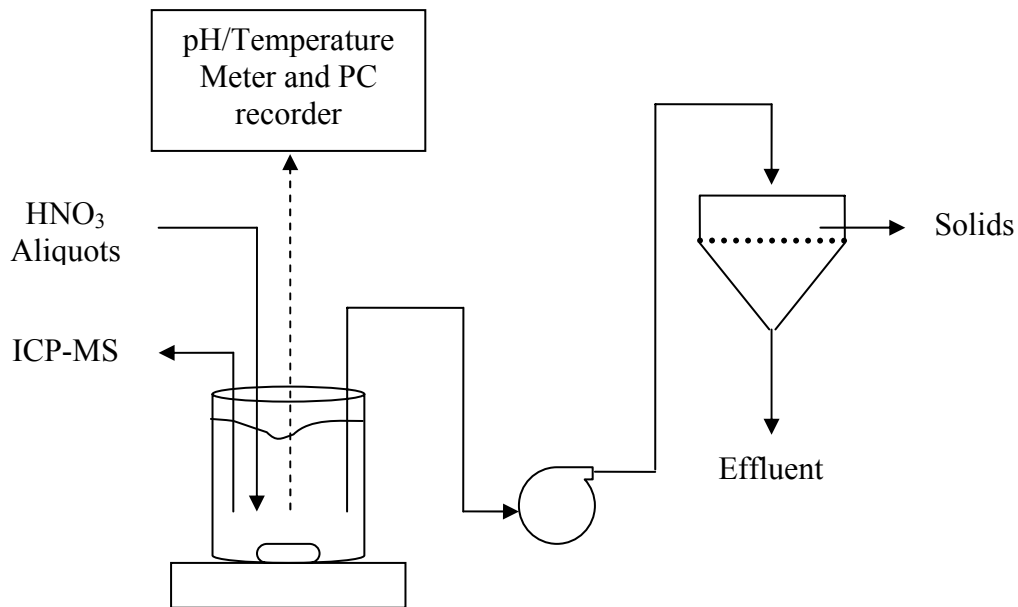


Figure 2: Leaching process including solids separation

### 3.5.2.1 Experimental Design

The matrices below summarize the range of experiments completed for the minimum pH leaching method. Prior work by Logan *et al.* on the commercial scale involved leaching at 90-95°C for favorable kinetics [20]. Three pH levels were chosen, for leaching the commercial MgO/TiB<sub>2</sub> and the SHS as-milled product, mildly acidic (pH 4.0), acidic (pH 2.5), and very acidic (pH 1.0). 8-10 liquid samples were taken at predetermined aliquot volumes, and the solids were collected for analysis for each experiment. A third matrix of experiments was added to explore the leaching behavior or a second leaching cycle.

<b>Stoichiometric Mixture of Commercial Powders</b>			
	<b>pH 4.0</b>	<b>pH 2.5</b>	<b>pH 1.0</b>
<b>90°C</b>	<b>x</b>	<b>x</b>	<b>x</b>
<b>60°C</b>	<b>x</b>	<b>x</b>	<b>x</b>
<b>30°C</b>	<b>x</b>	<b>x</b>	<b>x</b>

<b>SHS Produced MgO/TiB<sub>2</sub></b>			
	<b>pH 4.0</b>	<b>pH 2.5</b>	<b>pH 1.0</b>
<b>90°C</b>	<b>x</b>	<b>x</b>	<b>x</b>

<b>Second Cycle Leaching of SHS Produced MgO/TiB<sub>2</sub></b>			
	<b>pH 4.0</b>	<b>pH 2.5</b>	<b>pH 1.0</b>
<b>90°C</b>	<b>x</b>	<b>x</b>	<b>x</b>

Table 1: Experimental matrices for minimum pH leaching

All glassware and tools were cleaned in a 10% HNO<sub>3</sub> solution bath and washed twice with deionized water. The appropriate volume of deionized water was heated to the specified temperature on a magnetic stir/hot plate. An Accumet™ AB15+ pH meter running the Fisher Scientific CyberComm Pro 2.3.1 data acquisition software was

standardized and connected to a computer. The respective amounts of powders were weighed and added to the heated water.

An initial baseline was established immediately after the powders were added to the well-mixed system. 2.0ml was removed from the solution and filtered through a syringe filter (0.45 $\mu$ m for the commercial powders, and 0.1 $\mu$ m for the SHS powders). This established a baseline concentration to compare subsequent samples to determine the extent of conversion. Aliquots of HNO<sub>3</sub> were introduced to the system using clean finnpipettes. The concentration of the acid introduced was dependent on the system volume and minimum pH level. As the system returned to neutral, the next aliquot of acid was introduced.

At predetermined aliquot intervals, a 2.0ml sample was filtered through a syringe filter. A Whatman™ nylon 0.45 $\mu$ m filter was used for the commercial powders. For SHS powders at elevated temperatures, the 2.0ml sample was briefly cooled to 45°C prior to filtering. This was due to temperature limitations on the filter membrane (Whatman Anotop™ 0.1 $\mu$ m filter). The aliquots of acid were added until either the theoretical number of moles of acid had been added to the system, or the relative change in pH with respect to time (D(pH)/Dt) was constant over an extended amount of time. The latter constraint was evident in the dilute acid (pH 4.0 and 2.5) experiments. This phenomenon is discussed in further detail in the results and discussion in Chapter 4 and by Rocha *et al.* [29].

At the conclusion of each acid leaching run, the solids were reclaimed for SEM and XRD analysis. This was accomplished by centrifuge and by vacuum-assisted filtration. Samples 18-23 were centrifuged in a 6 x 250ml polycarbonate cells at 6000 rpm for 15 minutes. The supernatant was discarded and solids washed with deionized water and combined into one cell. The suspension was centrifuged again at 6000 rpm for 15 minutes. The supernatant was tested with litmus paper before being discarded. The washing and centrifuge process was repeated until the supernatant tested neutral. The polycarbonate centrifuge cell was placed in an oven at 110°C for at least 12 hours. The powders were carefully scraped off the sides with a PTFE spatula and weighed for solids analysis.

Vacuum-assisted filtration was used for the remainder of the samples. A 2.5 $\mu$ m filter (Whatman™ Grade 5) was used for all leaching experiments. The suspension was pumped to the vacuum-assisted filtration apparatus by a variable speed peristaltic pump. At the conclusion of the filtration, the filter paper was placed in an oven at 110°C for at least 12 hours. The powders were carefully scraped off the paper and weighed for solids analysis.

Additional experiments were run to observe the effect of a second leaching cycle. The dried solids from the initial leaching cycle were placed in the same conditions as the first cycle. The leaching was performed within the same extent as the first wash. Liquid samples were again taken for mass spectrometry, and solids filtered for microscopy and powder diffraction.

### **3.6 Characterization**

Three analytical tools were used to characterize the behavior during the leaching experiment and the effects to the leached powders. Inductively coupled plasma – mass spectrometry (ICP-MS) was used for chemical analysis of the liquid samples taken during the leaching process. Scanning electron microscopy (SEM) and Energy Dispersive Spectroscopy (EDS) were used to observe the particle size and morphology of the initial and leached powders. Powder x-ray diffraction (XRD) was used to determine the compounds present in the as-reacted SHS sample as well as after leaching.

#### *3.6.1 ICP-MS*

For liquids analysis, an X-Series Thermo Electron ICP-MS was used to determine the ion concentrations of <sup>25</sup>Mg, <sup>47</sup>Ti, and <sup>48</sup>Ti ions. Each sample was diluted to a maximum of 100ppm of the highest concentration ion. A total of 298 samples were diluted, including two deionized water “blanks” to subtract background interferences.

#### *3.6.2 SEM/EDS*

To analyze the final products, a Jeol JSM-6400 with EDAX EDS and a LEO 1550 Field Emission SEM equipped with a Gemini column was used to observe the particle

size and morphology of the solids. All samples were thickness-controlled sputter coated to 15 nm with gold-palladium.

### 3.6.3 XRD

Powder x-ray diffraction was performed on a Siemens D5000 Diffractometer running Diffrac<sup>Plus</sup> EVA software (v 7.0.0.1) for spectrum evaluation. Dried powders were mounted on the stage using methanol to avoid preferred orientation. A standard Cu-K $\alpha$  diffraction pattern was produced scanning from 18°-104° (2 theta), with a step size of 0.01° at 2 s per step.

## 3.7 Materials and Equipment Used

### 3.7.1 Synthesis

The Mg SHS thermite reaction was initiated in a sealed reaction chamber measuring 1.22m x 1.22m x 1.22m. Plexiglass walls bolted onto a welded frame allowed for viewing the reaction. High-temperature refractory brick served as a stage to initiate the reactions, while Kaoboard<sup>TM</sup> and Kaowool<sup>TM</sup> lined the interior of the chamber. A two-stage particulate filter moved 0.0368 m<sup>3</sup>/min of air to filter particle dust evolved from the reaction. The chamber was sealed with high temperature sealant to ensure dust particles did not leave the chamber. To initiate the reaction, the variable transformer is used to control the current to the NiCr wire just touching the reactant powders in the crucible.



Figure 3: Reaction chamber lined with refractory brick and walls

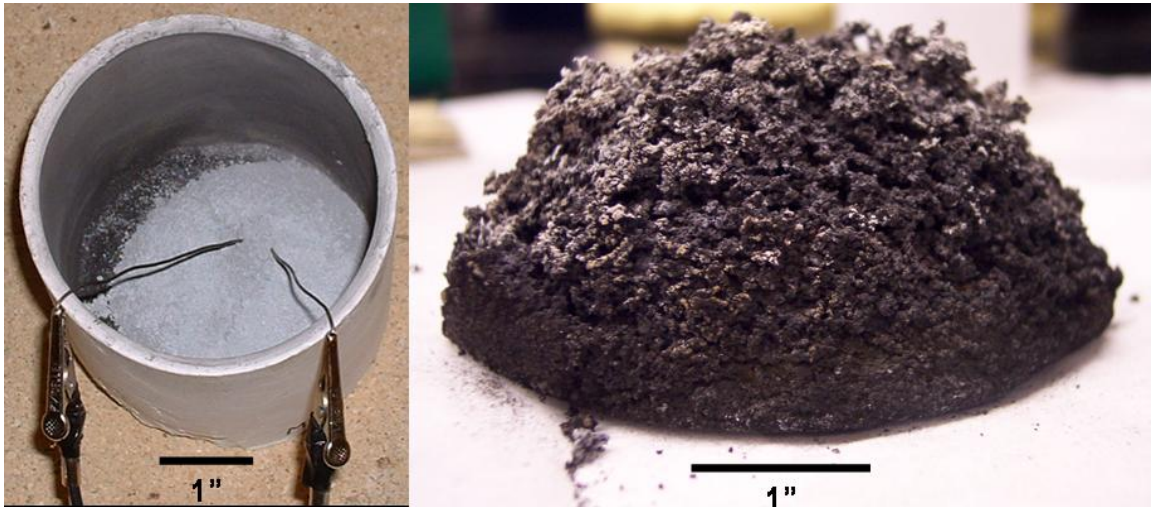


Figure 4: (left) NiCr wire just touching powders (right) product removed from crucible

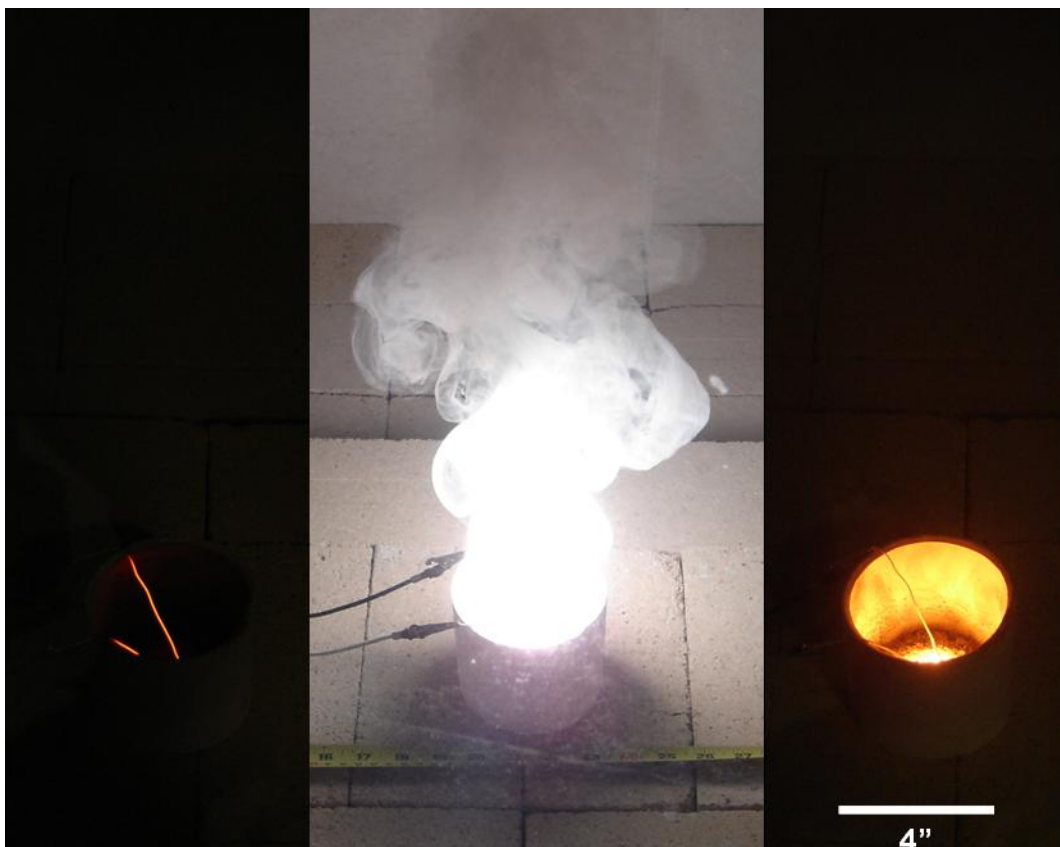


Figure 5: Stages of 38.9g Mg SHS thermite reaction. (*left*) NiCr glowing red,  $\sim 4.8\text{V}$  (*center*) SHS reaction initiated,  $\sim 7.2\text{V}-9.6\text{V}$  (*right*) Reaction completed.

### 3.7.2 Processing

Ball milling was used to break apart the agglomerates formed from the SHS reaction. A single-tier roller mill from U.S. Stoneware was used to mill the as-reacted powders. A 4.92L Type 304 stainless steel milling jar from U.S. Stoneware with 1.27cm Type 302/304 stainless steel balls from Glenn Mills Inc. was used as the milling media. From manufacturer specifications, 65% of maximum was the optimal speed for the system.

### 3.7.3 Testing

Equipment used in acid leaching consisted of an Accumet<sup>TM</sup> AB15+ pH meter using the Fisher Scientific CyberComm Pro 2.3.1 data acquisition software, vacuum-assisted filtration, and general bench-top chemistry labware. The figure below shows the typical leaching and filtration setup.



Figure 6: (*left*) Acid leaching setup (*right*) Vacuum-assisted filtration

## 4 CHAPTER FOUR – RESULTS AND DISCUSSION

### 4.1 Extent of Ball Milling

Figure 7 shows the as-reacted products dried at 110°C. In the bulk as-reacted form, the MgO acts as a cement, binding the hexagonal TiB<sub>2</sub> platelets together [19]. The optimal milling time was 18-20 hours shown in Figure 8. Further milling showed no difference in MgO/TiB<sub>2</sub> particle size. Detailed micrographs are included in the Appendix.

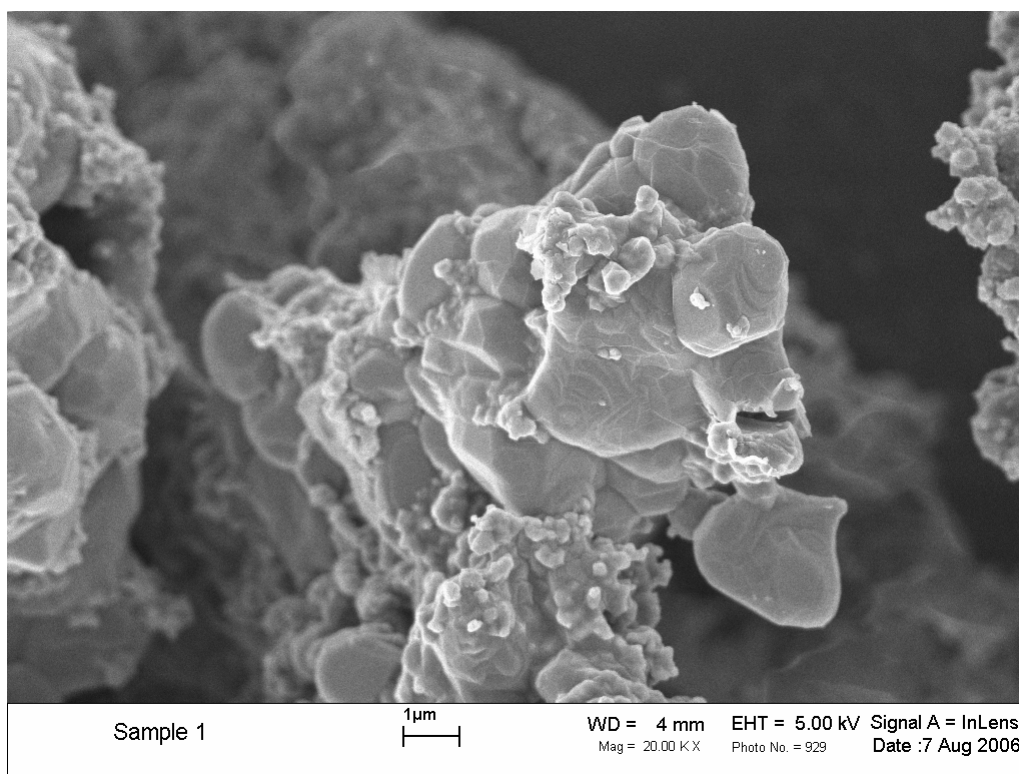


Figure 7: SEM Micrograph of dried MgO/TiB<sub>2</sub> as-reacted powders

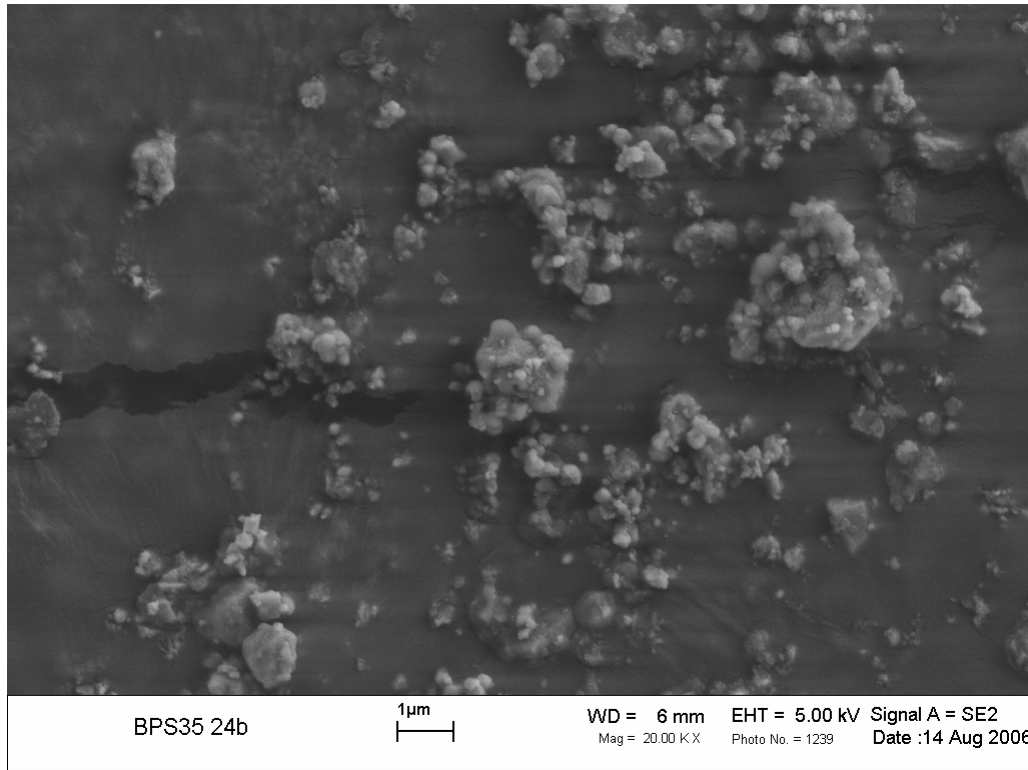


Figure 8: After 18 hours of milling, MgO/TiB<sub>2</sub> agglomerates have been reduced

## 4.1 Commercial Stoichiometric Mixture

### 4.1.1 Percent Conversion and Dissolution of Products

Titanium ions did not appear in solution in significant amounts at all temperatures and pH levels. This is due to the relatively low concentrations of acid (0.0001M-0.01M) in the leaching solution compared to methods used by others (1.0M-6.0M). The effect was similar at all temperature levels. The presence of Mg ions was measured during the leaching process and compared to the theoretical conversion of MgO to Mg(NO<sub>3</sub>)<sub>2</sub> in HNO<sub>3</sub>. The theoretical conversion of the experimental approach was tested by pilot leaching experiments of commercial MgO in the high (4.0) and low (1.0) pH levels.

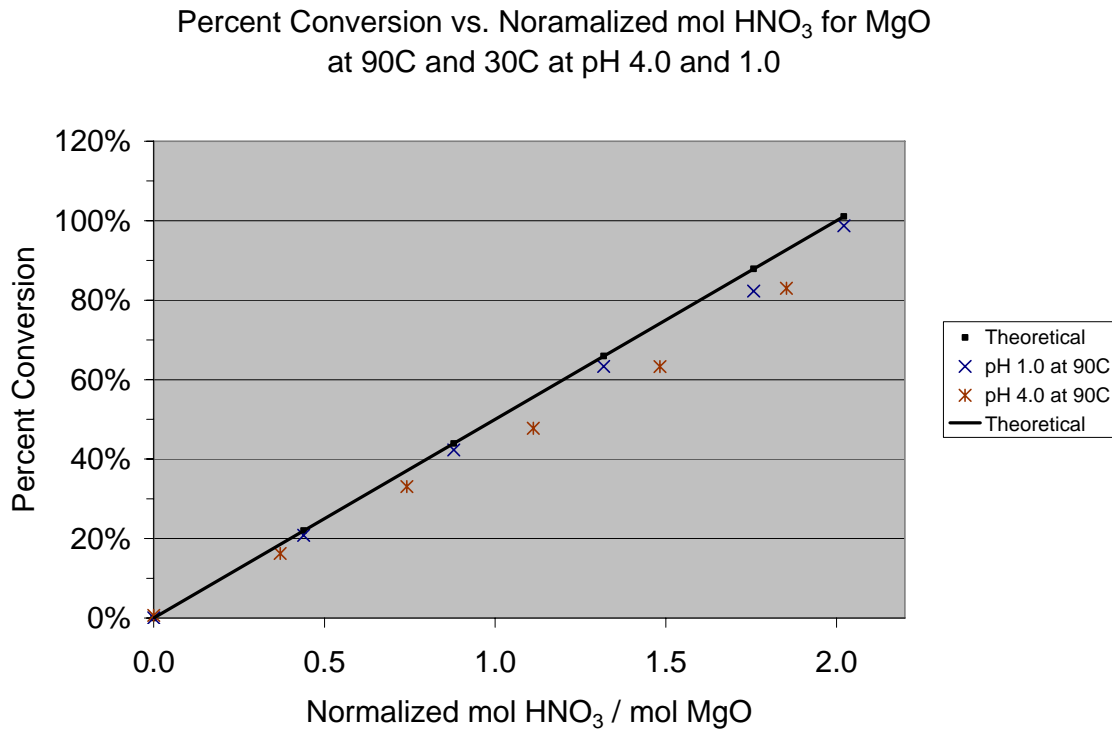


Figure 9: Stoichiometric MgO Conversion in HNO<sub>3</sub> in low and high pH conditions

From the pilot tests it was evident the experimental approach would allow complete conversion of MgO. However at the minimum pH 4.0 condition, approximately 12-15 hours to complete, adding aliquots of acid until the theoretical amount of acid was added.

At all temperatures and minimum pH levels, the MgO conversion percentage agreed with the theoretical results. Figure 10 shows the commercial mixture of powders at all temperature ranges and pH levels. It can be observed that the absence of Ti ions in the solution indicates TiB<sub>2</sub> is not being driven into solution. This was evident even at long leach times (12-15 hours) to achieve the maximum MgO conversion. It can be interpreted from this behavior that TiB<sub>2</sub> would not be attacked at the highest temperatures tested. How this impacted the particle morphology of the SHS produced MgO/TiB<sub>2</sub> aggregates was yet to be tested.

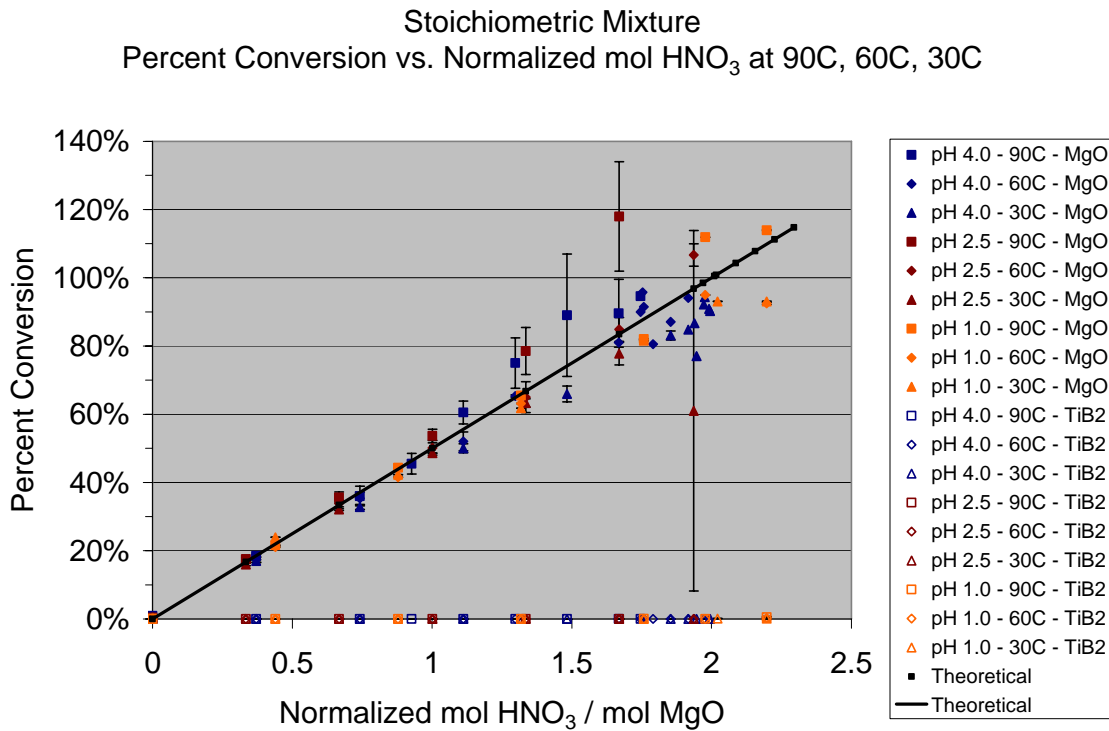


Figure 10: Conversion percentage of stoichiometric mixture of commercial MgO and TiB<sub>2</sub> based on ICP-MS data during leaching

#### 4.1.2 SEM

SEM micrographs were taken of the particles after leaching at 90°C for all pH levels. At 50,000x magnification, the particles do not differ significantly with respect to particle size and morphology. Full micrographs taken at the stub level and surface features can be found the Appendix.

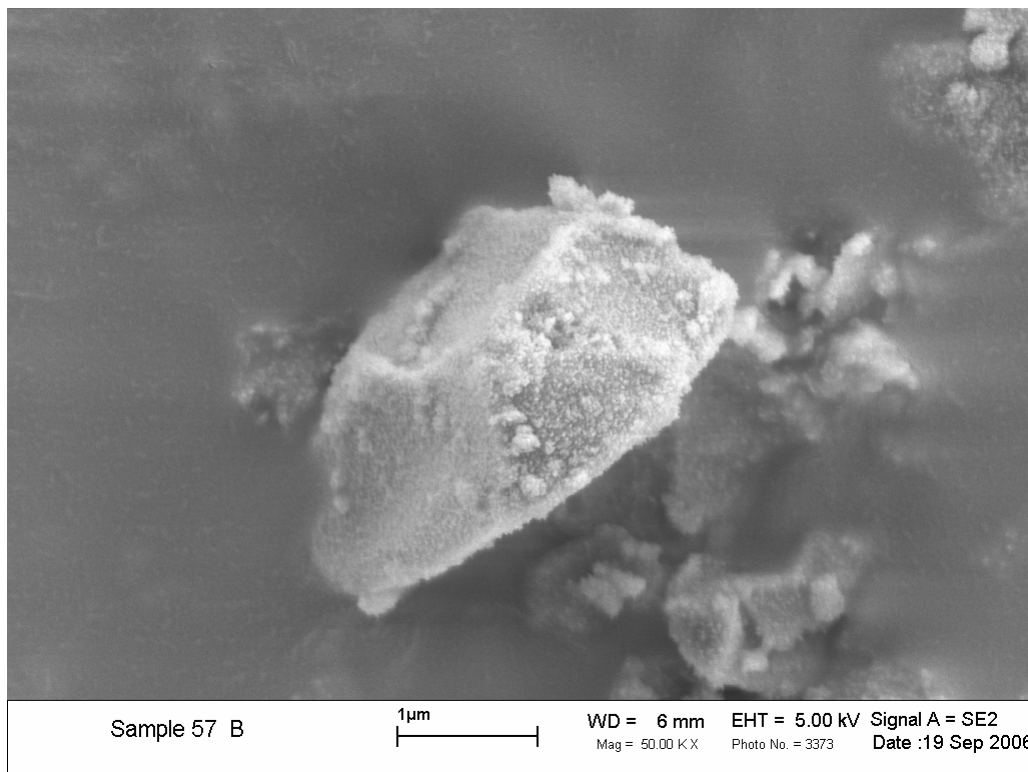


Figure 11: Commercial  $\text{TiB}_2$  leached at minimum pH of 4.0 at  $90^\circ\text{C}$

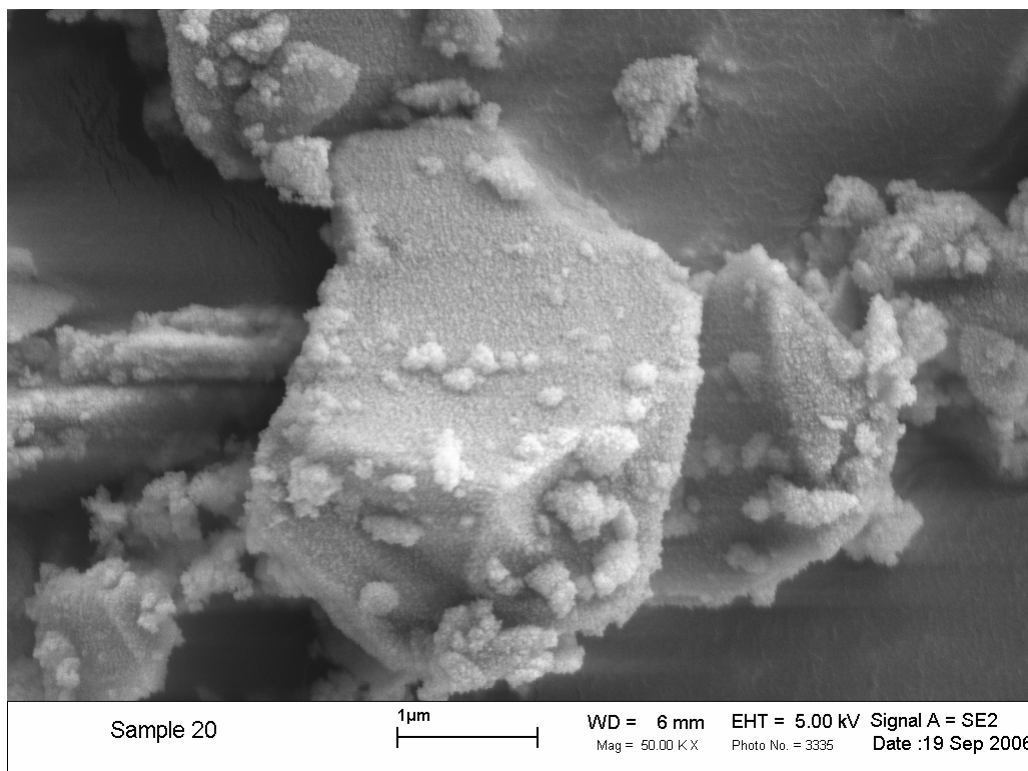


Figure 12: Commercial  $\text{TiB}_2$  leached at minimum pH of 2.5 at  $90^\circ\text{C}$

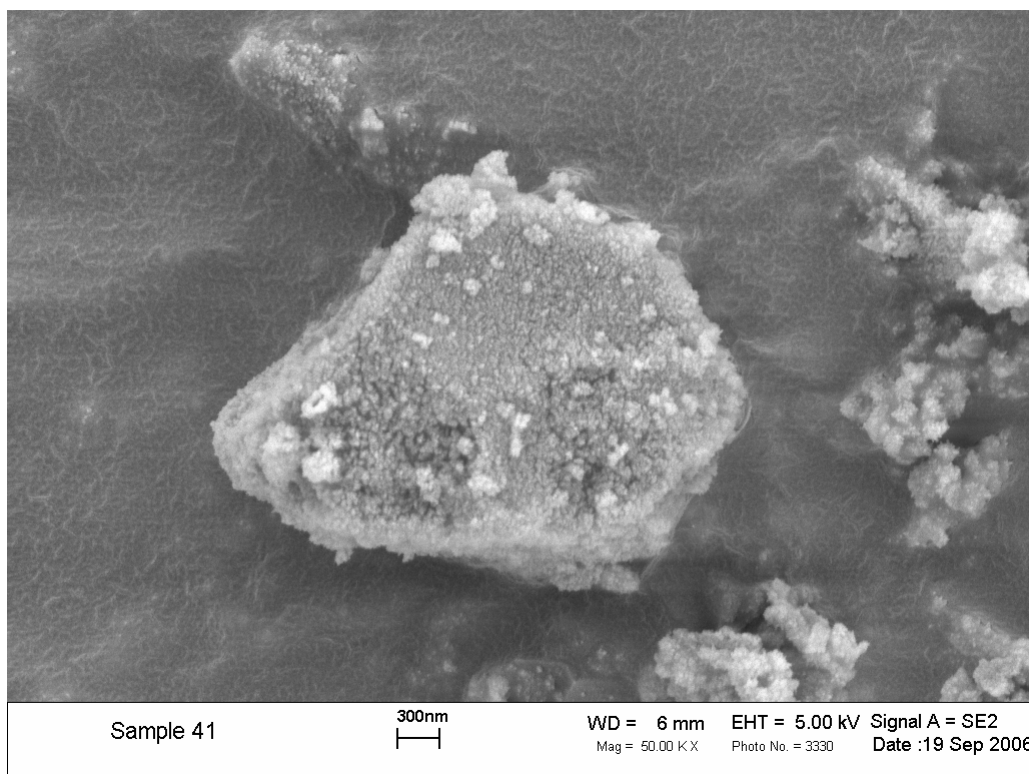


Figure 13: Commercial  $\text{TiB}_2$  leached at minimum pH of 1.0 at  $90^\circ\text{C}$

## 4.2 SHS Produced $\text{MgO}/\text{TiB}_2$

### 4.2.1 Percent Conversion and Dissolution of Products

Similar to the stoichiometric mixture of commercial powders, titanium ions did not appear in solution in significant amounts at all pH levels due to the relatively low concentrations of acid. The absence of titanium ions in the solution from the commercial powders allowed for leaching of the SHS product at  $90^\circ\text{C}$  at each minimum pH level.

The presence of Mg ions was measured during the leaching process and compared to the theoretical conversion. At all minimum pH levels, the MgO conversion percentage agreed with the theoretical results shown in Figure 14. The absence of Ti ions in the solution indicates  $\text{TiB}_2$  is not being driven into solution. This was evident even at long leach times for the minimum pH 4.0 experiments. Figure 15 shows the dissolution of  $\text{TiB}_2$  of both SHS produced and commercial powders. In each case, only trace amounts of  $\text{TiB}_2$  were detected by ICP-MS, below 100ppm.

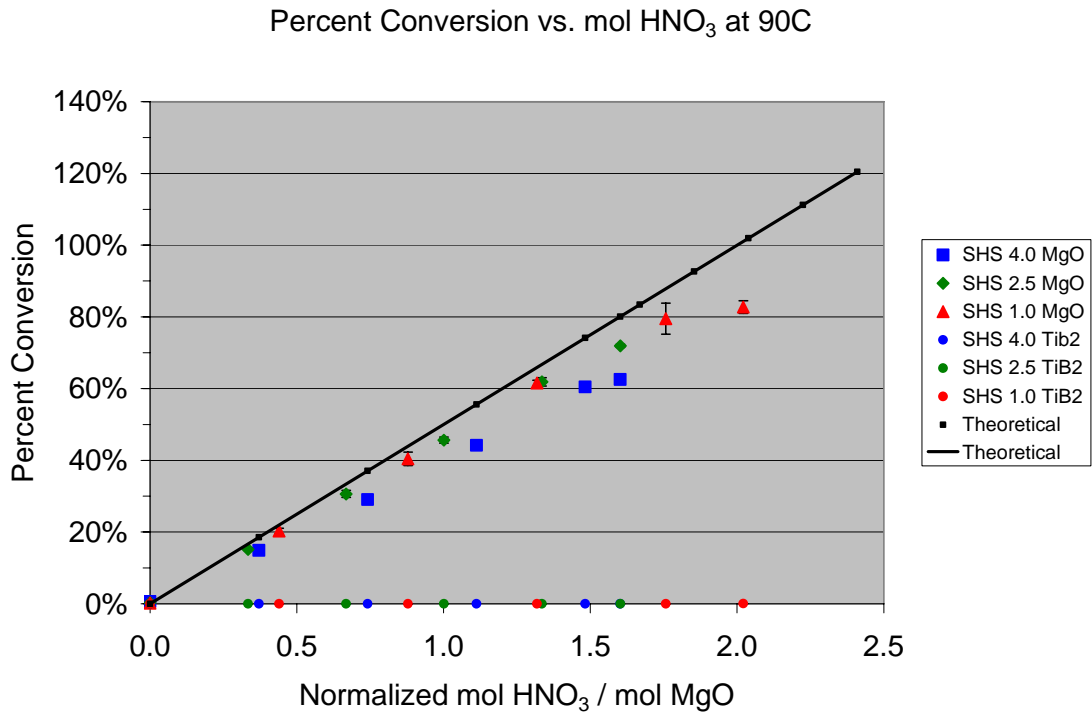


Figure 14: Conversion percentage of SHS produced MgO/TiB<sub>2</sub> from ICP-MS

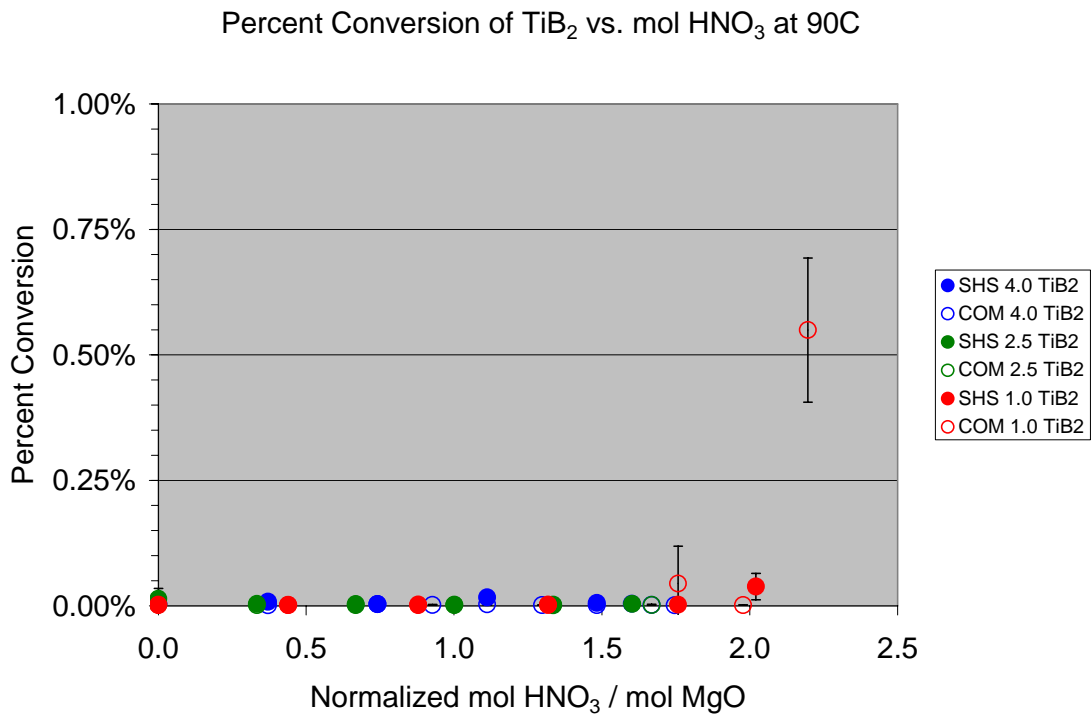


Figure 15: Conversion of TiB<sub>2</sub> from leaching commercial and SHS powders at 90°C

#### 4.2.1.1 Second Cycle Leaching

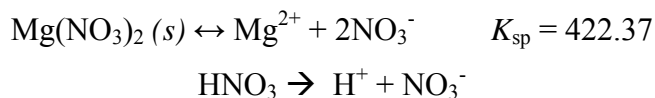
The inhibitive effect of the aqueous solution composition on the leaching process was investigated. If the solubility limit of  $\text{Mg}(\text{NO}_3)_2$  is reached at any point in the leaching process, further dissolution of  $\text{MgO}$  or  $\text{Mg}(\text{OH})_2$  into aqueous  $\text{Mg}(\text{NO}_3)_2$  would be impossible due to solid  $\text{Mg}(\text{NO}_3)_2$  precipitating out of solution. The solubility of a salt can be impacted by the presence of common ions in the aqueous solution. The common ion effect is an application of Le Châtelier's principle where the solubility of a salt is decreased if one of its constituent ions is present in the solution. In the present work, the addition and subsequent dissociation of  $\text{HNO}_3$  into  $\text{H}^+$  and  $\text{NO}_3^-$  ions provide a potential condition for the common ion effect to take place.

The solubility product of the system can be broken down into the three constituents, the oxide ( $\text{MgO}$ ), the hydroxide ( $\text{Mg}(\text{OH})_2$ ), and the aqueous salt, ( $\text{Mg}(\text{NO}_3)_2$ ). The following table summarizes the solubility, molar solubility, and solubility product for each compound.

	<b>MgO</b>	<b>Mg(OH)<sub>2</sub></b>	<b>Mg(NO<sub>3</sub>)<sub>2</sub></b>
<b>Solubility (g/100 ml H<sub>2</sub>O)</b>	0.00062	0.00069	71.2
<b>Molar Solubility (M)</b>	$1.54 \times 10^{-4}$	$1.18 \times 10^{-4}$	4.8
<b>K<sub>sp</sub></b>	$2.36 \times 10^{-8}$	$1.65 \times 10^{-12}$	442.37

Table 2: Solubility properties calculated from handbook values [1]

From the solubility values in the table above, the oxide and hydroxide are relatively insoluble and the aqueous salt is very soluble as expected. The extent of the common ion effect can be calculated based on the following reactions.



The maximum concentration of  $\text{NO}_3^-$  ions in this work was in the minimum pH 1.0 condition in which 0.7195 mol of  $\text{HNO}_3$  was added to 800 ml water, resulting in  $\text{NO}_3^-$  ion concentration of 0.8993M. The effect of  $[\text{NO}_3^-]$  from the dissociation of  $\text{HNO}_3$  on the solubility of  $\text{Mg}(\text{NO}_3)_2$  is calculated below.



Initial Concentration	solid	$\sim 0.0M$	0.8993M
Final Concentration	solid	x	$2x + 0.8993M$

$$K_{sp} = [x] [2x + 0.8993M]^2 = 442.37$$

$$x = [\text{Mg}^{2+}] = 4.505 M$$

The solubility of  $\text{Mg}(\text{NO}_3)_2$  decreases from 4.8M (71.2g/100ml  $\text{H}_2\text{O}$ ) to 4.5M (66.8g/100ml  $\text{H}_2\text{O}$ ) from the addition of the required  $\text{HNO}_3$ . This translates to a maximum solubility of 3.604 mol of  $\text{Mg}^{2+}$  in 800 ml for the minimum pH of 1.0 condition, well above the 0.3597 mol (14.5g) of  $\text{MgO}$  used in these experiments. It can be concluded that despite the decrease in solubility of  $\text{Mg}(\text{NO}_3)_2$  due to the common ion effect of dissociated acid, a saturated solution of  $\text{Mg}(\text{NO}_3)_2$  was not achieved by several orders of magnitude. Therefore, precipitation of solid  $\text{MgO}$  or  $\text{Mg}(\text{OH})_2$  will not occur at the tested leaching conditions.

Pilot experiments of a second washing cycle were run to support or refute the common ion effect on the dissolution of  $\text{MgO}$ . If the equilibrium of Equations 23 and 25 shifts to the left due to the increase of  $\text{Mg}(\text{NO}_3)_2$ ,  $\text{MgO}$  and  $\text{Mg}(\text{OH})_2$  would not react as predicted. For each minimum pH level, the leached powders were dried in an oven at 110°C for 12 hours. The amount of product used in the second cycle was scaled so that the solids concentration was the same as the first washing cycle.

The leaching reactions for the minimum pH of 2.5 and 4.0 were stopped at 80% of total  $\text{MgO}$  dissolution. This was done in an effort to reduce the error involved with leaching times in excess of 12 hours at 90°C in which the solution level varied greatly and additional deionized water had to be added to the system to reestablish a constant

level so that concentration measurements not artificially increase as the leaching solution evaporated.

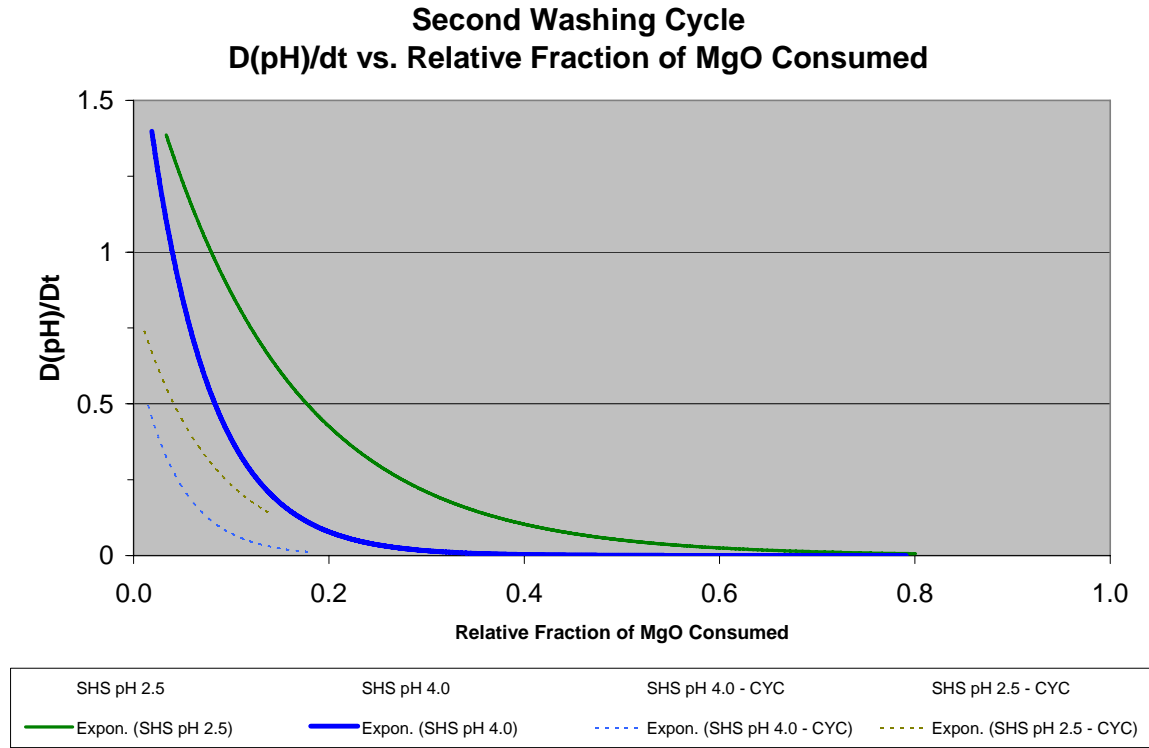


Figure 16: D(pH)/Dt curves of pH 4.0 and 2.5 second cycle plotted versus relative MgO moles

	<b>pH 4.0 SHS</b>	<b>pH 4.0 CYC</b>	<b>pH 2.5 SHS</b>	<b>pH 2.5 CYC</b>
<b>R<sup>2</sup></b>	0.9400	0.9253	0.9356	0.7148

Table 3: R<sup>2</sup> values for D(pH)/Dt curves of pH 4.0 and 2.5 second leaching cycles

The D(pH)/Dt trends are explained in greater detail in the following sections, however, empirical observation of the change in pH between the pH levels of 4.0 and 2.5 indicate that the rate dissolution of MgO continued where the first cycle ended (see Figure 38 inset). This observation agrees with the assertion that the presence of Mg(NO<sub>3</sub>)<sub>2</sub> in the solution does not inhibit further reaction of MgO and HNO<sub>3</sub>. For the pH 1.0 case, essentially all the MgO was reacted in the first leaching cycle, and only two

additions of acid were required for the second cycle. Thus there is no  $D(\text{pH})/Dt$  trend data available for the pH 1.0 second leaching cycle.

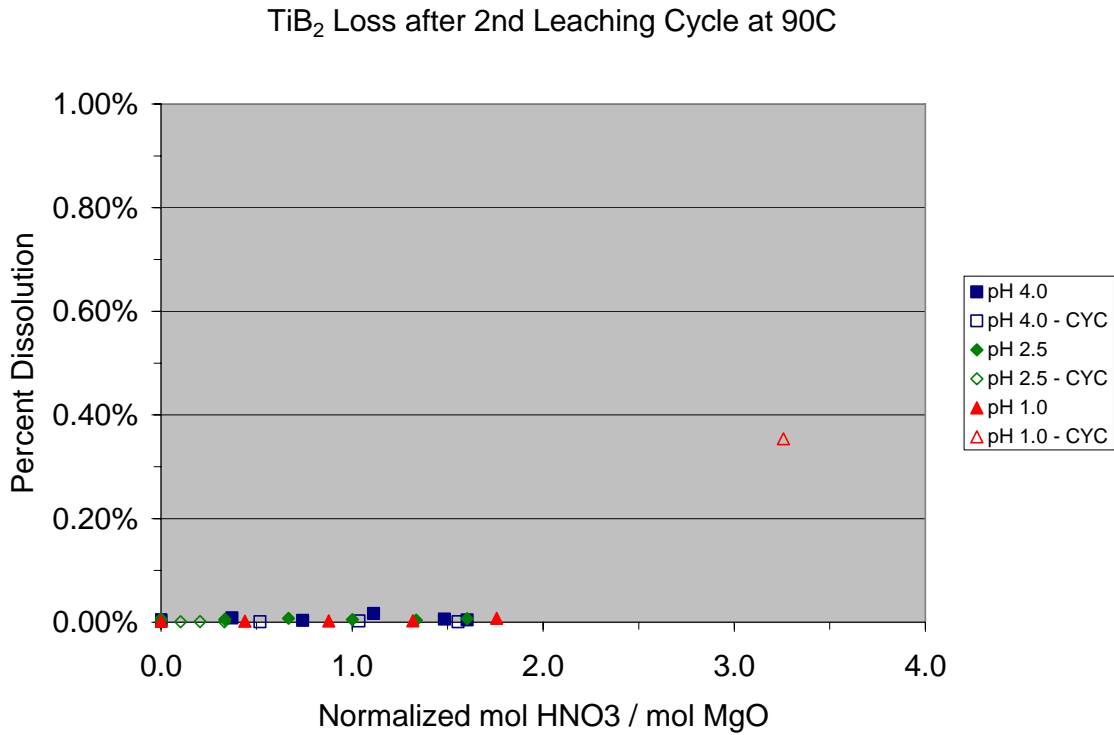


Figure 17: Percent dissolution of SHS Produced TiB<sub>2</sub> during second leaching cycle

The percent dissolution of TiB<sub>2</sub> for the second washing cycle runs (CYC) are plotted with the percent dissolution for the single leach runs. A second leaching cycle did not significantly result in dissolution of TiB<sub>2</sub> for the minimum 2.5 and 4.0 pH levels, and less than 0.40% of TiB<sub>2</sub> for the minimum pH 1.0 experiment.

#### 4.2.2 SEM/EDS

SEM micrographs and EDS spectra were taken of the SHS powders leached at 90°C for each minimum pH level. The accompanying EDS spectra show varying degrees of MgO left in the sample. The as-milled powders show some TiB<sub>2</sub> incased in the MgO cement even after 20 hours of milling. Leaching at 90C at a minimum pH level of 2.5 appeared to have the optimal results for MgO dissolution and TiB<sub>2</sub> retention.

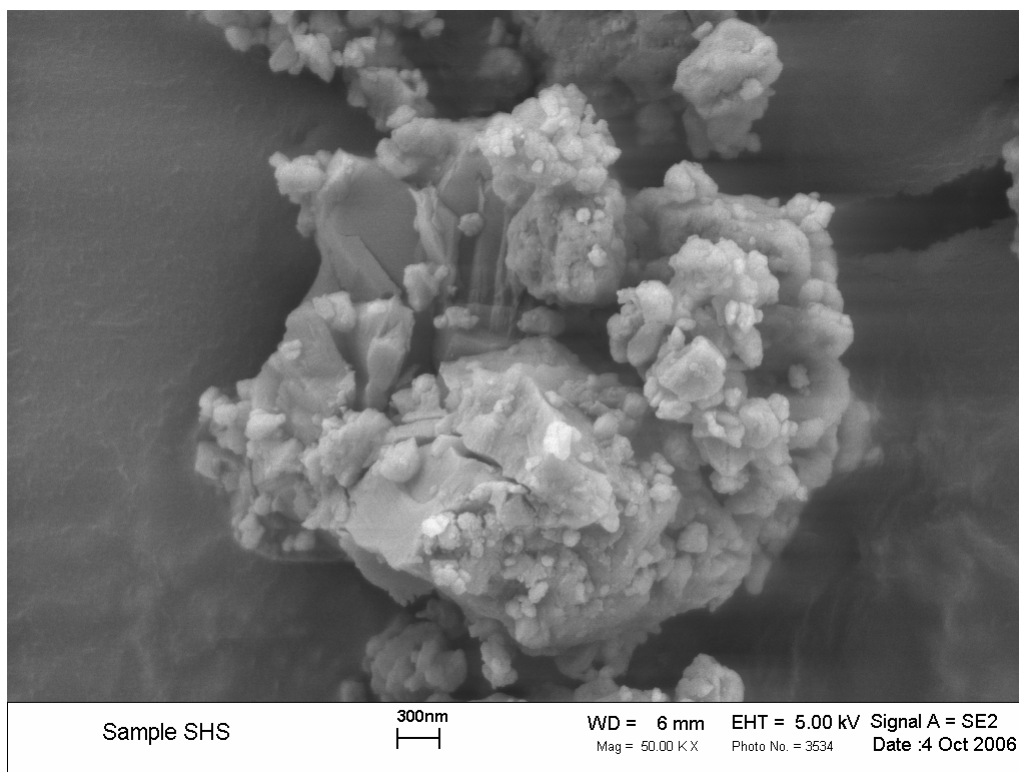


Figure 18: As-milled SHS MgO/TiB<sub>2</sub> prior to leaching - 50,000x

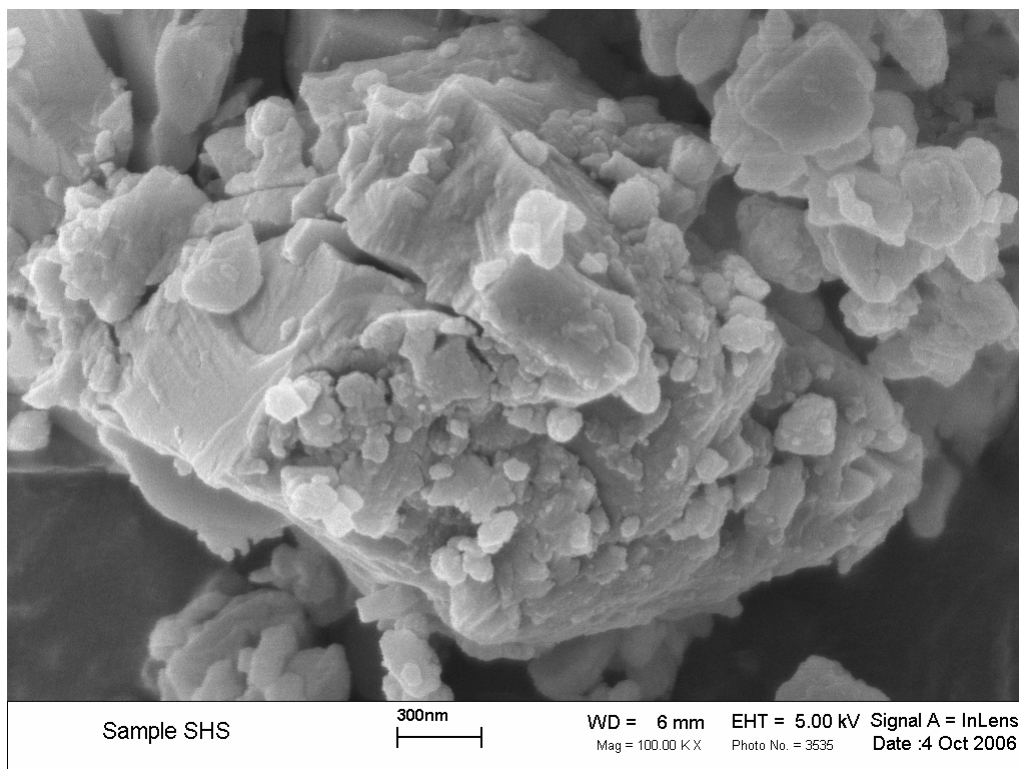


Figure 19: As-milled SHS MgO/TiB<sub>2</sub> prior to leaching - 100,000x

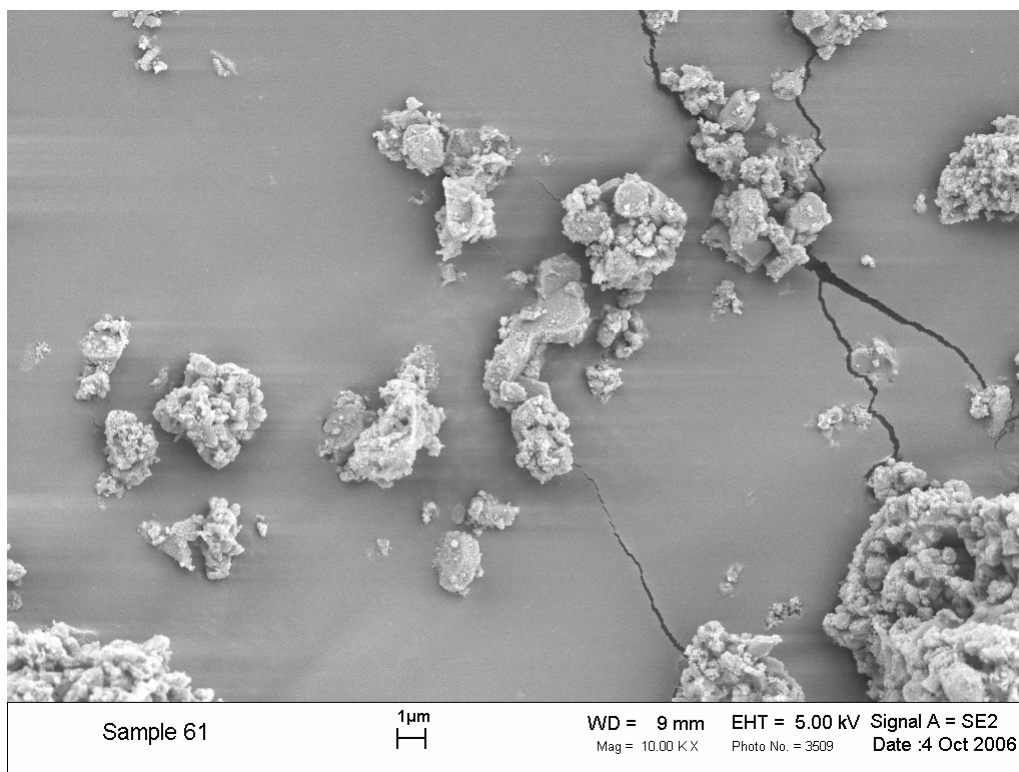


Figure 20: SHS TiB<sub>2</sub> leached at minimum pH 4.0 at 90°C – 10,000x

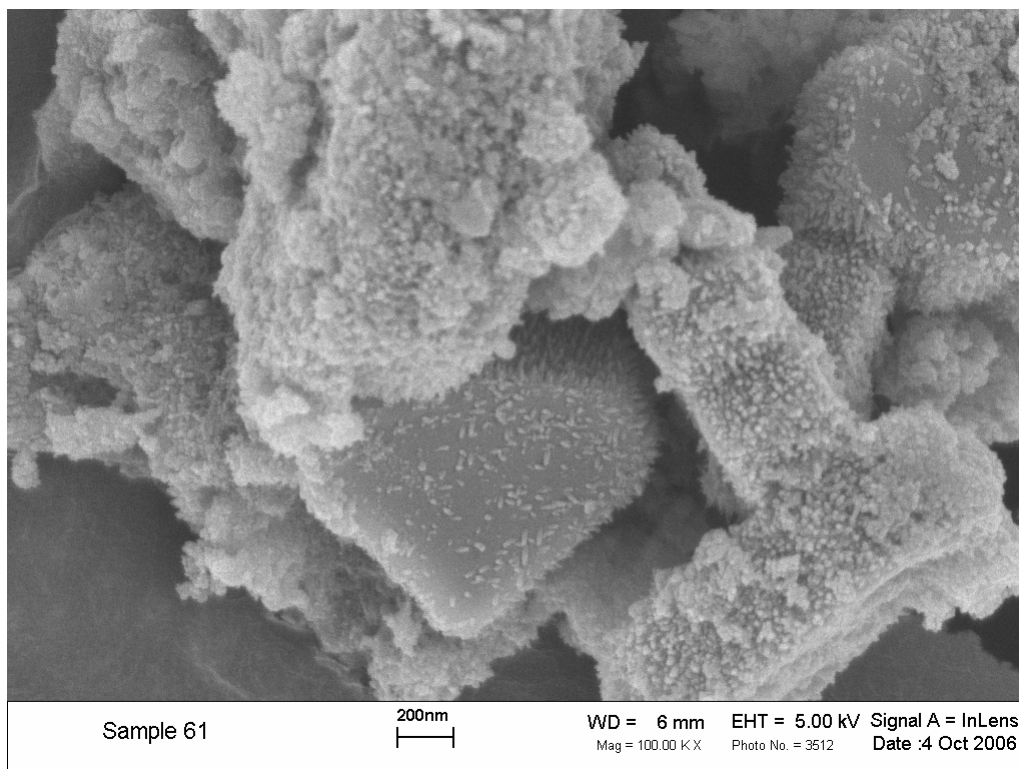


Figure 21: SHS TiB<sub>2</sub> leached at minimum pH 4.0 at 90°C - 100,000x

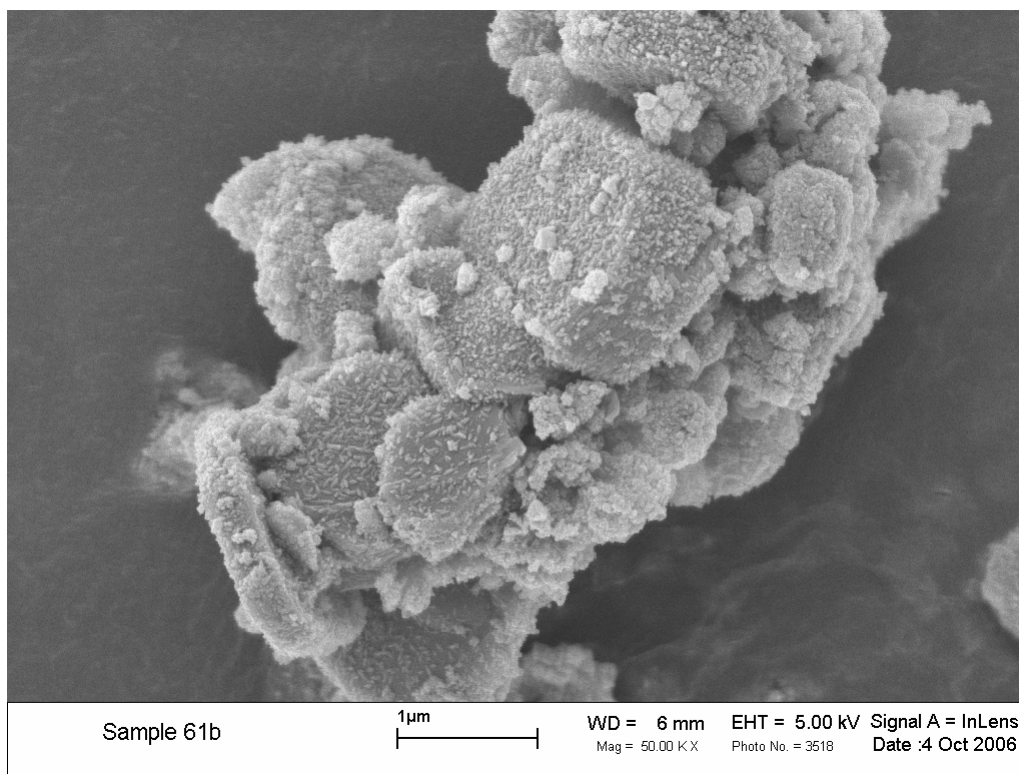


Figure 22: SHS TiB<sub>2</sub> leached at minimum pH 4.0 at 90°C - Second Cycle – 50,000x

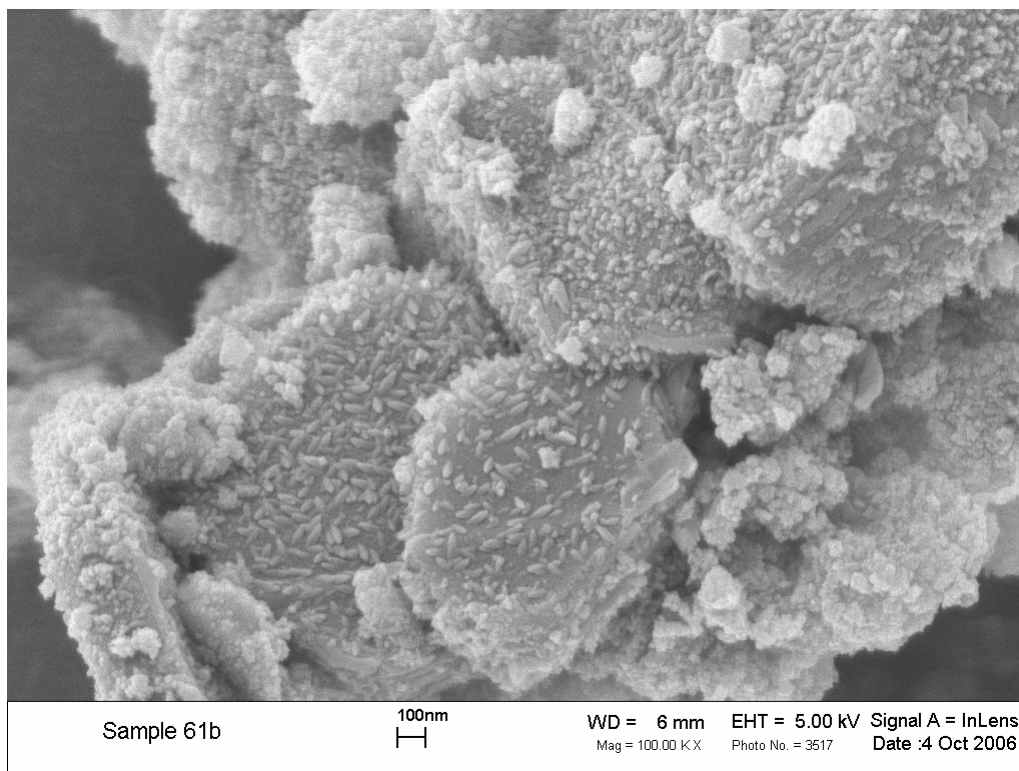


Figure 23: SHS TiB<sub>2</sub> leached at minimum pH 4.0 at 90°C - Second Cycle – 100,000x

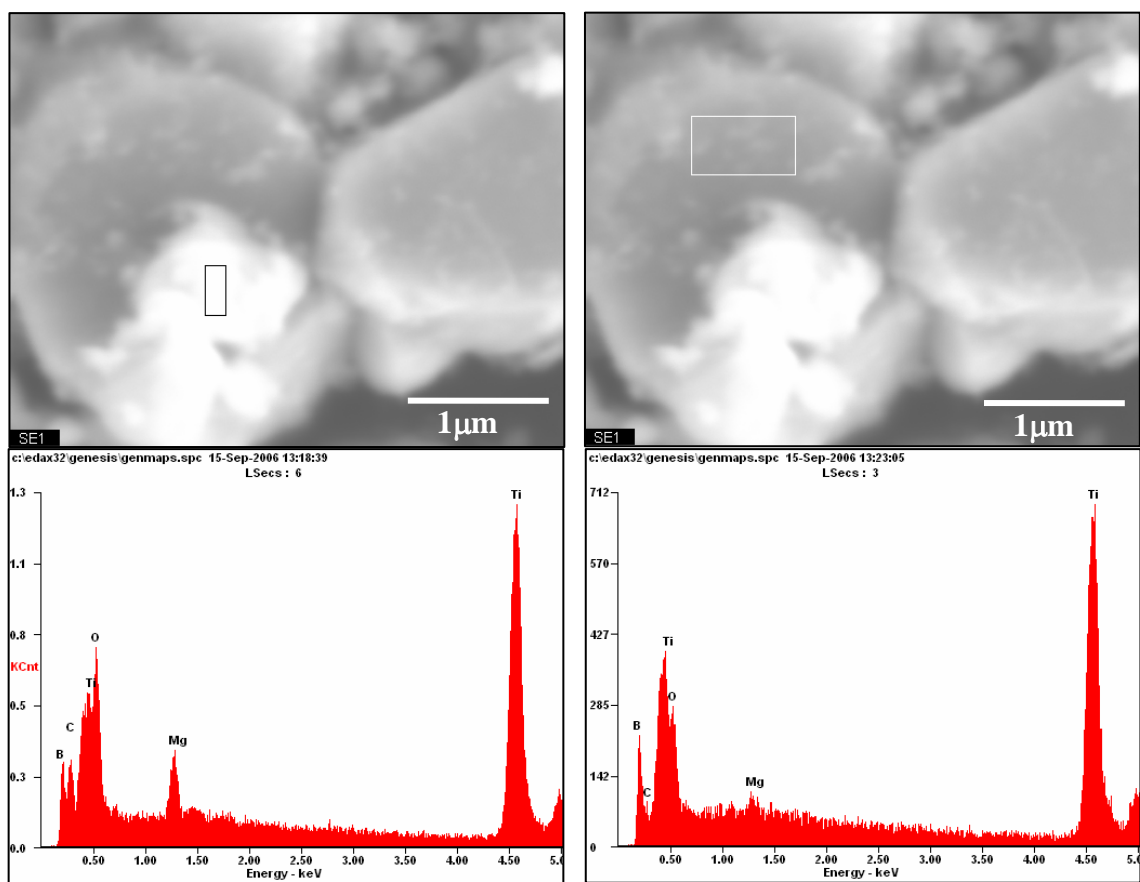


Figure 24: EDS spectra of SHS TiB<sub>2</sub> leached at minimum pH 4.0 at 90°C

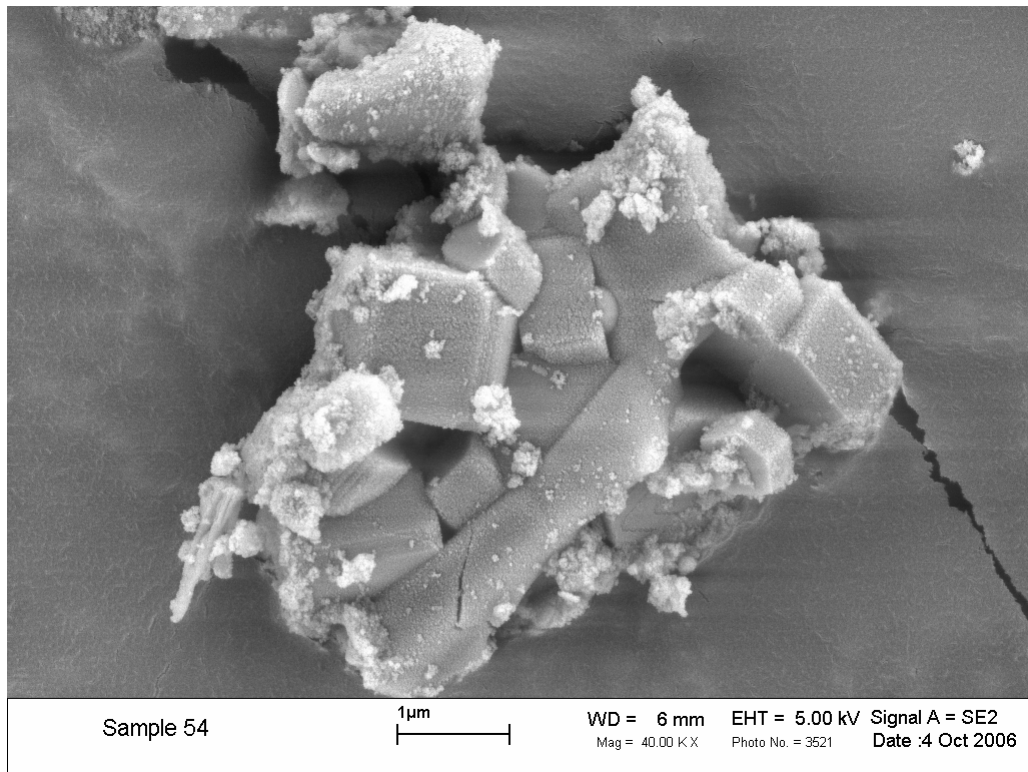


Figure 25: SHS TiB<sub>2</sub> leached at minimum pH 2.5 at 90°C – 50,000x

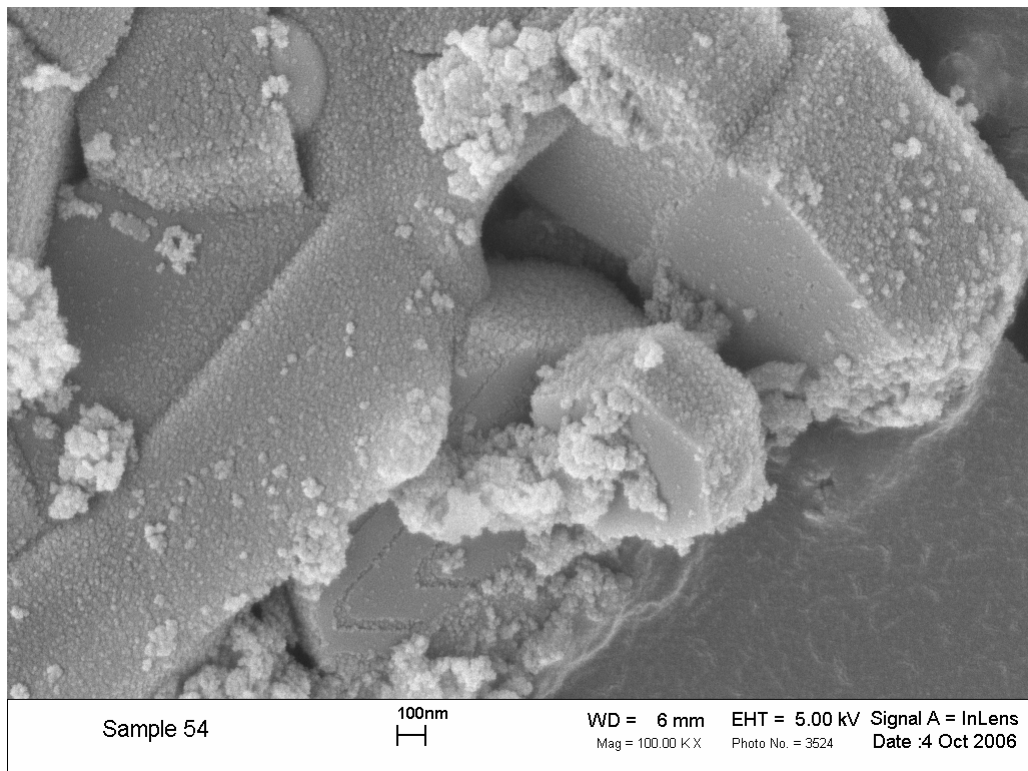


Figure 26: SHS TiB<sub>2</sub> leached at minimum pH 2.5 at 90°C – 100,000x

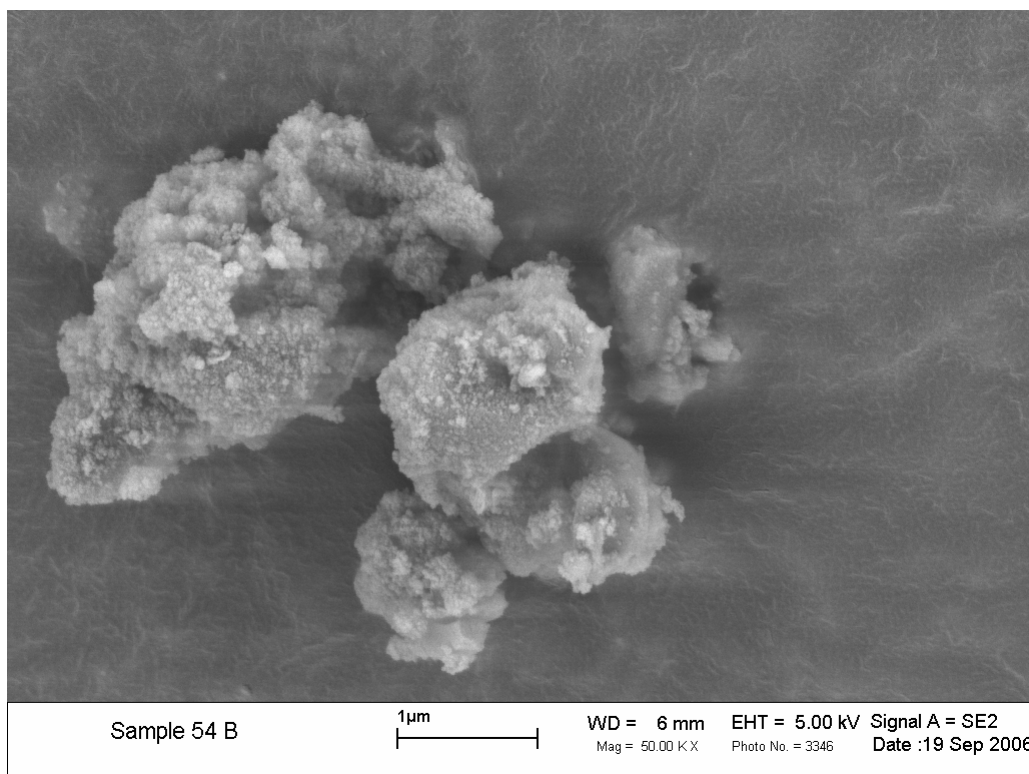


Figure 27: SHS TiB<sub>2</sub> leached at minimum pH 2.5 at 90°C – Second Cycle– 50,000x

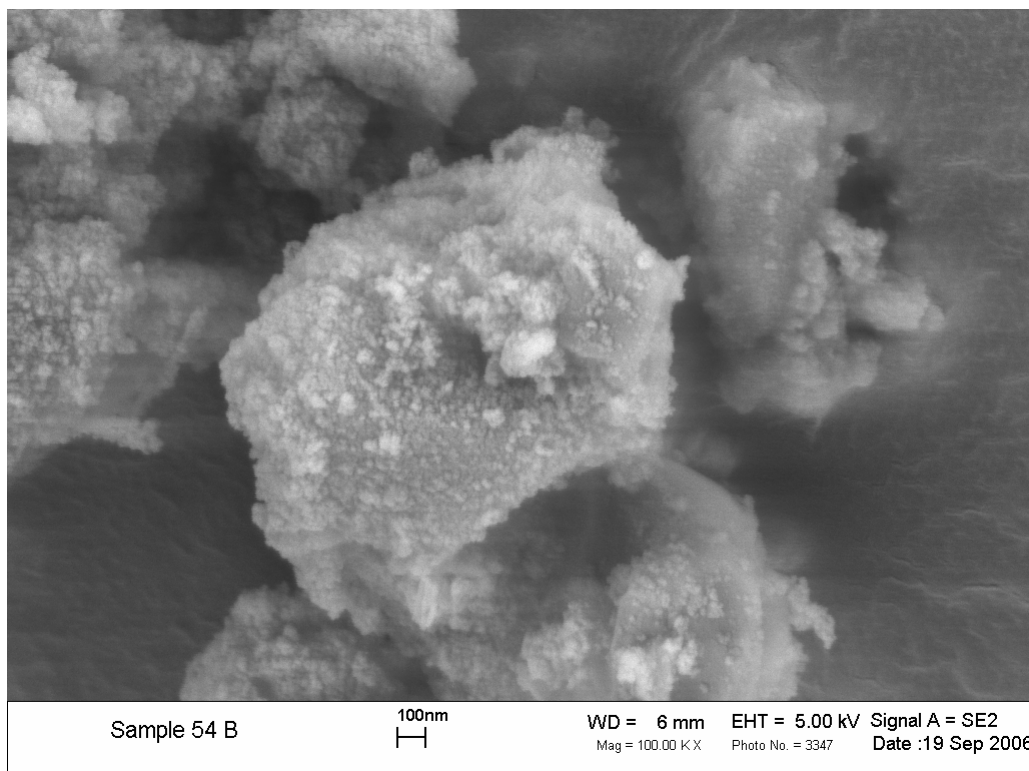


Figure 28: SHS TiB<sub>2</sub> leached at minimum pH 2.5 at 90°C – Second Cycle – 100,000x

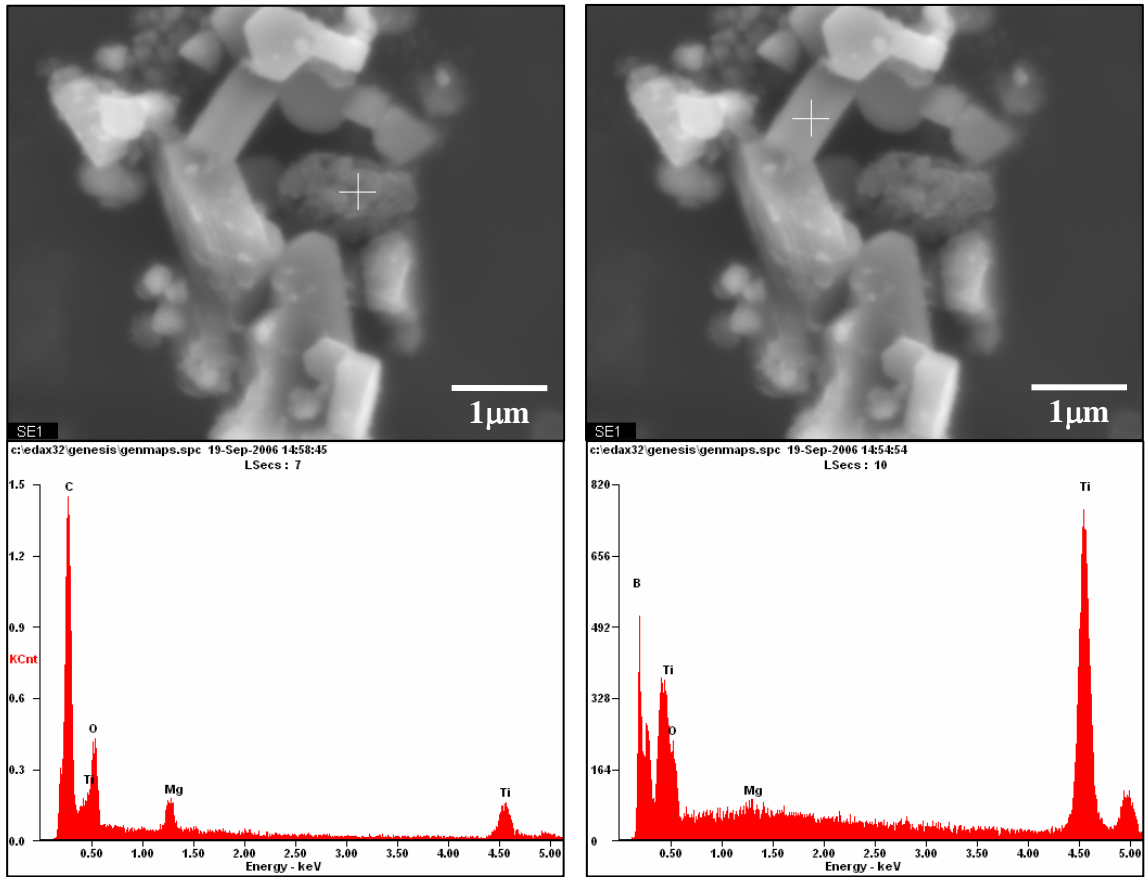


Figure 29: EDS spectra of SHS TiB<sub>2</sub> leached at minimum pH 2.5 at 90°C

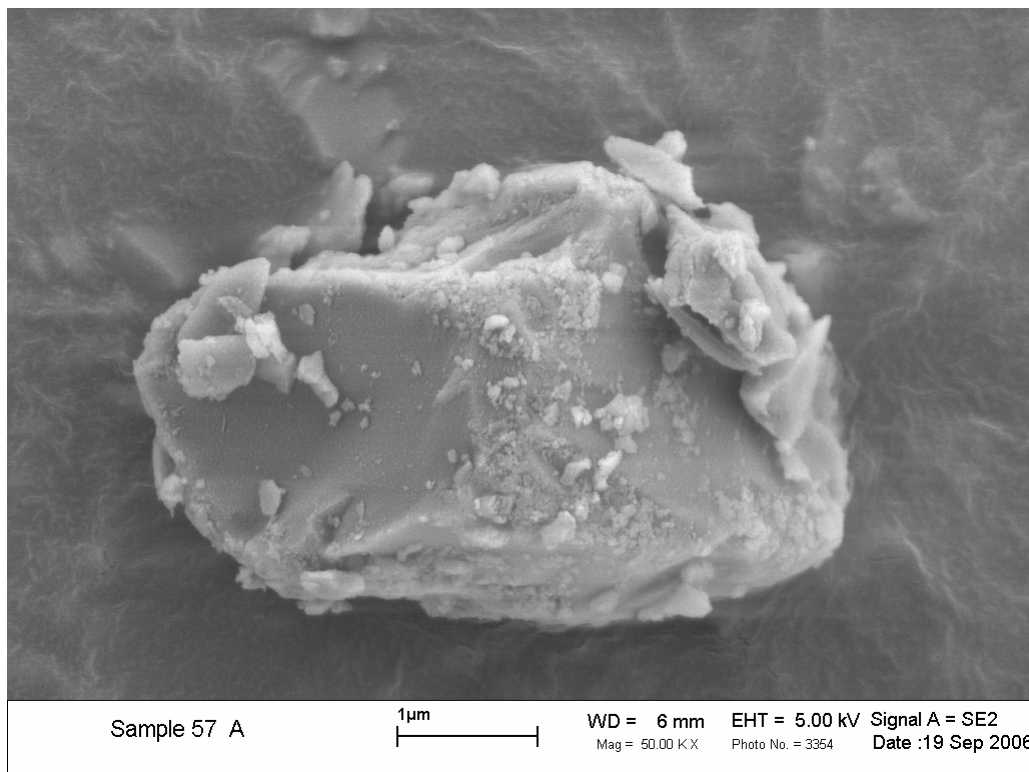


Figure 30: SHS TiB<sub>2</sub> leached at minimum pH 1.0 at 90°C – 50,000x

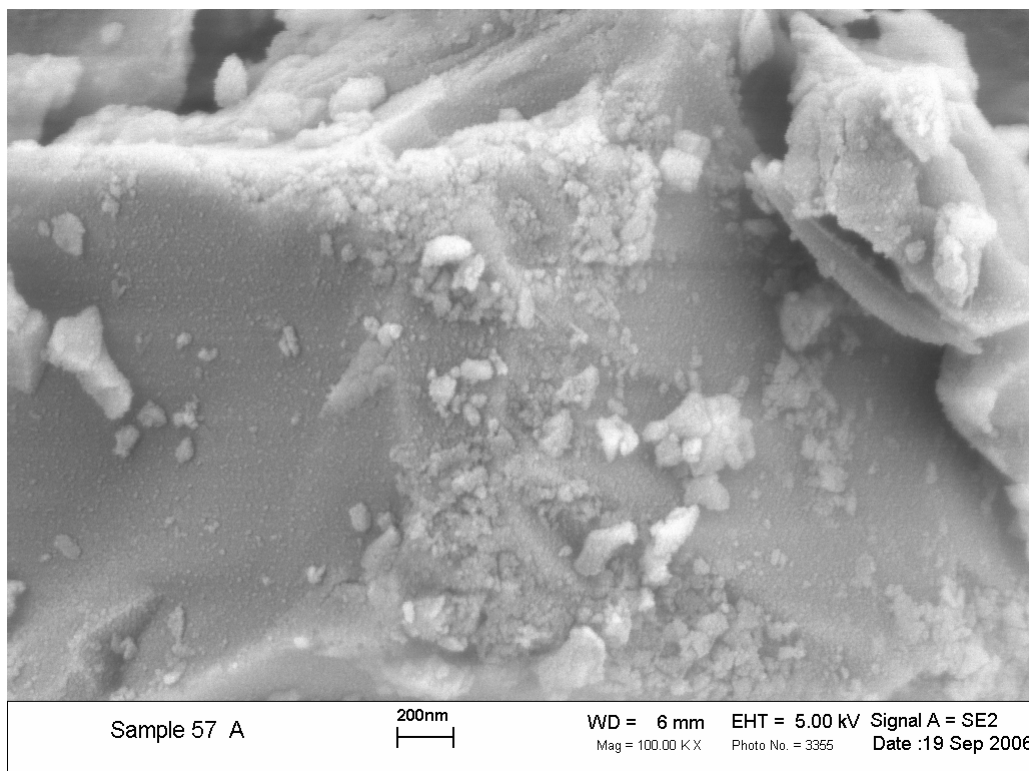


Figure 31: SHS TiB<sub>2</sub> leached at minimum pH 1.0 at 90°C – 100,000x

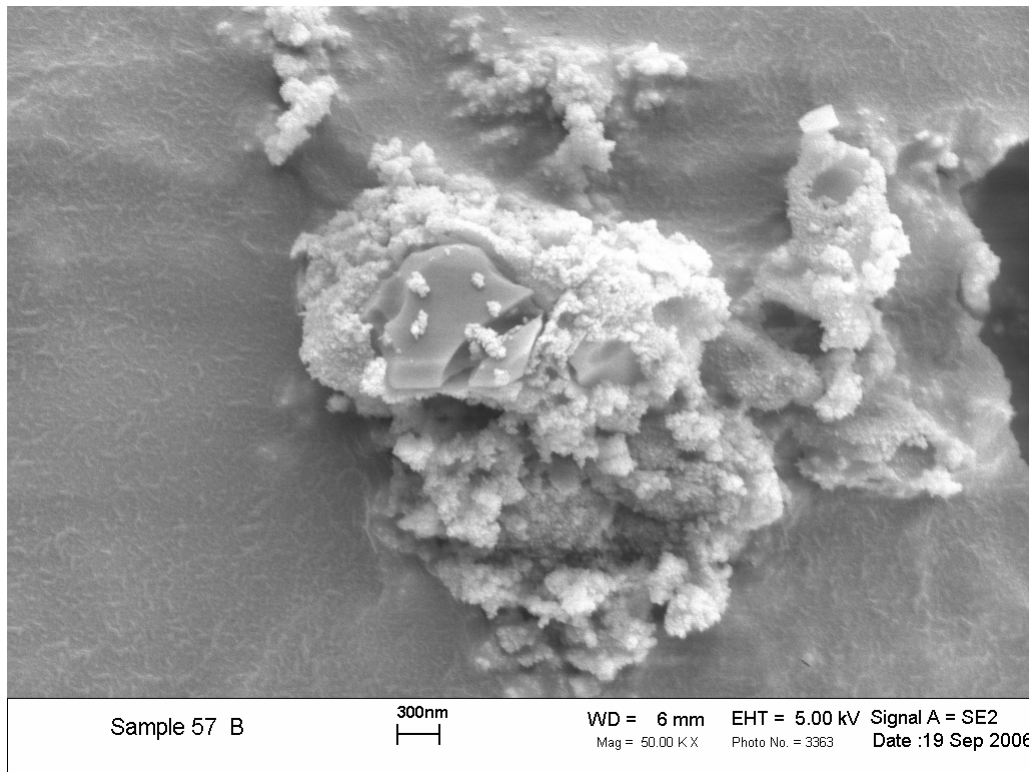


Figure 32: SHS TiB<sub>2</sub> leached at minimum pH 1.0 at 90°C – Second Cycle – 50,000x

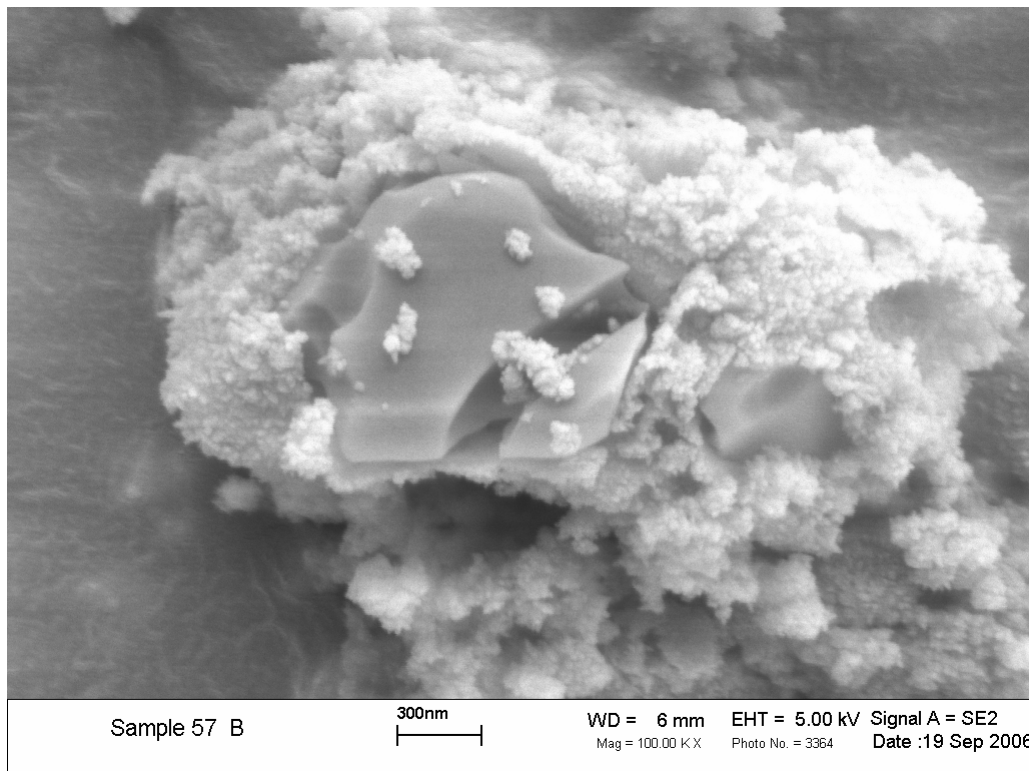


Figure 33: SHS TiB<sub>2</sub> leached at minimum pH 1.0 at 90°C – Second Cycle – 100,000x

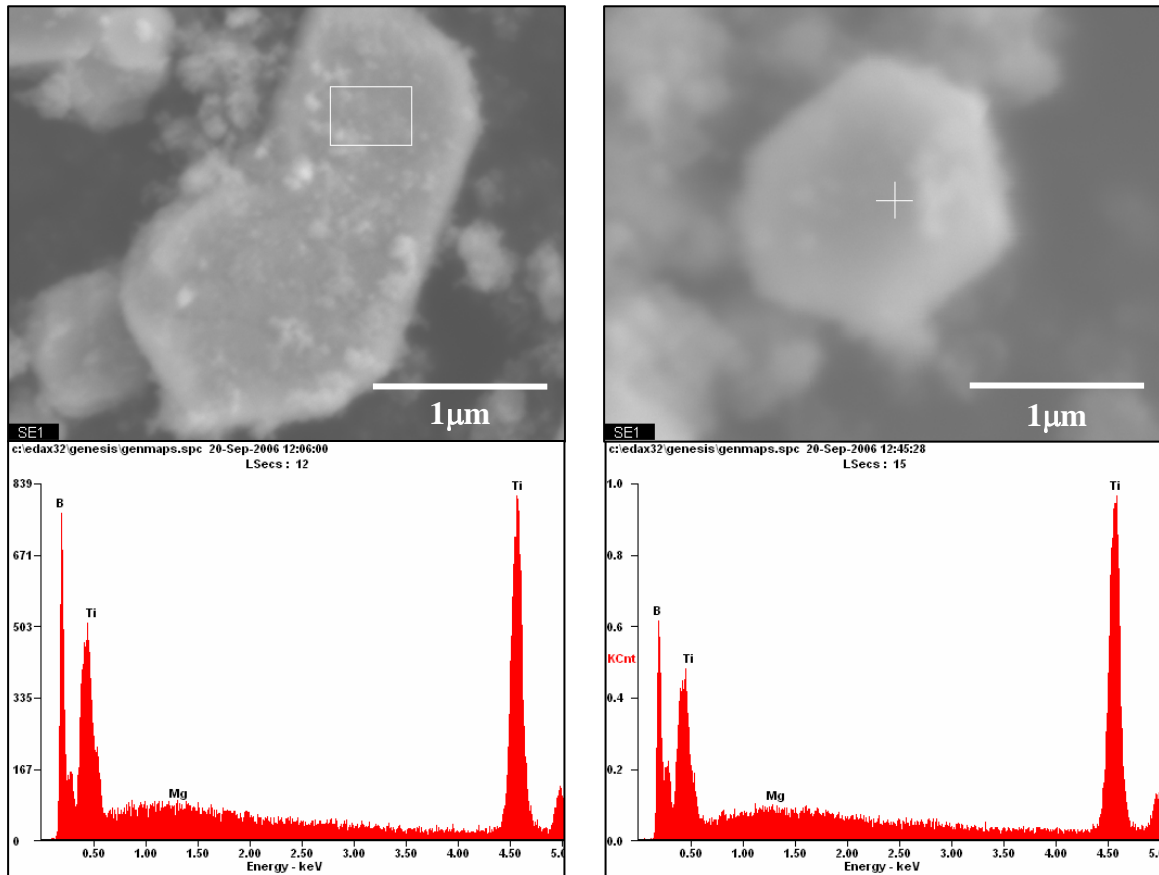


Figure 34: EDS spectra of SHS  $\text{TiB}_2$  leached at minimum pH 1.0 at  $90^\circ\text{C}$

The surface features shown in the pH 4.0 and 2.5 SEM images appear to be oxide derivatives present after 80% leaching. The EDS spectra of pH 1.0 products in Figure 34 indicate fewer oxide compounds present after 100% theoretical leaching. The surface features on the as-received commercial  $\text{TiB}_2$  (Figure 44) suggests the presence of impurities.

The surface features present on each of the pH targets indicate  $\text{TiB}_2$  had been attacked to varying degrees. In the pH 4.0 case, unidentified compounds cover the surface, making observation of the surface texture not possible. For the pH 2.5 target, the surface texture shows evidence of apparent  $\text{TiB}_2$  attack. The minimum pH 1.0 case shows similar unidentified compounds on the surface. In all cases, the second leaching cycle likely resulted in further conversion of  $\text{TiB}_2$  into unidentified compounds. Evidence of this is investigated using powder XRD.

### 4.2.3 XRD

Powder x-ray diffraction was used to determine the evidence of byproducts from non-stoichiometric reaction conditions. A standard Cu-K $\alpha$  pattern shows the relative amounts of MgO and TiB<sub>2</sub> as the powders were leached. The peaks have been identified and indexed.

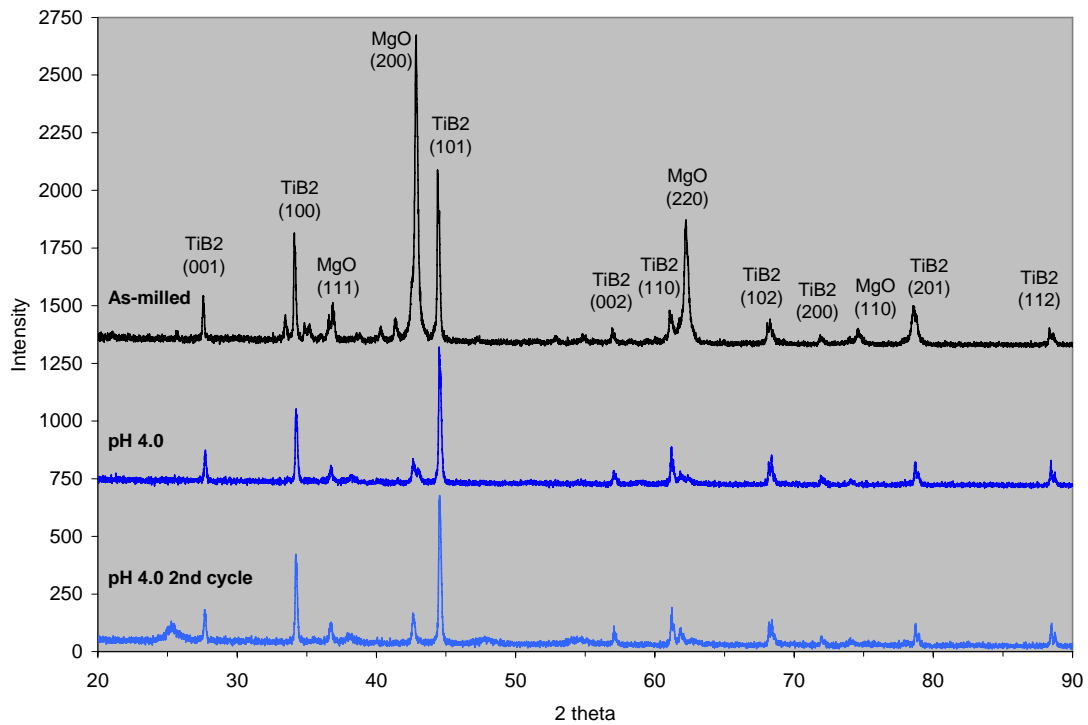


Figure 35: Powder x-ray diffraction scan for minimum pH 4.0 leaching

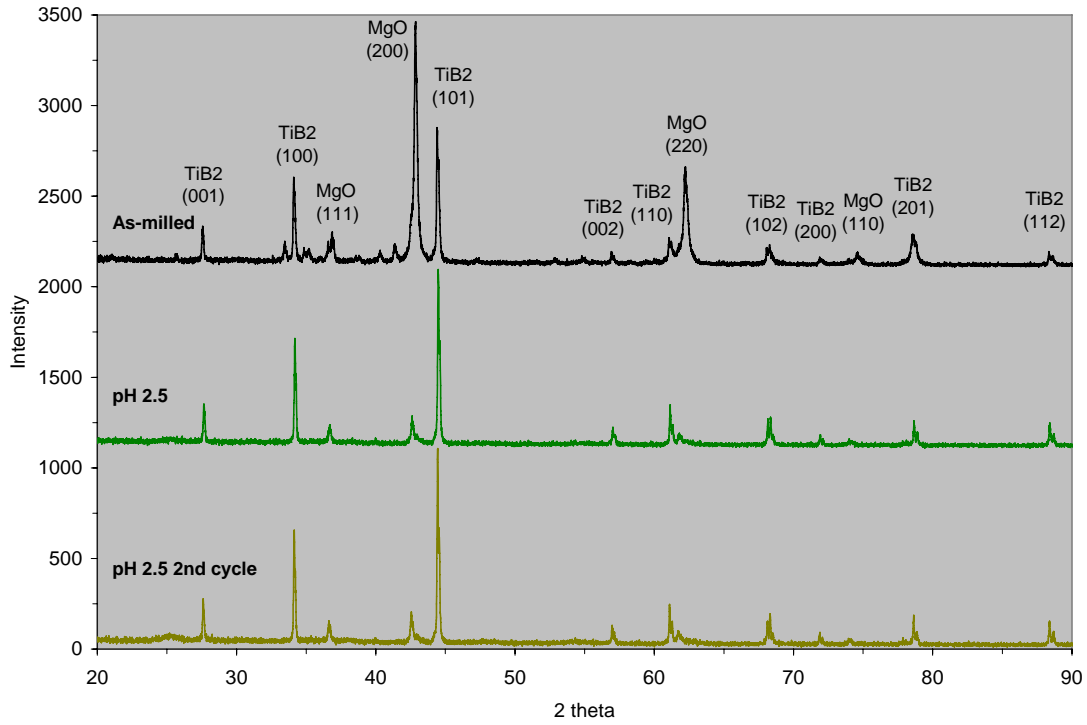


Figure 36: Powder x-ray diffraction scan for minimum pH 2.5 leaching

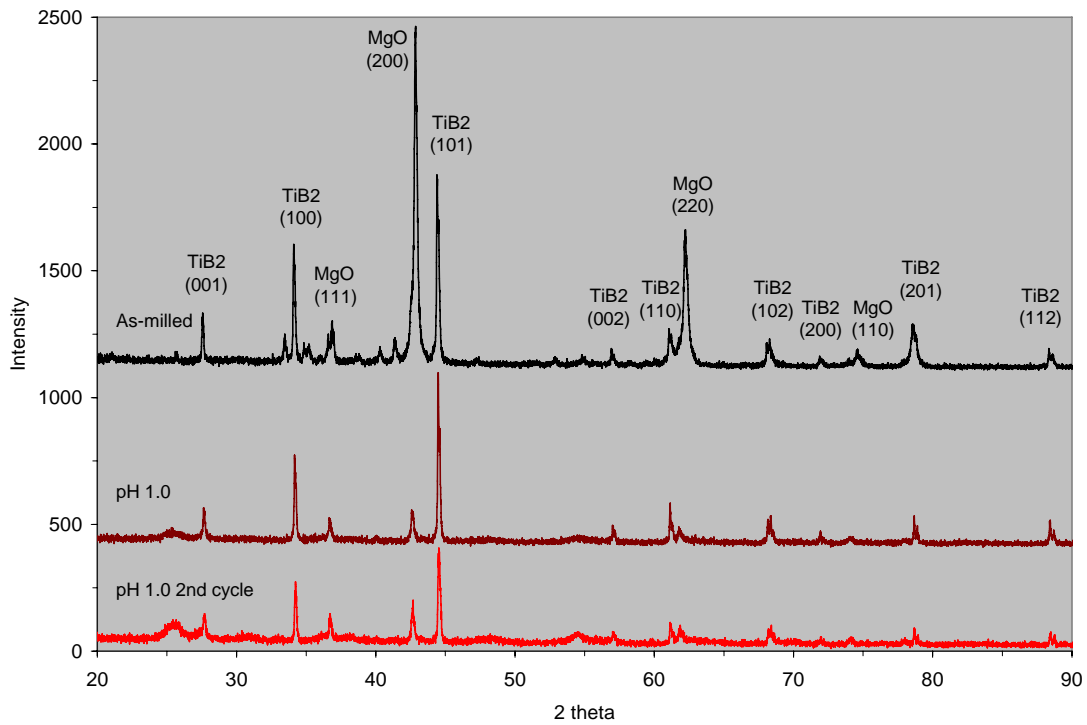


Figure 37: Powder x-ray diffraction scan for minimum pH 1.0 leaching

The MgO (200) and (111) planes in each case were not completely diminished, indicating MgO was not completely leached. At a minimum pH of 4.0 and 2.5, this was expected since acid additions were performed until 80% of theoretical conversion. In the minimum pH 1.0 tests, HNO<sub>3</sub> was added until the pH did not change significantly. Figure 84 and Figure 85 in the Appendix confirm this behavior. This suggests agglomerates were affecting the leaching rate. The unidentified broadening feature at 26° (2-theta) in each of the second leaching cycle scans show the presence of an amorphous compound or species at the nanometer scale. The lack of Ti ions from ICP-MS analysis, the unidentified broad peak, and the relative reduction in the TiB<sub>2</sub> (101) and (100) planes indicate a conversion of TiB<sub>2</sub> occurred. This behavior was observed during the second leaching cycle for all samples, and during the first leaching at a minimum pH of 1.0.

### 4.3 Qualitative Comparisons

#### 4.3.1 $D(pH)/Dt$

The difference in pH over the difference in time recorded by the pH meter revealed an initial exponential change. However, due to experimental constraints, the system became alkaline from the conversion of MgO to Mg(OH)<sub>2</sub>. The change in pH is influenced by the neutralization reaction.



The amount of acid required for dissolution of MgO remains the same due to equal stoichiometric ratios between MgO/Mg(OH)<sub>2</sub> and HNO<sub>3</sub>. This is observed by the following reactions.



The conversion of MgO into its hydroxide form is favorable at the elevated temperatures of leaching. Such conversion has been studied by Rocha *et al.* and illustrated in **Error! Reference source not found.**. It is shown in the powder XRD scans that Mg(OH)<sub>2</sub> peaks were not detected in the SHS leached products. The neutralization reaction occurring at the same time with Equation 25 influences the D(pH)/Dt determination.

**D(pH)/Dt vs. Fraction MgO Consumed at 90C**

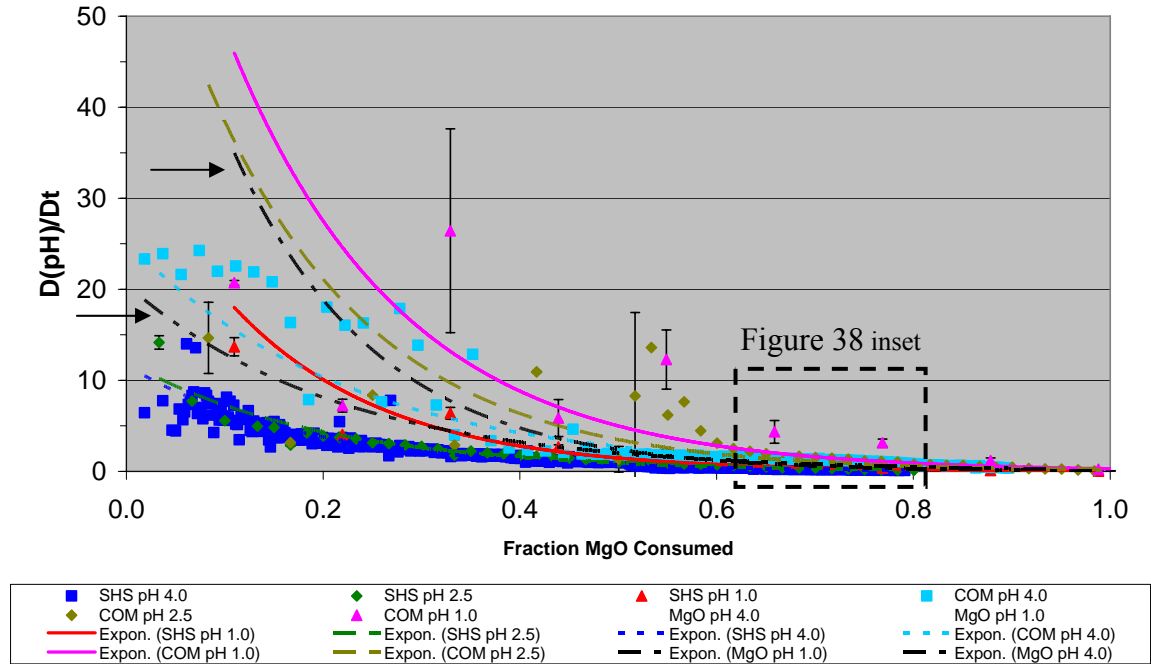


Figure 38: D(pH)/Dt for all powders at 90C. Indicated with arrows, the single-hashed and double-hashed lines represent leaching of commercial MgO-only at pH 4.0 and pH of 1.0, respectively.

	Stoich Commercial Mix			SHS MgO/TiB <sub>2</sub>			MgO only	
Min pH	4.0	2.5	1.0	4.0	2.5	1.0	4.0	1.0
R <sup>2</sup>	0.9149	0.7677	0.7663	0.9578	0.9612	0.9311	0.9133	0.6678

Table 4: R<sup>2</sup> values for D(pH)/Dt curves

The dotted, dashed, and solid lines show leaching performed with a minimum pH of 4.0, 2.5, and 1.0 respectively. The relative particle size effects can be observed from the  $D(\text{pH})/Dt$  plots. The cemented aggregate formed from the SHS reaction (Figure 8) inhibits the dissolution of MgO despite the smaller particle size ( $\sim 1\mu\text{m}$ ) compared to the larger commercial particles ( $44\mu\text{m}$ ). This was evident in qualitative comparisons between the SHS trend and the commercial trend at each minimum pH level. At each pH level, the stoichiometric powders exhibited a larger change in pH over the same time interval initially before tapering off as the reaction went to completion.

#### 4.3.2 Average pH

The saw-tooth behavior is characteristic of buffer solutions that resist change to pH. Therefore the minimum pH that has been referred to throughout these experiments is not representative of the average pH for a given leaching condition. The following was determined from pH readings taken every ten seconds. A bell-curve is produced, indicating the average pH being slightly higher than the minimum pH. The log-curve of pH versus moles of acid for a strong acid has a characteristic step-wise behavior which results in a large number of counts near pH of 6.0-7.0. This clustering of counts influences the average pH, and thus only acidic ( $< 4.5$ ) were considered for pH levels of 2.5 and 1.0. For the 4.0 minimum pH conditions, the average pH peak is observed closer to the neutral cluster of peaks. The focus on lower pH is appropriate since this is the region of interest in acid dissolution. The relative heights are not indicative of kinetic behavior since different quantities of initial powders were used. However, the following is applicable to leaching at a constant pH using a pH-stat to control the  $[\text{H}^+]$  of the system.

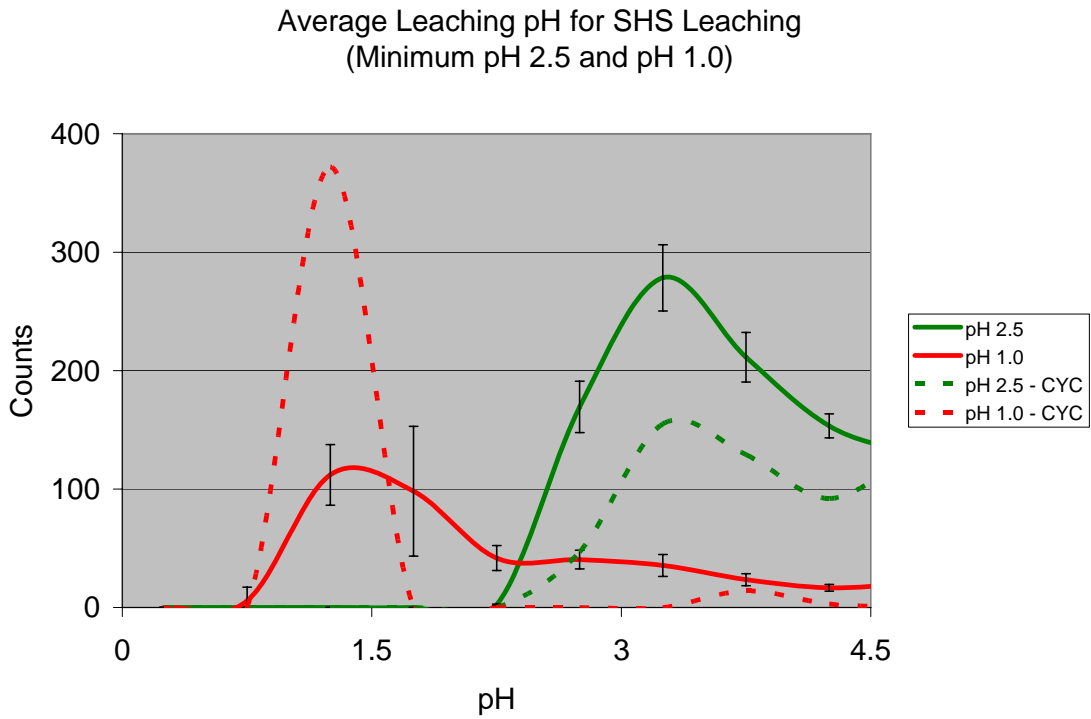


Figure 39: Average pH for minimum pH levels 2.5 and 1.0 including second cycle

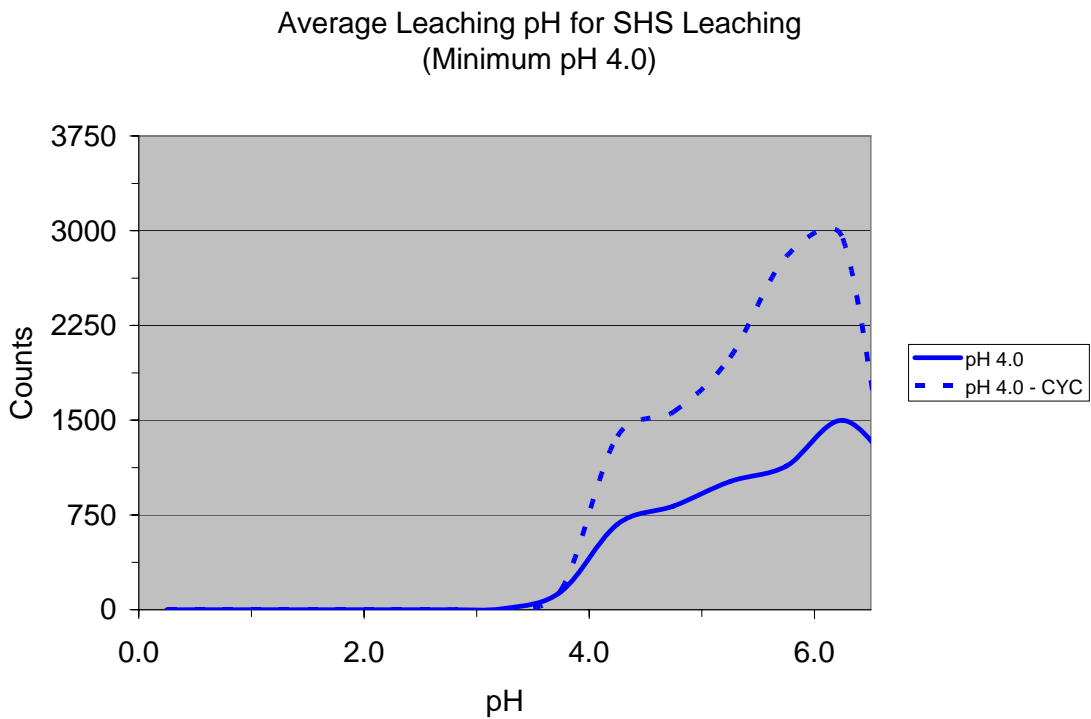


Figure 40: Average pH for minimum pH level 4.0 including second cycle

Leaching with a minimum pH of 2.5 resulted in an average pH in the 2.5-4.5 range for both cycles of leaching. At the pH 1.0 minimum condition, the average pH was 1.0-1.5 for both cycles. The peaks in the pH 4.0 minimum experiments show an average pH around 4.0-5.0 when the cluster of pH greater than 5.5 is disregarded. When leaching at a fixed pH, with control devices such as a pH-stat, the following table summarizes the recommended pH to reproduce the results from this work.

Minimum pH:	<b>4.0</b>	<b>2.5</b>	<b>1.0</b>
Constant pH:	4.5 ± 0.5	3.0 ± 0.5	1.25.0 ± 0.25

Table 5: Constant pH settings corresponding to the minimum pH used in this work

## **5 CHAPTER FIVE – CONCLUSIONS AND FUTURE WORK**

### **5.1 Optimal Dissolution of MgO and TiB<sub>2</sub>**

It was determined that the MgO byproduct from the magnesium SHS thermite reaction could be effectively removed using acid leaching. Optimal leaching conditions were determined to be at 90°C with a minimum pH of 2.5. This resulted in 83%-84% percent conversion of MgO, and less than 100 ppm of TiB<sub>2</sub> in solution after one leaching cycle. A second leaching cycle incrementally increased the MgO conversion, and did not result in significant dissolution of TiB<sub>2</sub>. The experiments were allowed to leach until specific trends could be established. Precipitation and the common ion effect did not impact the solubility of the aqueous salt, nor did it hamper the dissolution of the unwanted products. This was because of the relative solubility differences in the leaching candidate chosen for the particular system.

### **5.2 Leaching Dynamics of SHS produced MgO/TiB<sub>2</sub>**

From the qualitative observations, it can be inferred the leaching dynamics are influenced by particle size effects around ~70% of MgO consumed. After this point, the D(pH)/Dt trend became linear. This was also inferred from the SEM micrographs taken of the leached products. MgO still encased some of the TiB<sub>2</sub>, requiring more time to attack the MgO and thus decreasing the D(pH)/Dt value. Leaching of the stoichiometric mixture of commercial powders followed a similar trend. The D(pH)/Dt trend for each minimum pH level was higher than the corresponding SHS produced D(pH)/Dt trend.

### **5.3 Proposed Future Work**

Powder XRD revealed the formation of an unidentified compound. The relative reduction in the (101) and (100) planes revealed TiB<sub>2</sub> reacted with the nitric acid, particularly during the second leaching cycle. However, the absence of Ti ions in the liquid solution indicates the formation of another compound. Identification of the solids

would be valuable in determining if the broad peak was due to an amorphous phase or due to particles in the nano-scale.

Throughout the course of this work, time was kept constant and independent of the parameters investigated. With automated temperature control and constant pH during the leaching process using a pH-stat, a kinetic study can be performed on the system to determine the kinetic parameters that govern the speed of the reaction. This study was dictated by the kinetics at work which extended leach times. Determining the optimal kinetic parameters would achieve an optimal leaching process based on  $\text{TiB}_2$  dissolution and time spent leaching.

A mathematical model combining the kinetic and dissolution behavior from this work could be constructed to predict leaching parameters. Product composition from the SHS reaction can vary from one reaction to another. The ability to model the leaching characteristics based on this composition would prove valuable.

## APPENDIX

### A.1 SEM

#### A.1.1 Stock Powders

Micrographs of stock powders used in the SHS reaction and commercial stoichiometric mixture are included here. Particle size analysis is included in A.2.

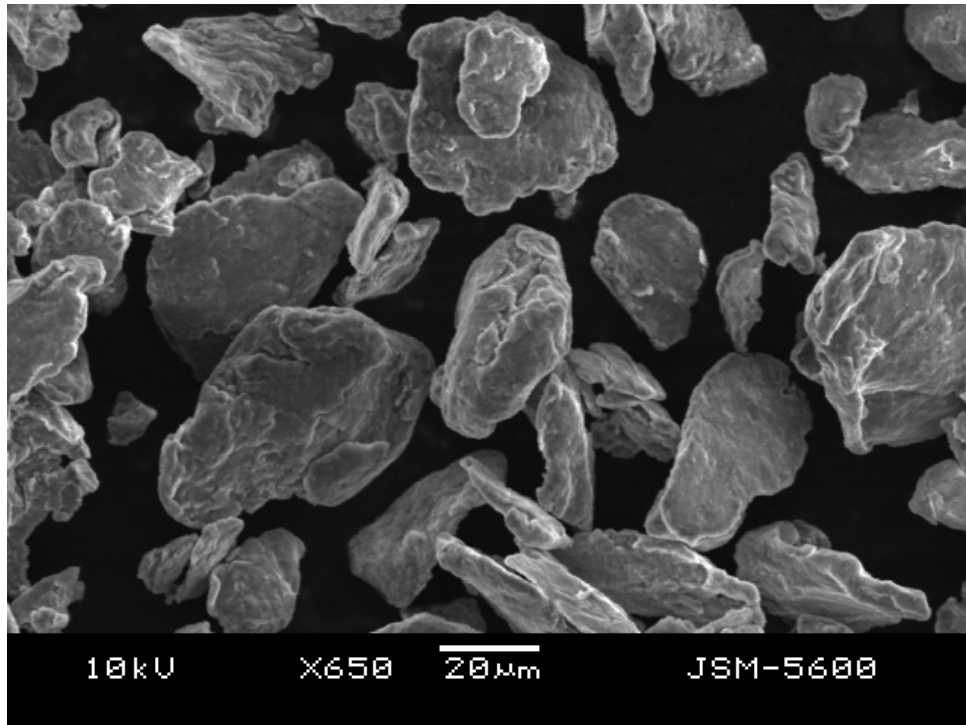


Figure 41: SHS reactant Mg flake at 650x magnification

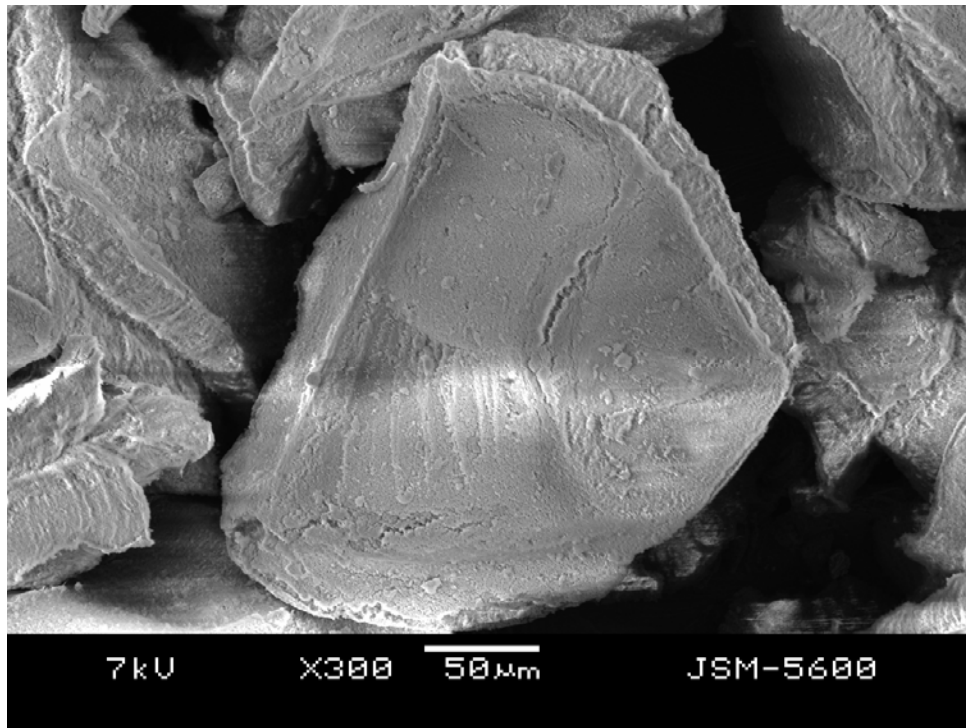


Figure 42: SHS reactant amorphous B<sub>2</sub>O<sub>3</sub> at 300x magnification

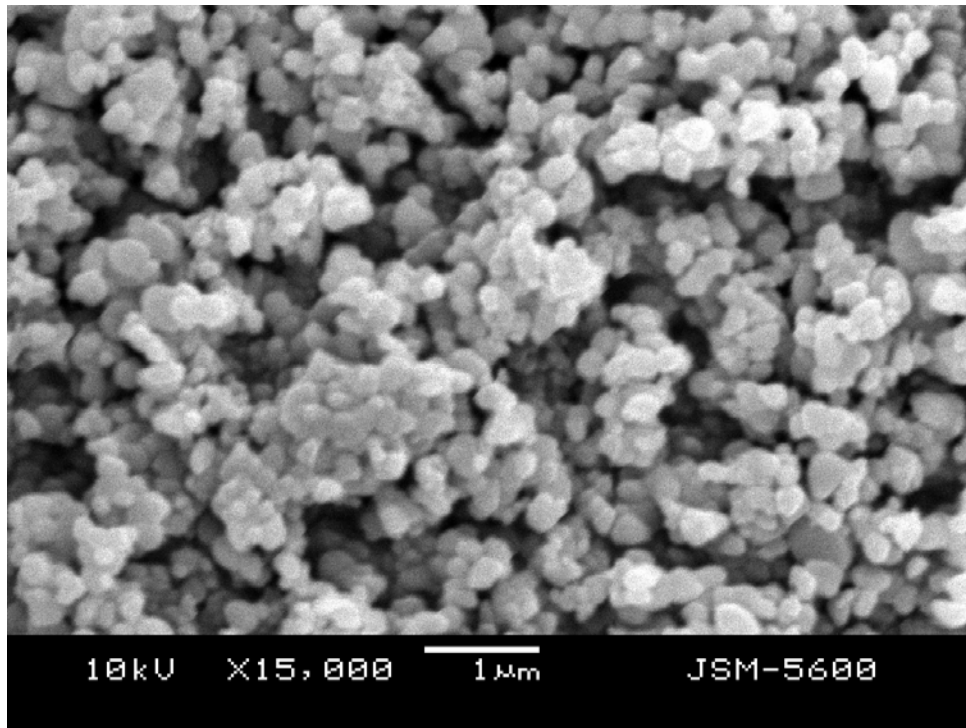


Figure 43: SHS reactant pigment grade TiO<sub>2</sub> at 15,000x magnification

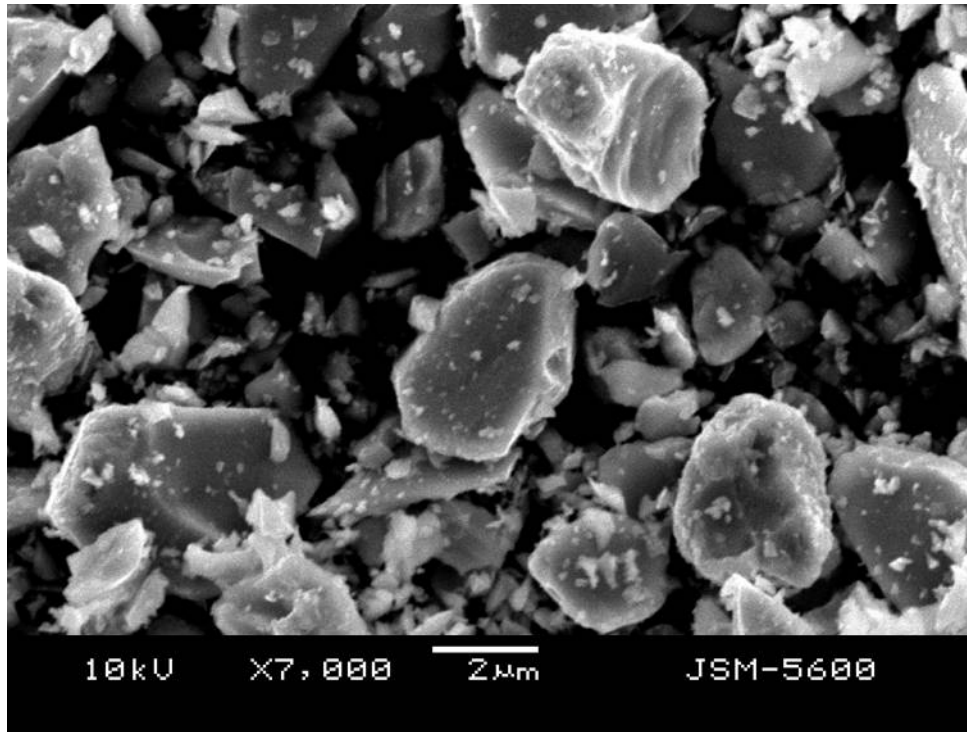


Figure 44: Commercial carbothermic TiB<sub>2</sub> from H.C. Starck at 7,000x magnification

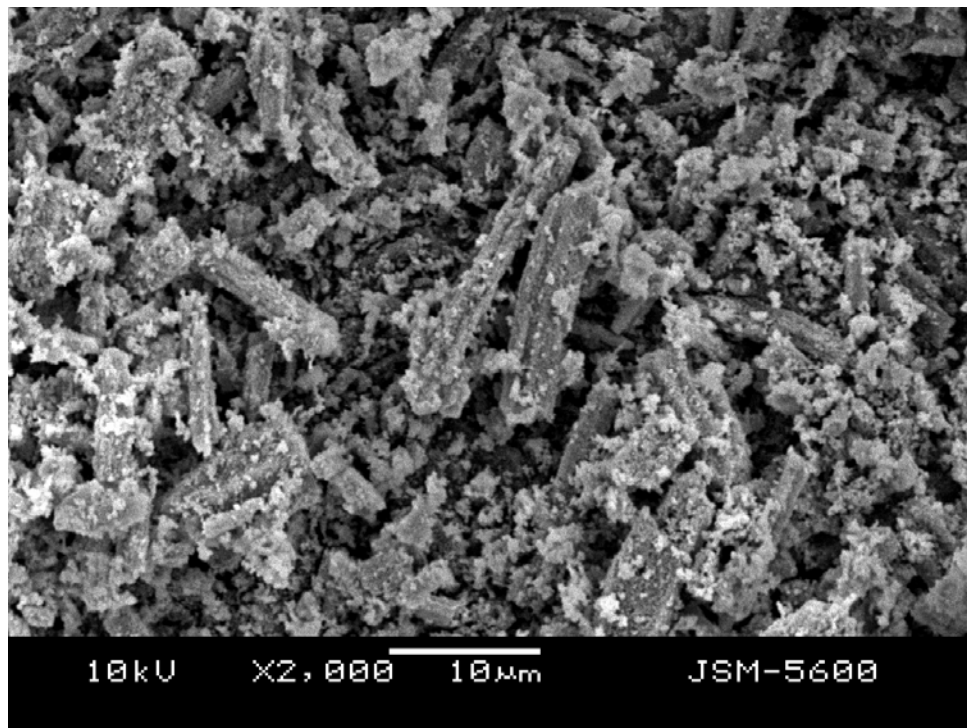


Figure 45: Commercial MgO used in stoichiometric mixture at 2,000x magnification

### A.1.2 Ball Milling

As-reacted 38.9g batch milled to determine optimal milling time. Milling was performed in a 4.92L Type 304 stainless steel milling jar with 1.27cm Type 302/304 stainless steel balls. Micrographs were selected from samples were taken at 0 hrs, 2 hrs, 4 hrs, 6 hrs, 8 hrs, 12 hrs, 18 hrs, 24 hrs, and 30 hrs. Optimal milling was determined to be about 18 hours. Further milling did not reduce the particle size beyond this point.

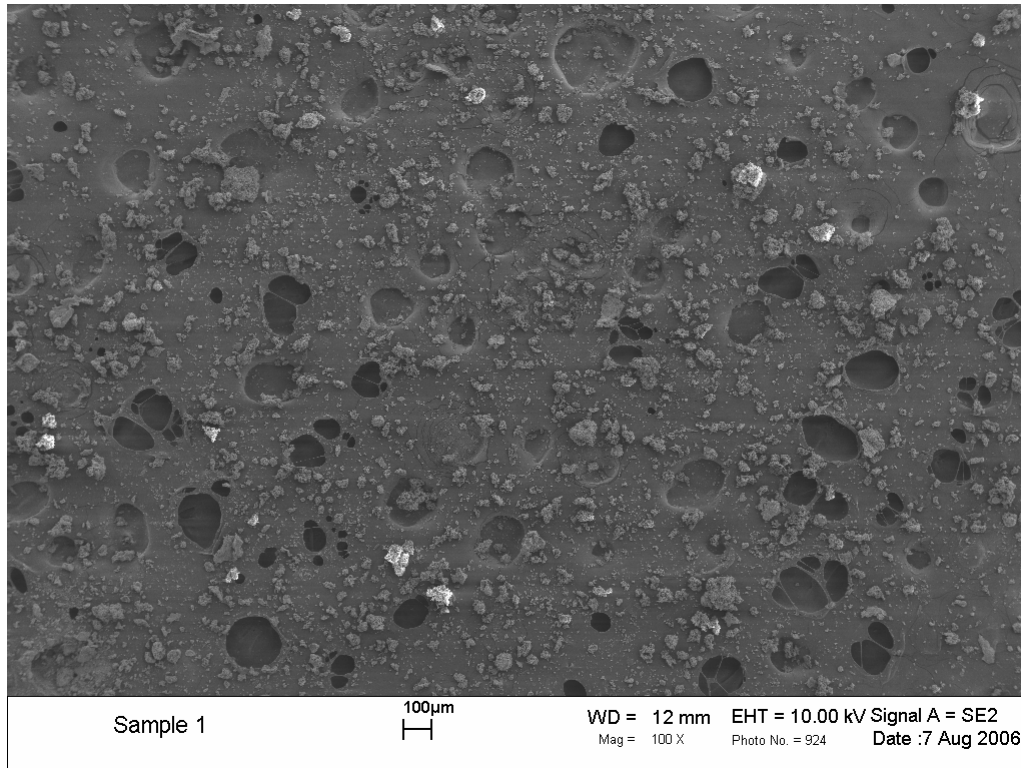


Figure 46: As-reacted MgO/TiB<sub>2</sub> at 100x magnification

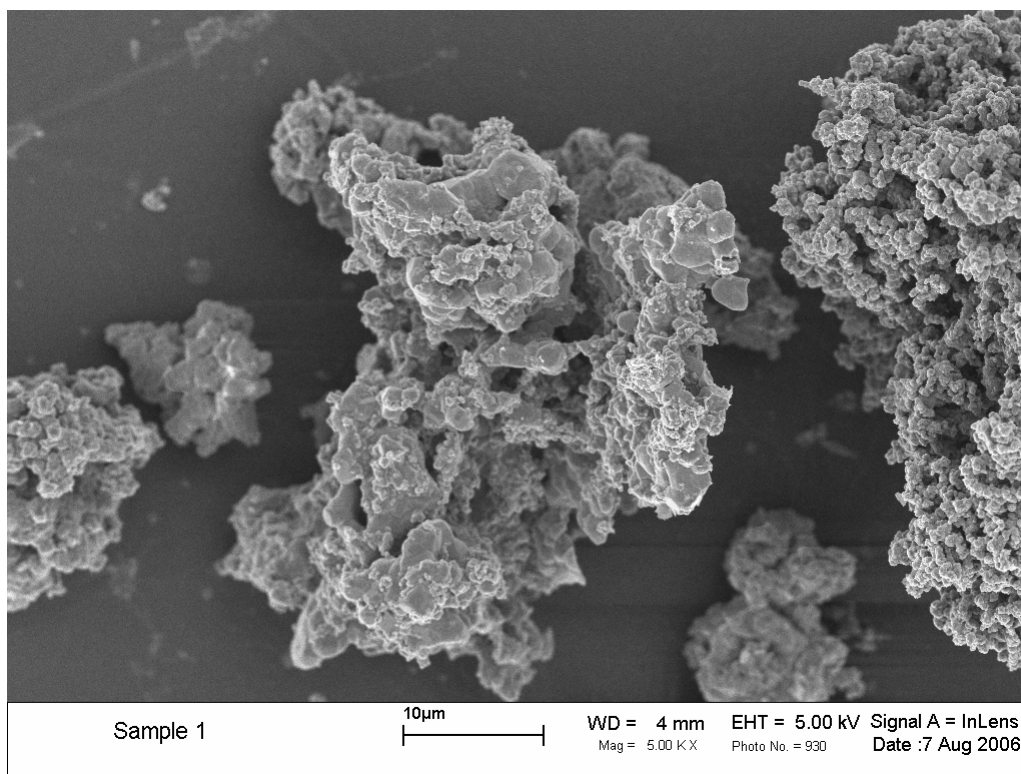


Figure 47: As-reacted MgO/TiB<sub>2</sub> at 5,000x magnification

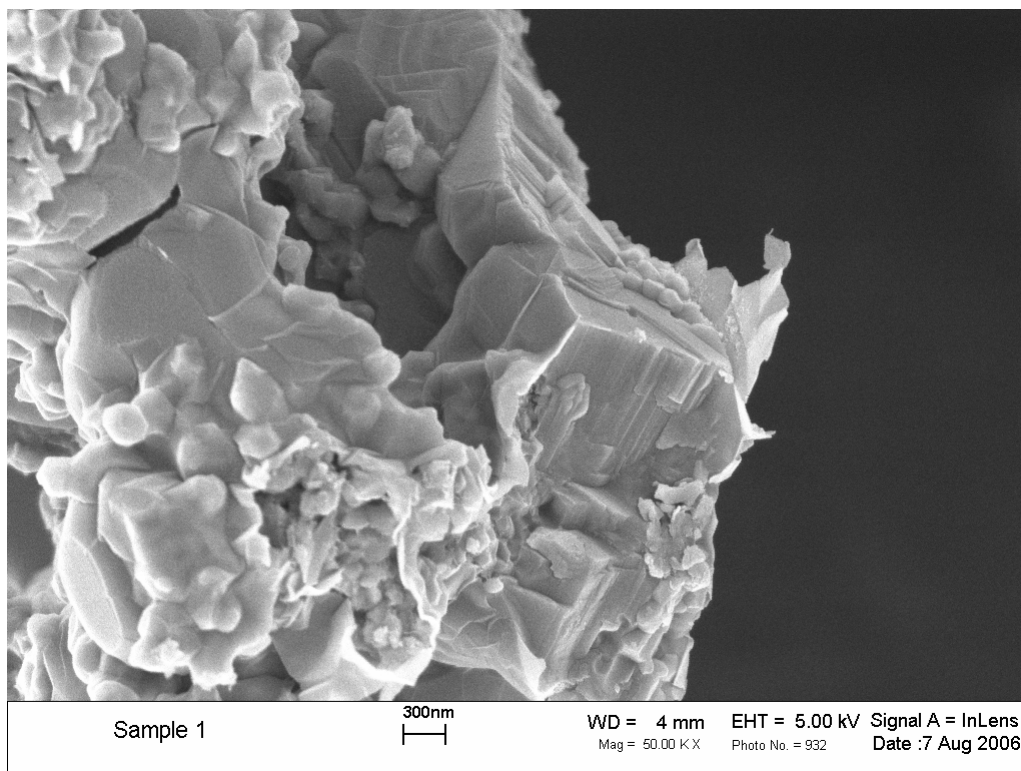


Figure 48: As-reacted MgO/TiB<sub>2</sub> at 50,000x magnification

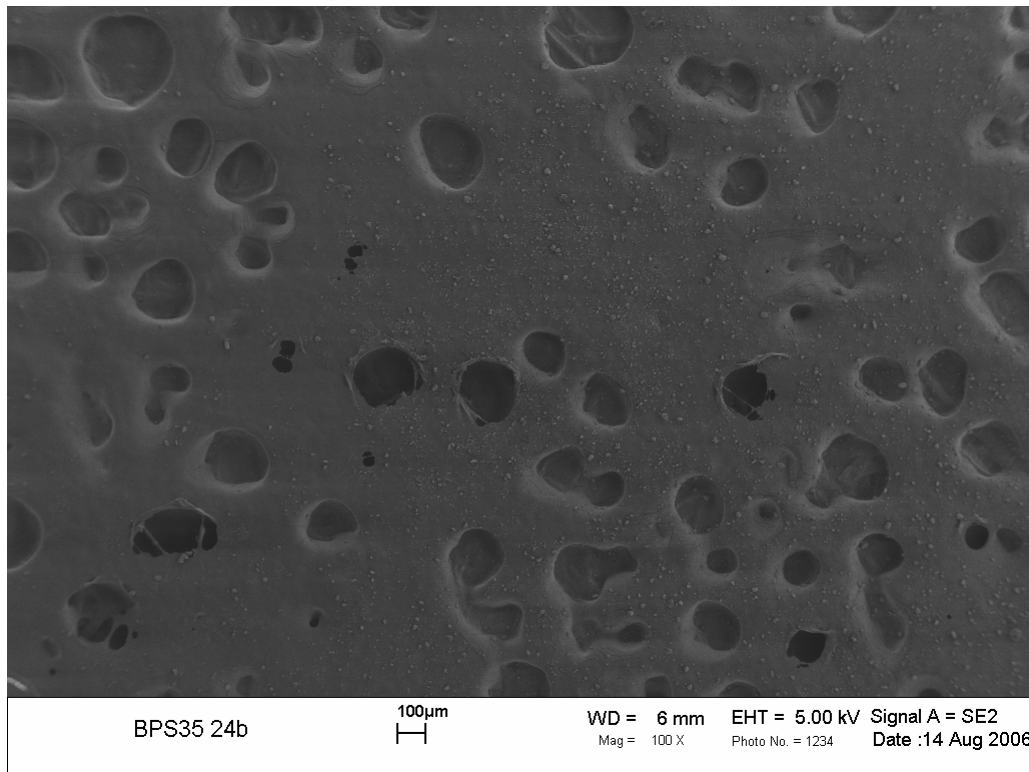


Figure 49: As-reacted MgO/TiB<sub>2</sub> milled for 18 hours at 100x magnification

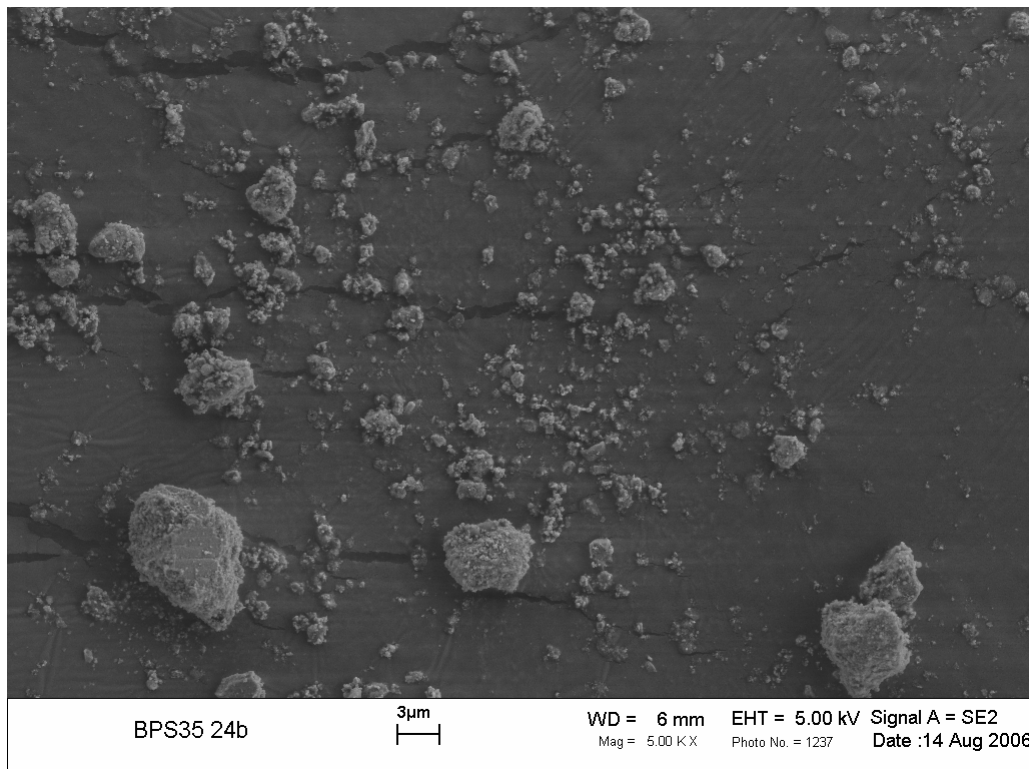


Figure 50: As-reacted MgO/TiB<sub>2</sub> milled for 18 hours at 5,000x magnification

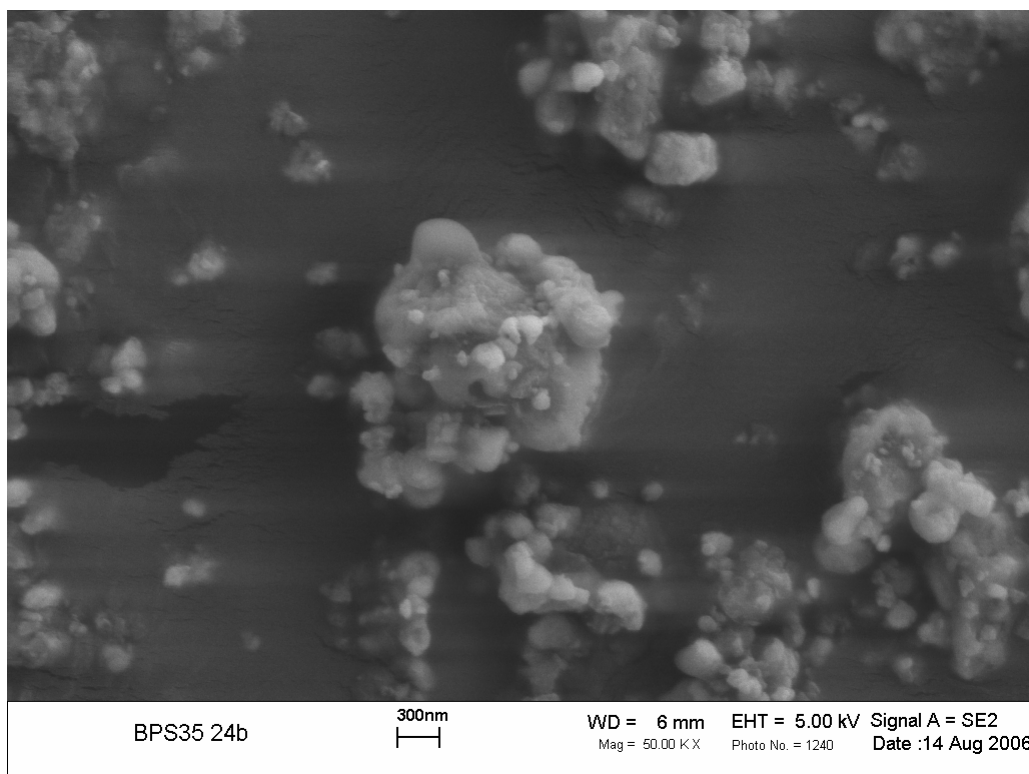


Figure 51: As-reacted MgO/TiB<sub>2</sub> milled for 18 hours at 50,000x magnification

### *A.1.3 Leaching Results*

SEM micrographs of the leached powders are included in this section for leaching performed at 90°C for both SHS produced and commercial powders. The selected micrographs are representative of the respective triplicate set. The leached SHS produced products are presented first at three magnification levels showing the sample overview, individual particles, and surface features. The commercial powders are presented in the following set, showing the sample overview and individual particles.

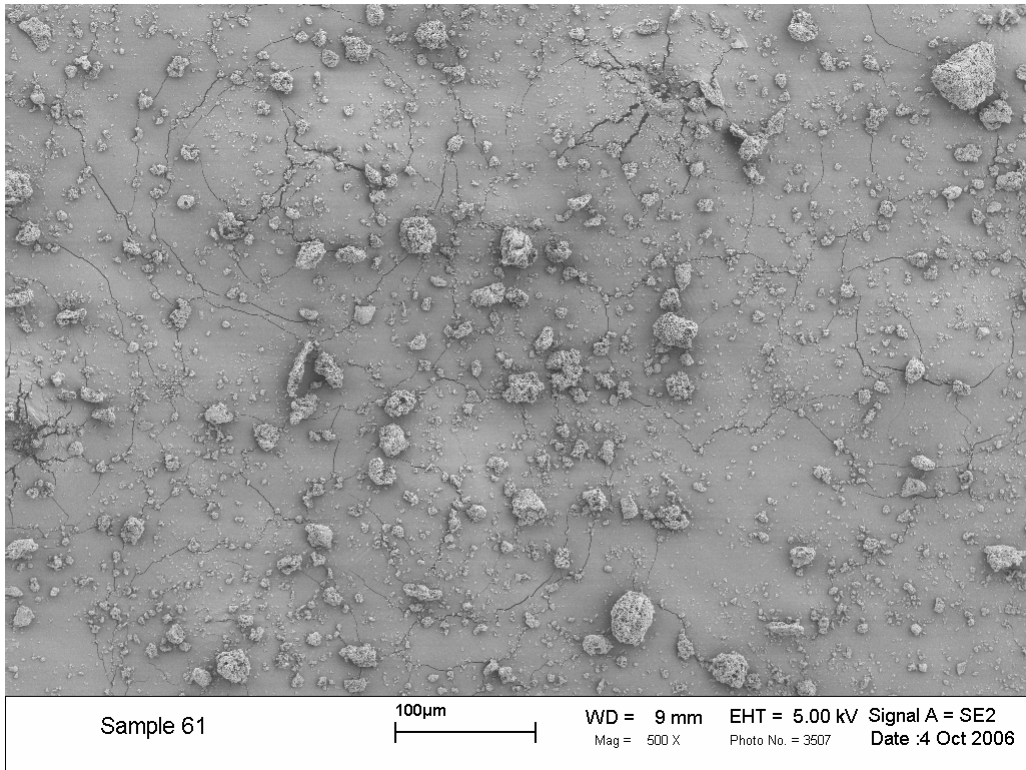


Figure 52: SHS MgO/TiB<sub>2</sub> – min pH 4.0 at 90°C at 500x magnification

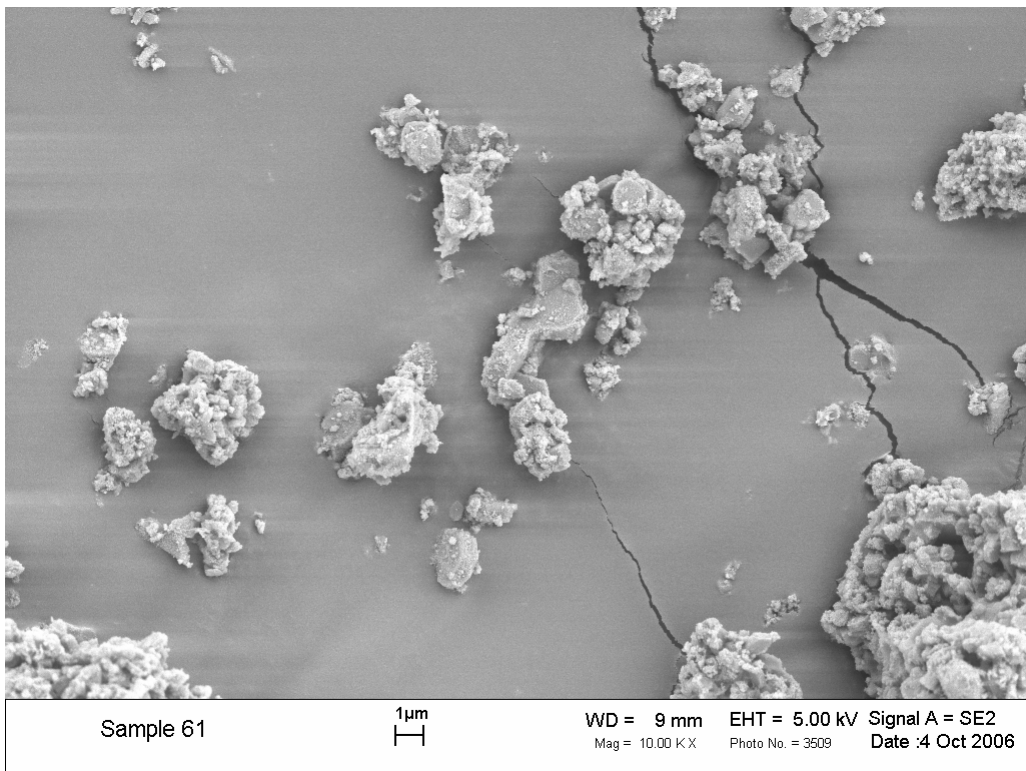


Figure 53: SHS MgO/TiB<sub>2</sub> – min pH 4.0 at 90°C at 10,000x magnification

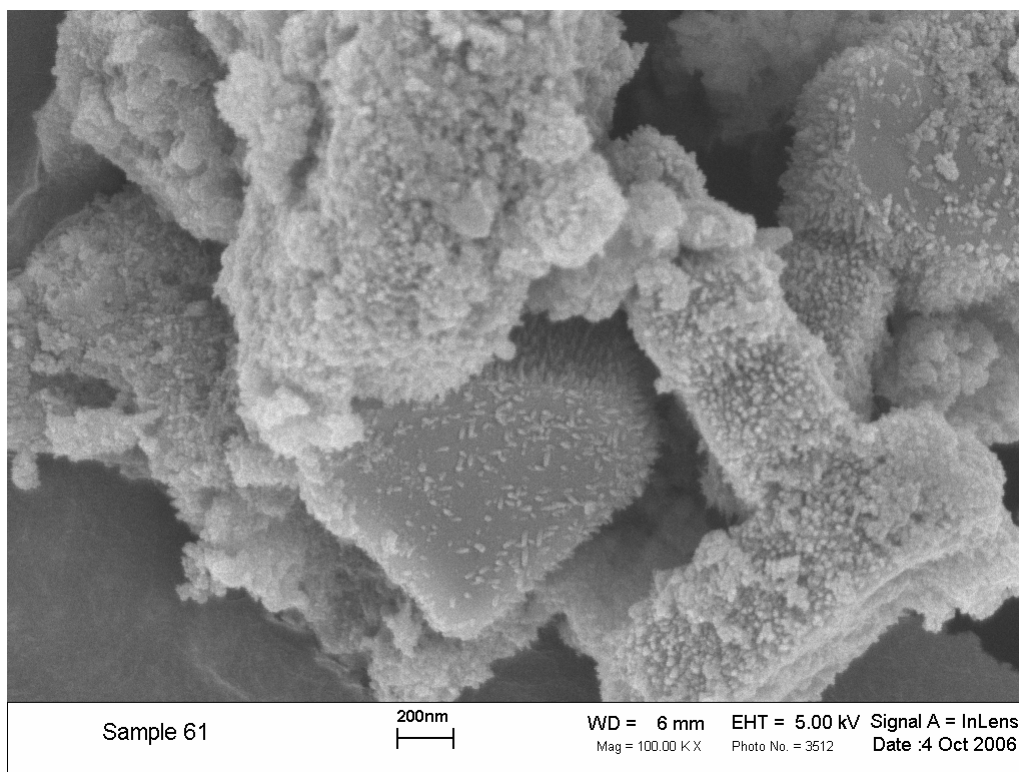


Figure 54: SHS MgO/TiB<sub>2</sub> – min pH 4.0 at 90°C at 100,00 0x magnification

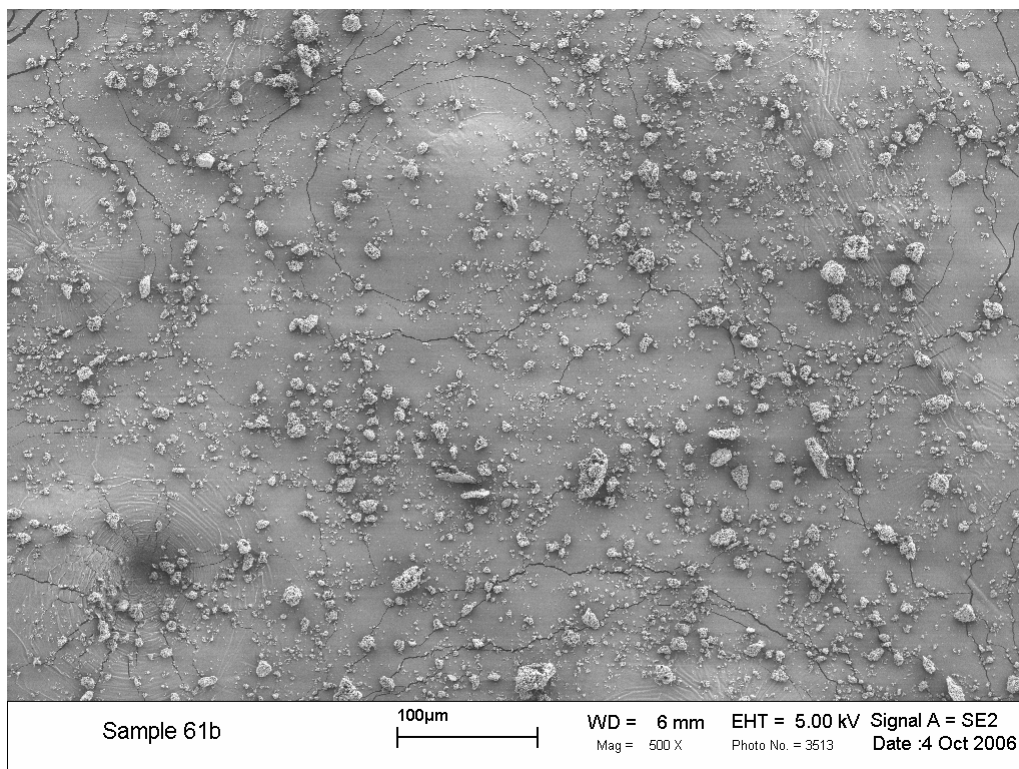


Figure 55: SHS MgO/TiB<sub>2</sub> – min pH 4.0 at 90°C at 500x magnification – 2<sup>nd</sup> Cycle

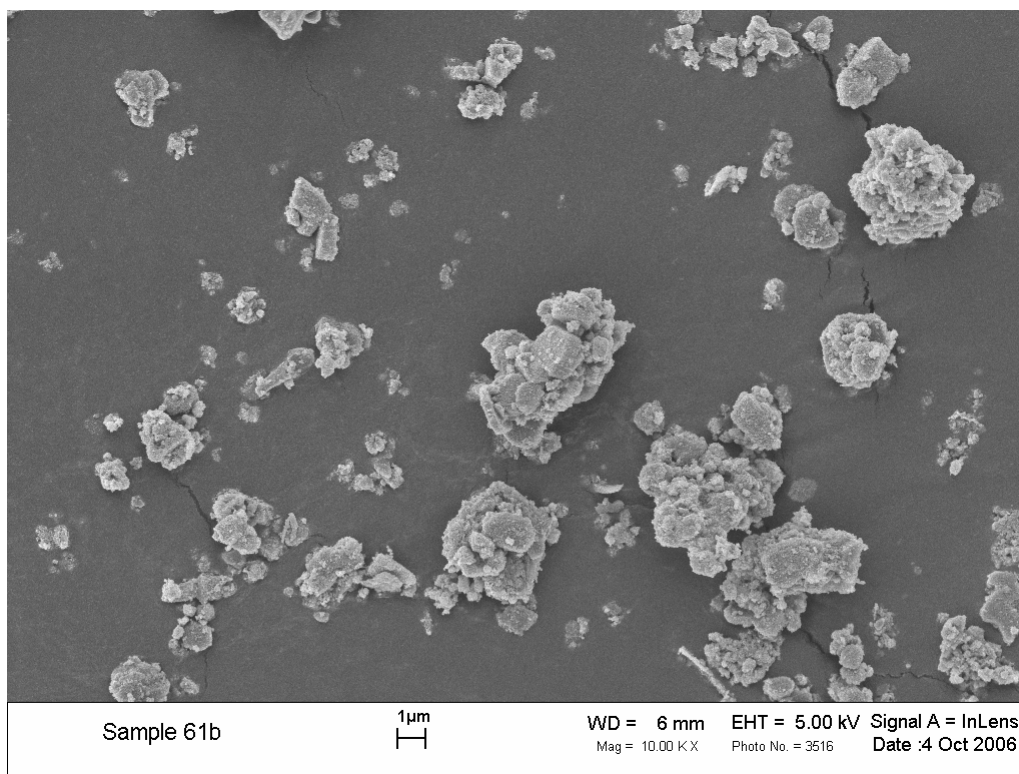


Figure 56: SHS MgO/TiB<sub>2</sub> – min pH 4.0 at 90°C at 10,000x magnification – 2<sup>nd</sup> Cycle

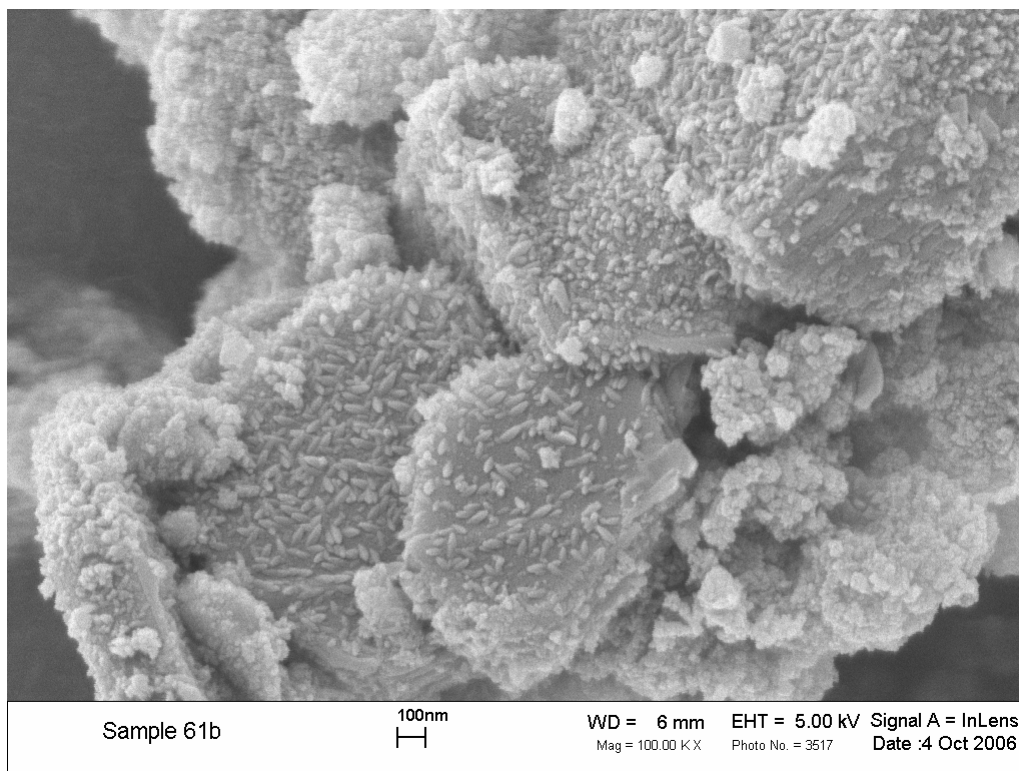


Figure 57: SHS MgO/TiB<sub>2</sub> – min pH 4.0 at 90°C at 100,000x magnification – 2<sup>nd</sup> Cycle

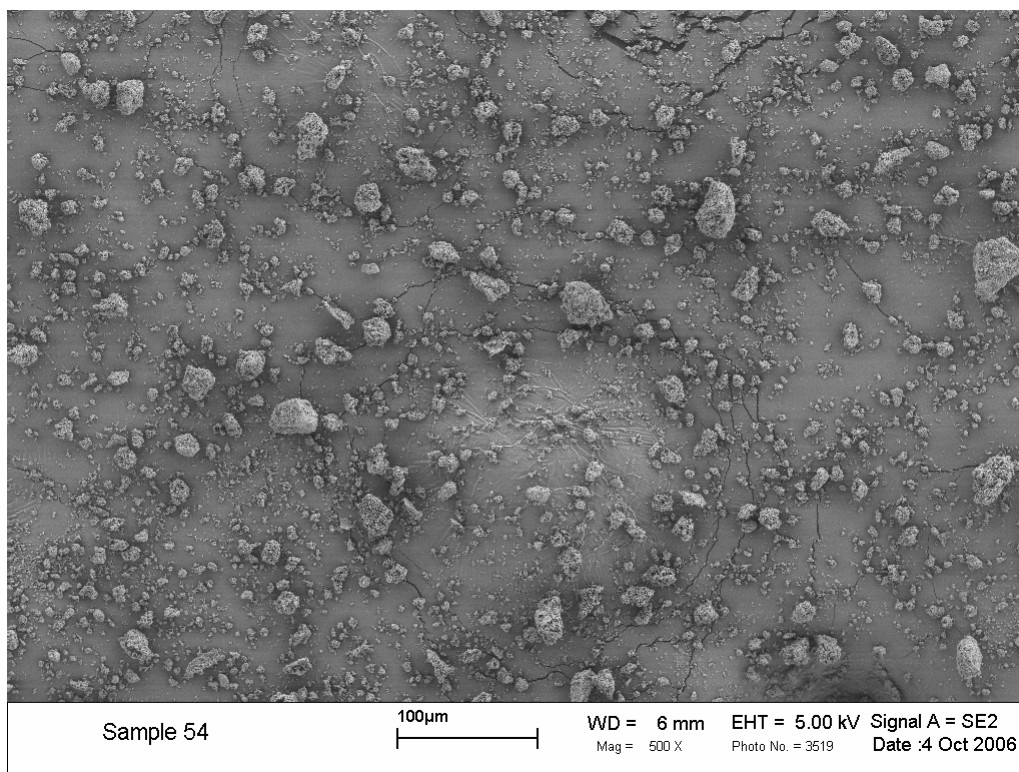


Figure 58: SHS MgO/TiB<sub>2</sub> – min pH 2.5 at 90°C at 500x magnification

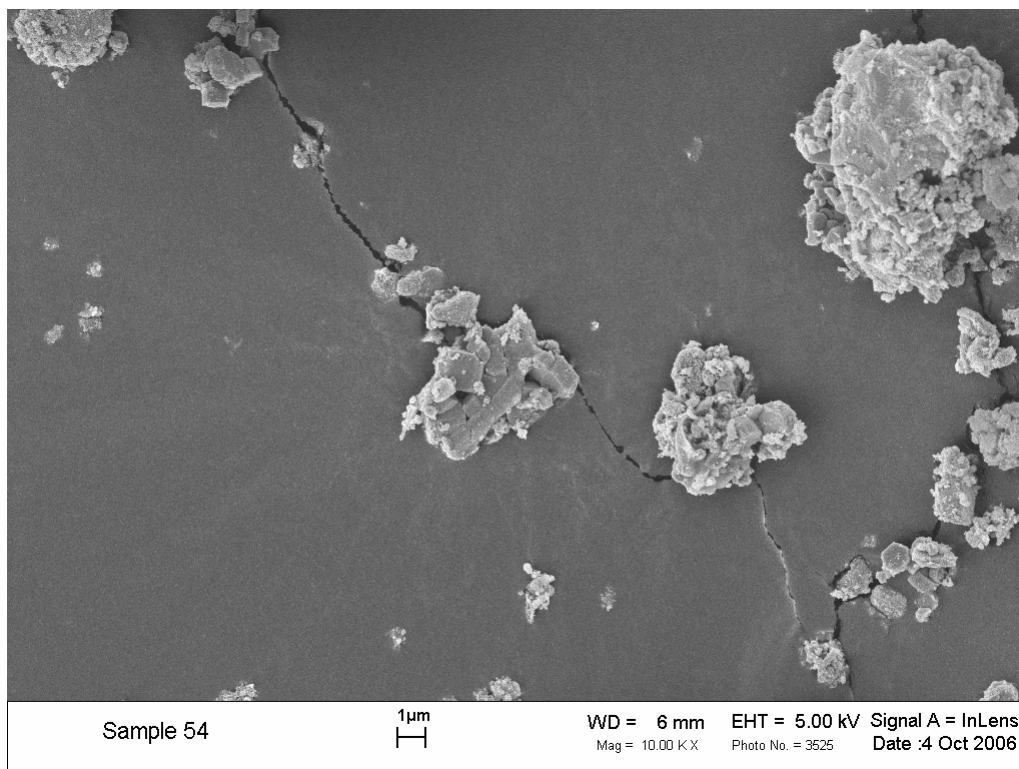


Figure 59: SHS MgO/TiB<sub>2</sub> – min pH 2.5 at 90°C at 10,000 magnification

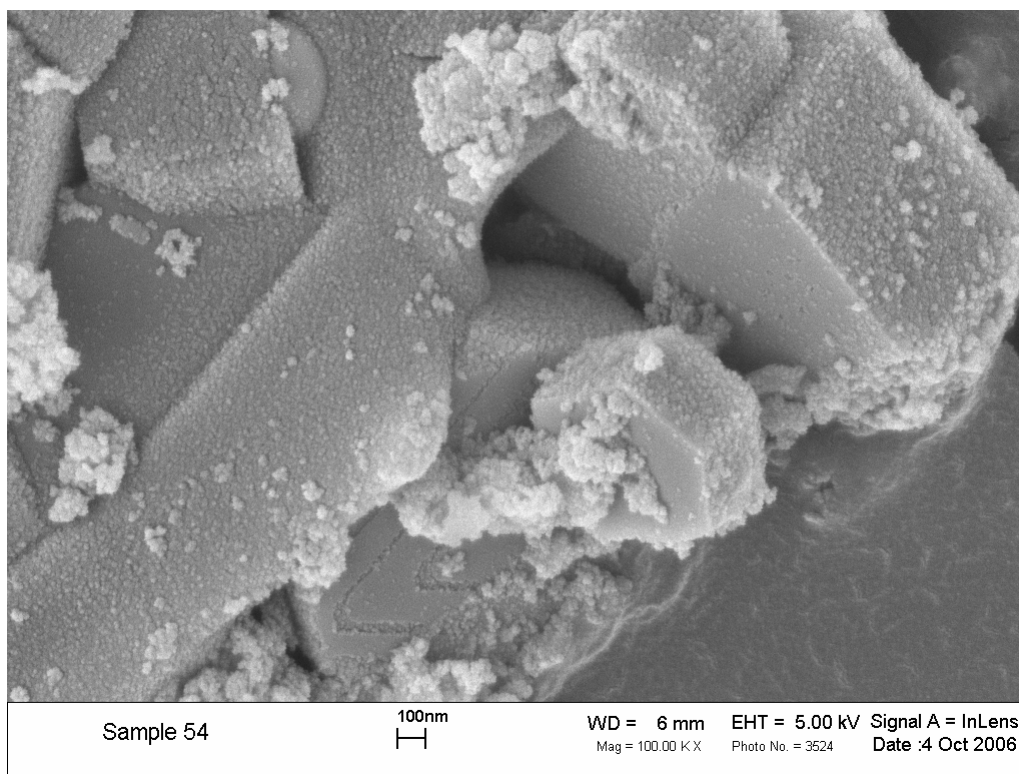


Figure 60: SHS MgO/TiB<sub>2</sub> – min pH 2.5 at 90°C at 100,000x magnification

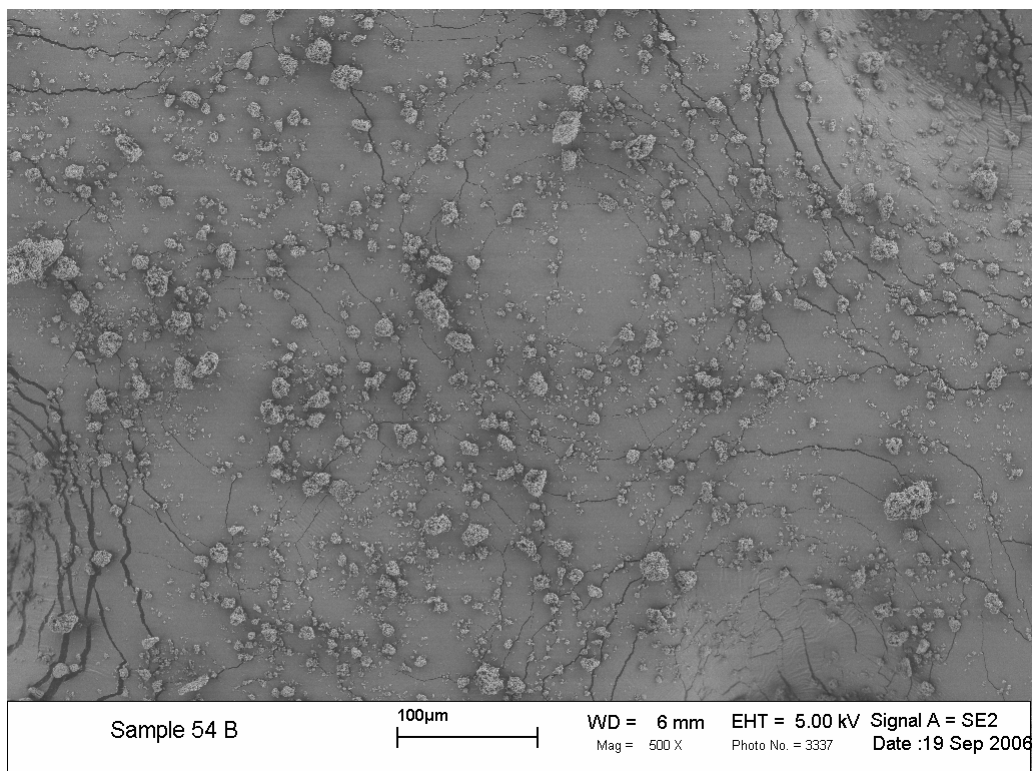


Figure 61: SHS MgO/TiB<sub>2</sub> – min pH 2.5 at 90°C at 500x magnification – 2<sup>nd</sup> Cycle

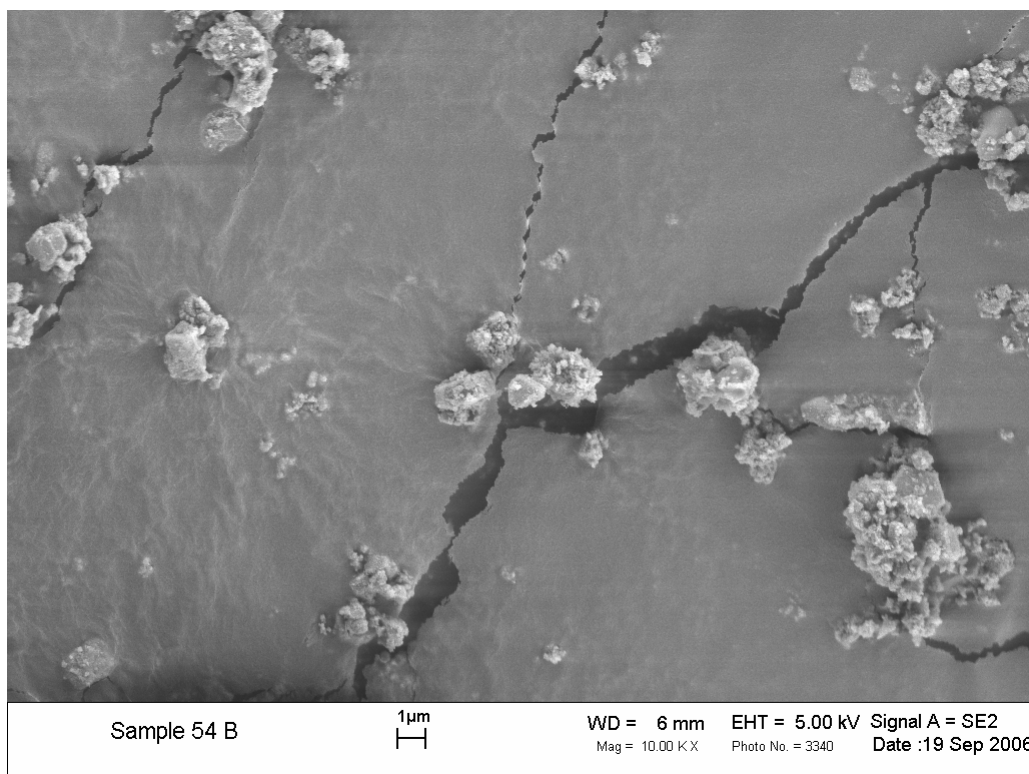


Figure 62: SHS MgO/TiB<sub>2</sub> – min pH 2.5 at 90°C - 10,000x magnification – 2<sup>nd</sup> Cycle

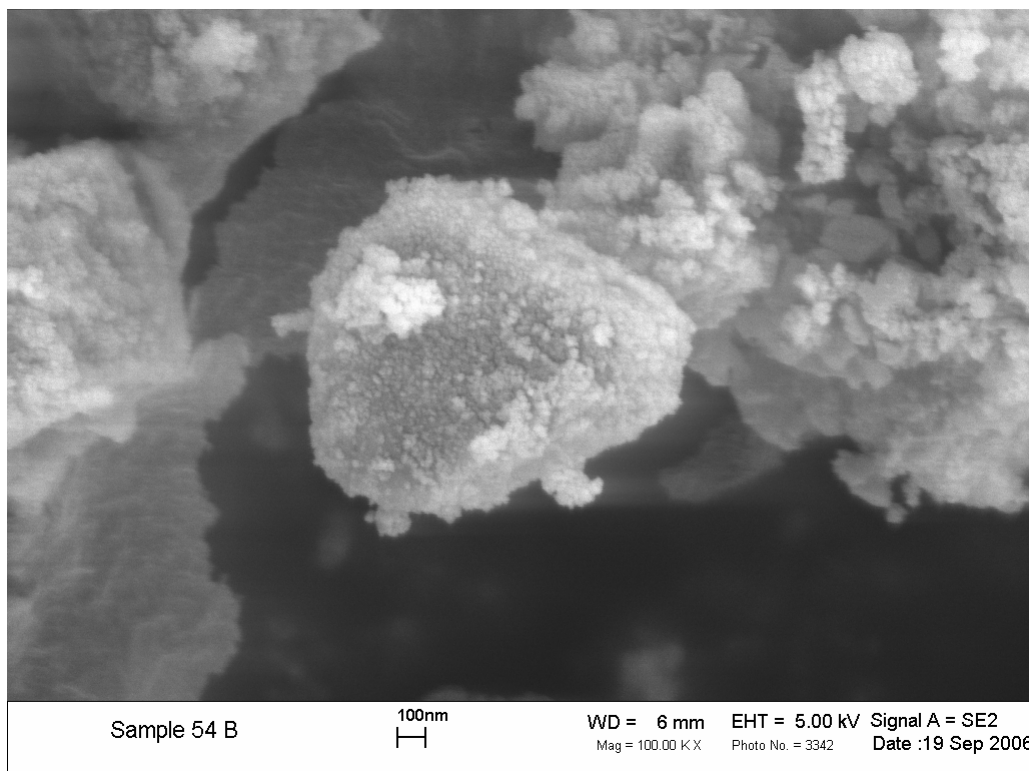


Figure 63: SHS MgO/TiB<sub>2</sub> – min pH 2.5 at 90°C - 100,000x magnification – 2<sup>nd</sup> Cycle

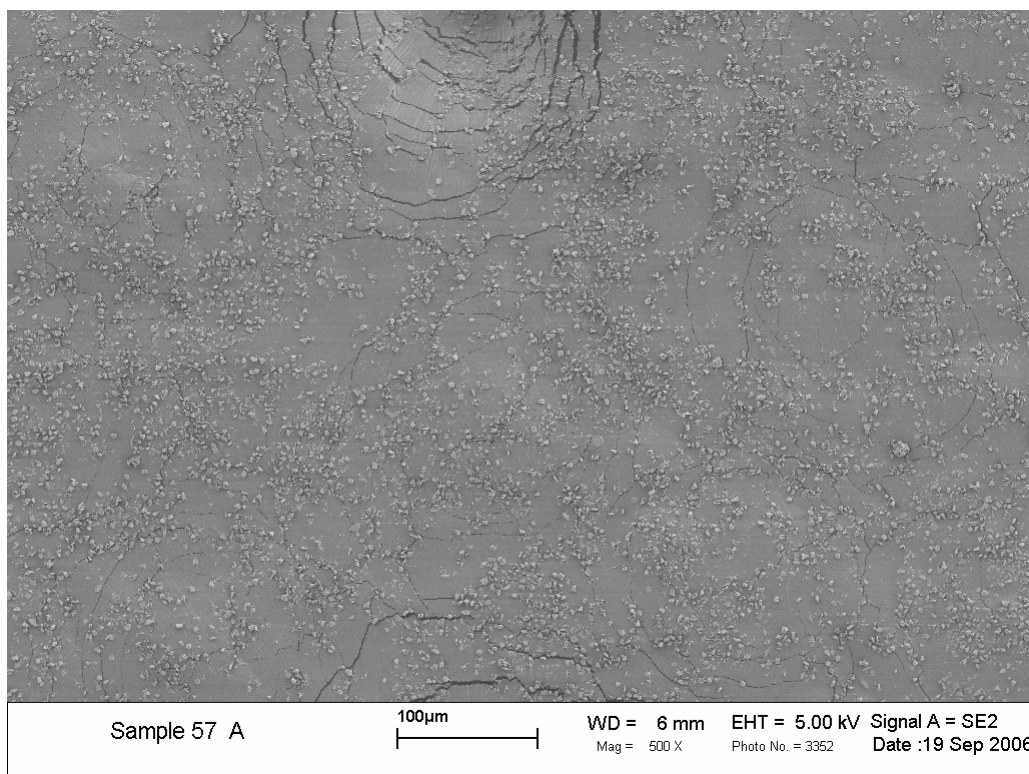


Figure 64: SHS MgO/TiB<sub>2</sub> – min pH 1.0 at 90°C - 500x magnification

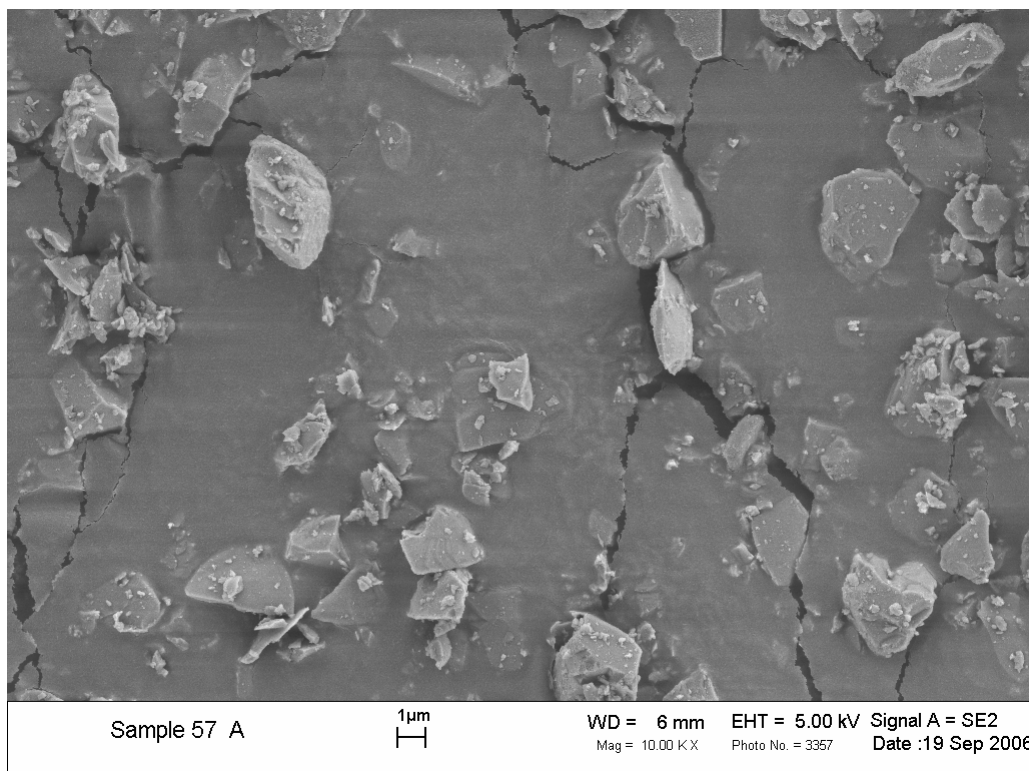


Figure 65: SHS MgO/TiB<sub>2</sub> – min pH 1.0 at 90°C – 10,000x magnification

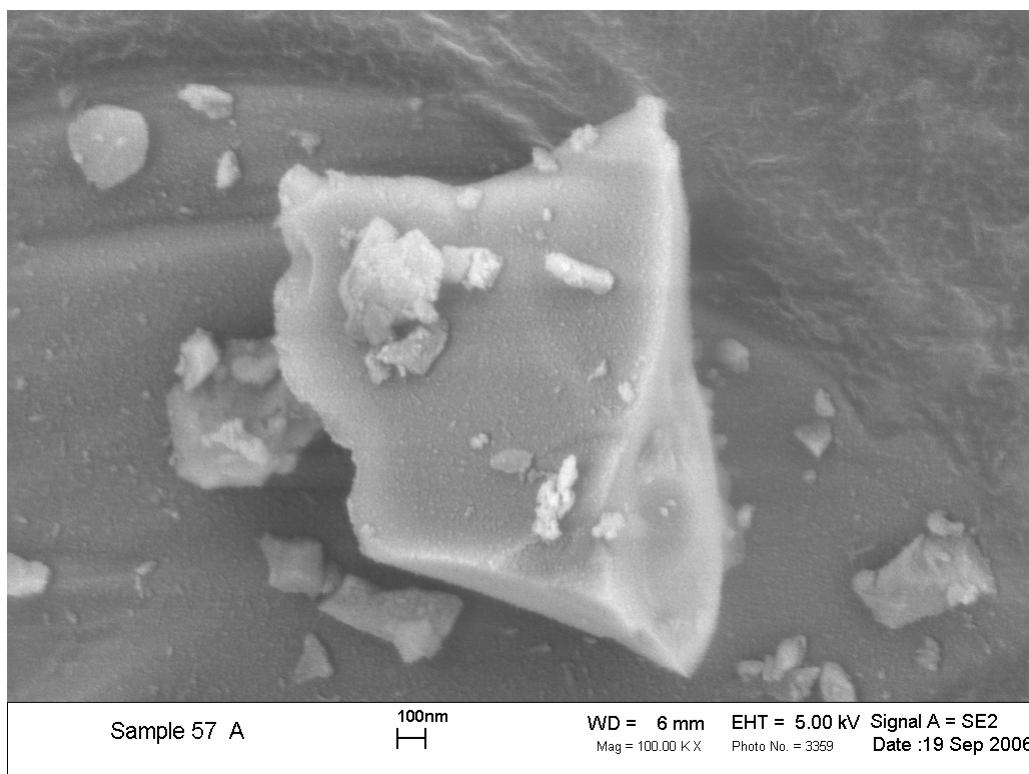


Figure 66: SHS MgO/TiB<sub>2</sub> – min pH 1.0 at 90°C – 100,000x magnification

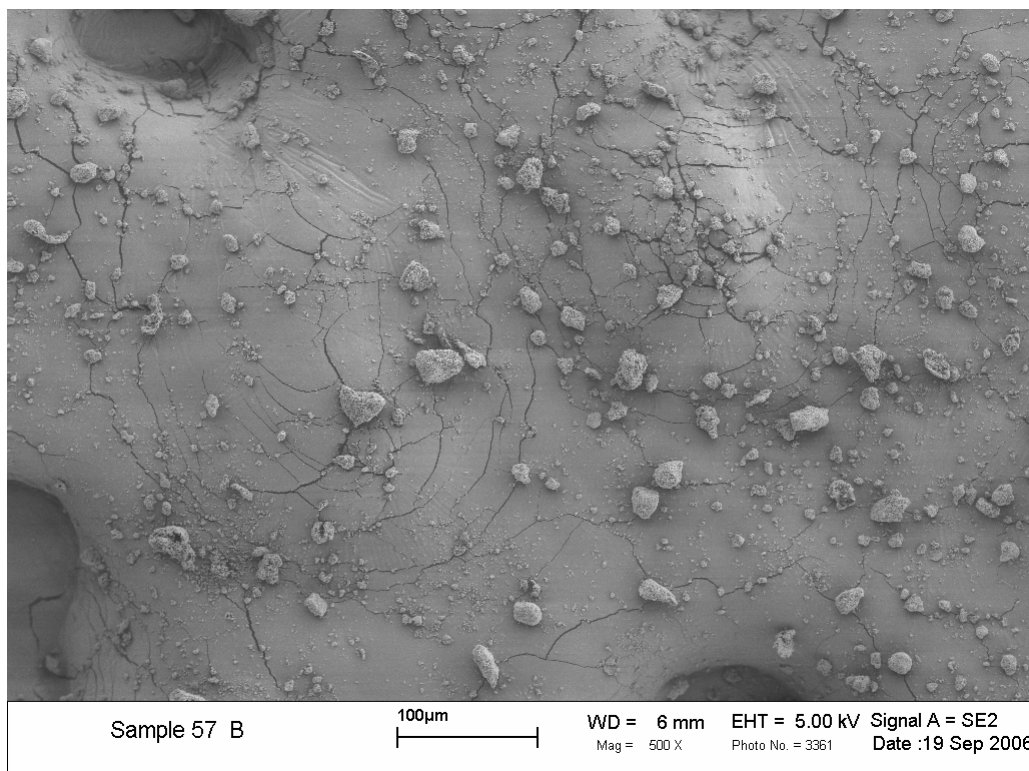


Figure 67: SHS MgO/TiB<sub>2</sub> – min pH 1.0 at 90°C - 500x magnification – 2<sup>nd</sup> Cycle

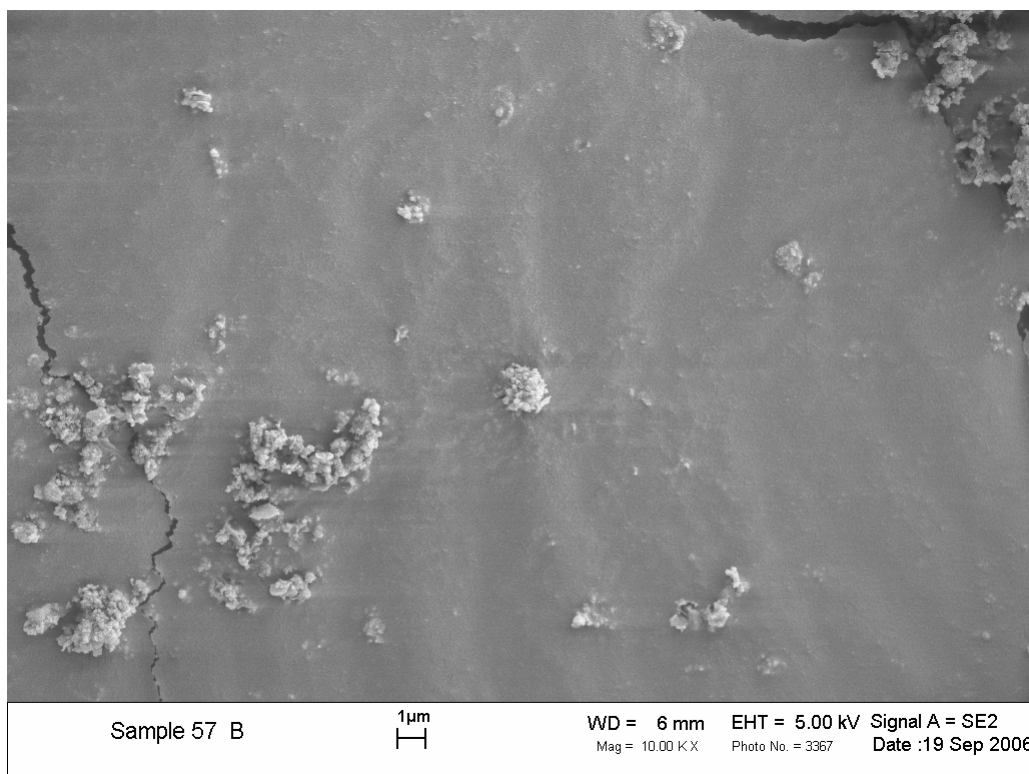


Figure 68: SHS MgO/TiB<sub>2</sub> – min pH 1.0 at 90°C – 10,000x magnification – 2<sup>nd</sup> Cycle

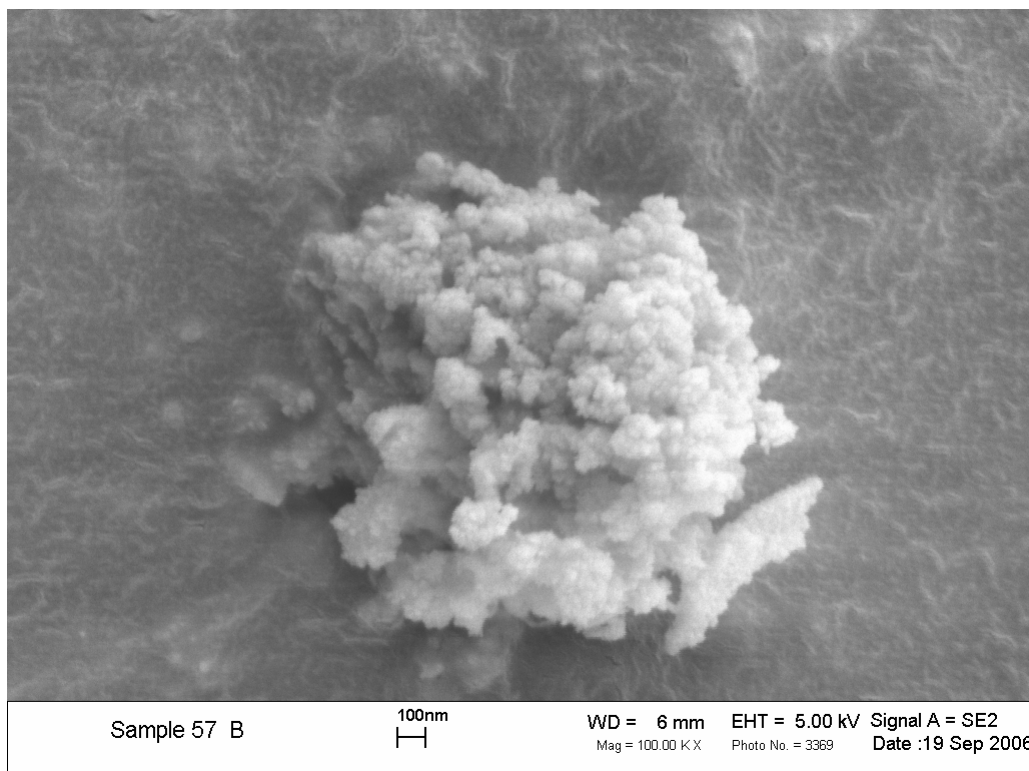


Figure 69: SHS MgO/TiB<sub>2</sub> – min pH 1.0 at 90°C – 100,000x magnification – 2<sup>nd</sup> Cycle

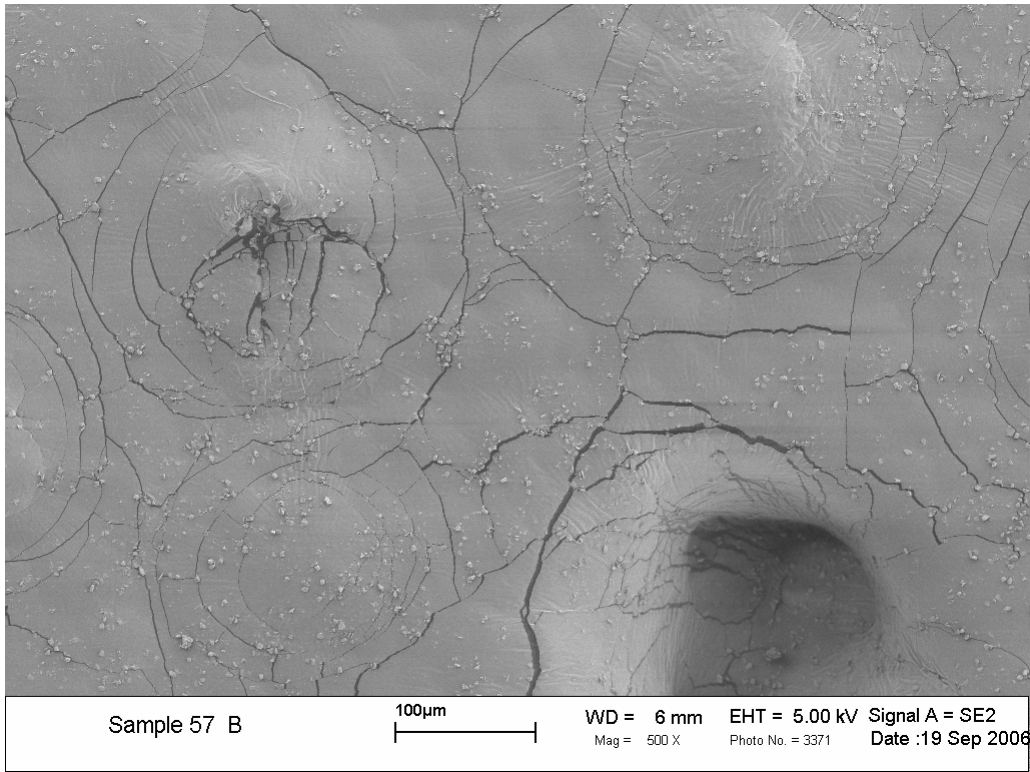


Figure 70: Commercial Powders – min pH 4.0 at 90°C - 500x magnification

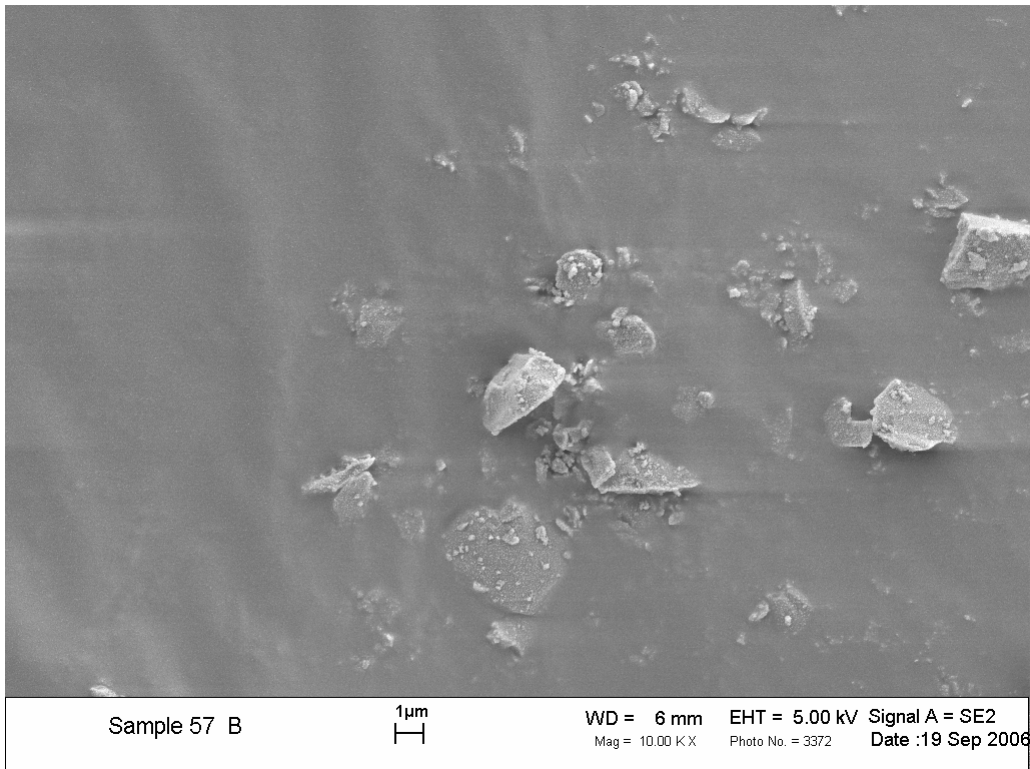


Figure 71: Commercial Powders – min pH 4.0 at 90°C – 10,000x magnification

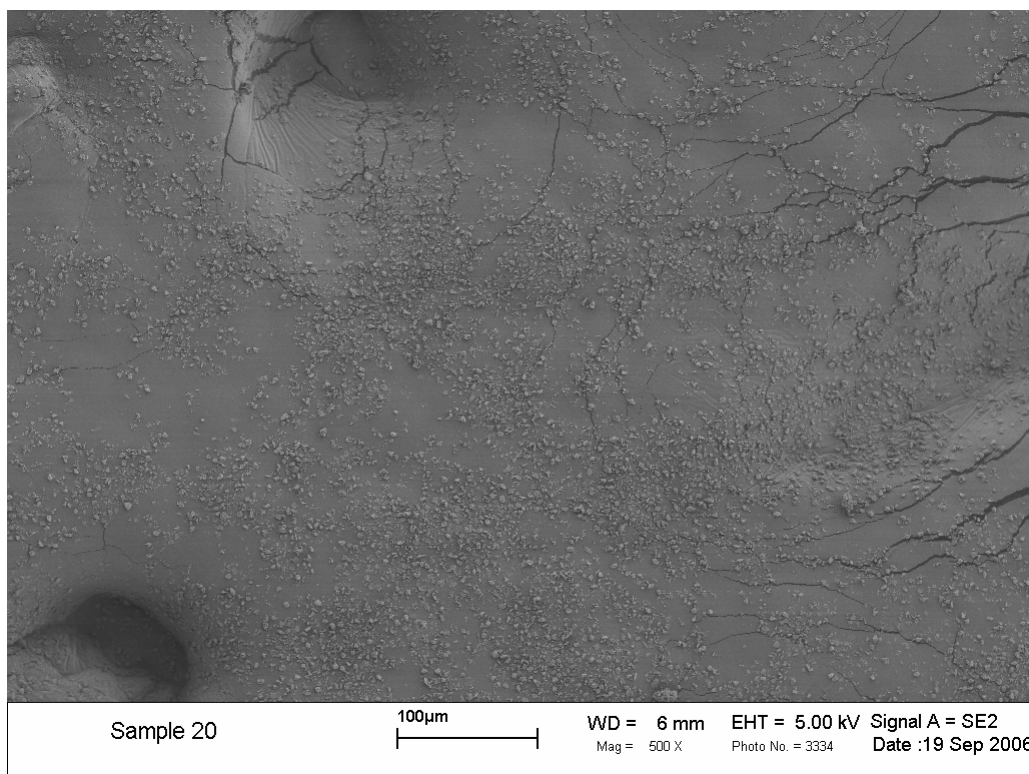


Figure 72: Commercial Powders – min pH 2.5 at 90°C – 500x magnification

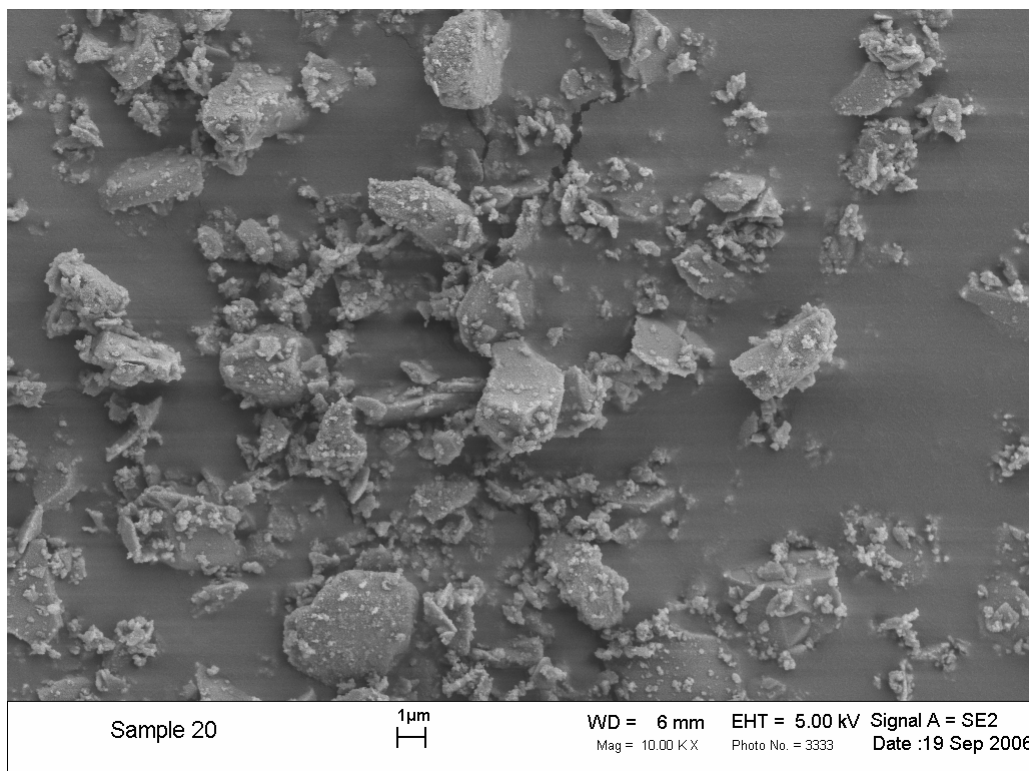


Figure 73: Commercial Powders – min pH 2.5 at 90°C – 10,000x magnification

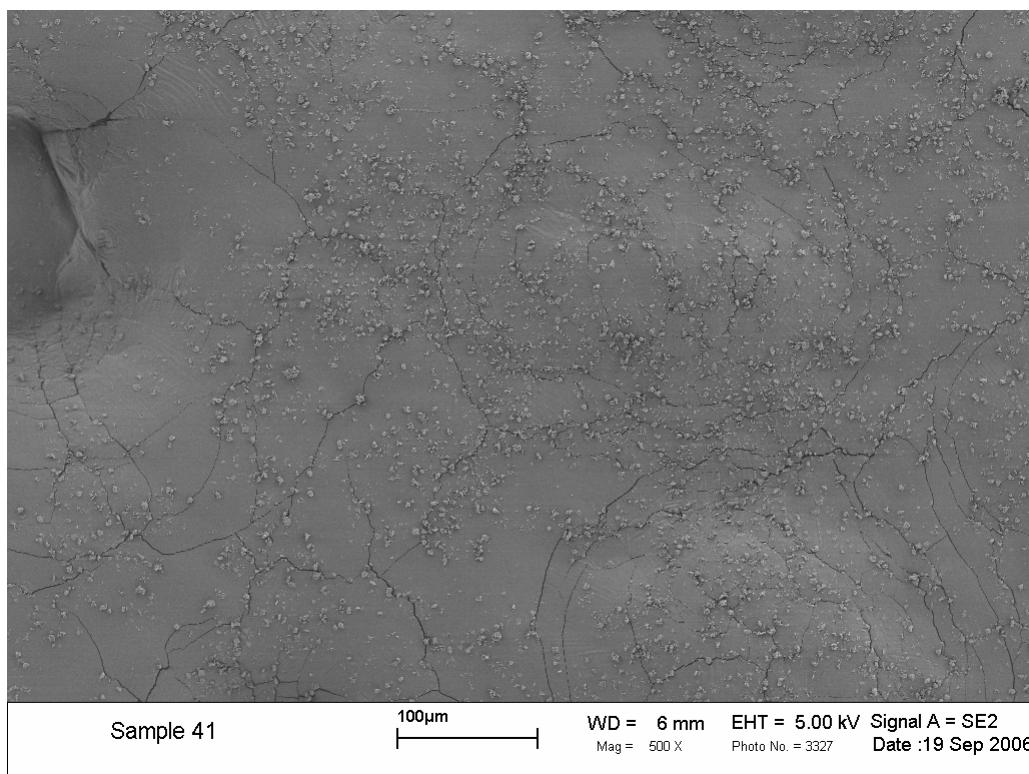


Figure 74: Commercial Powders – min pH 1.0 at 90°C – 500x magnification

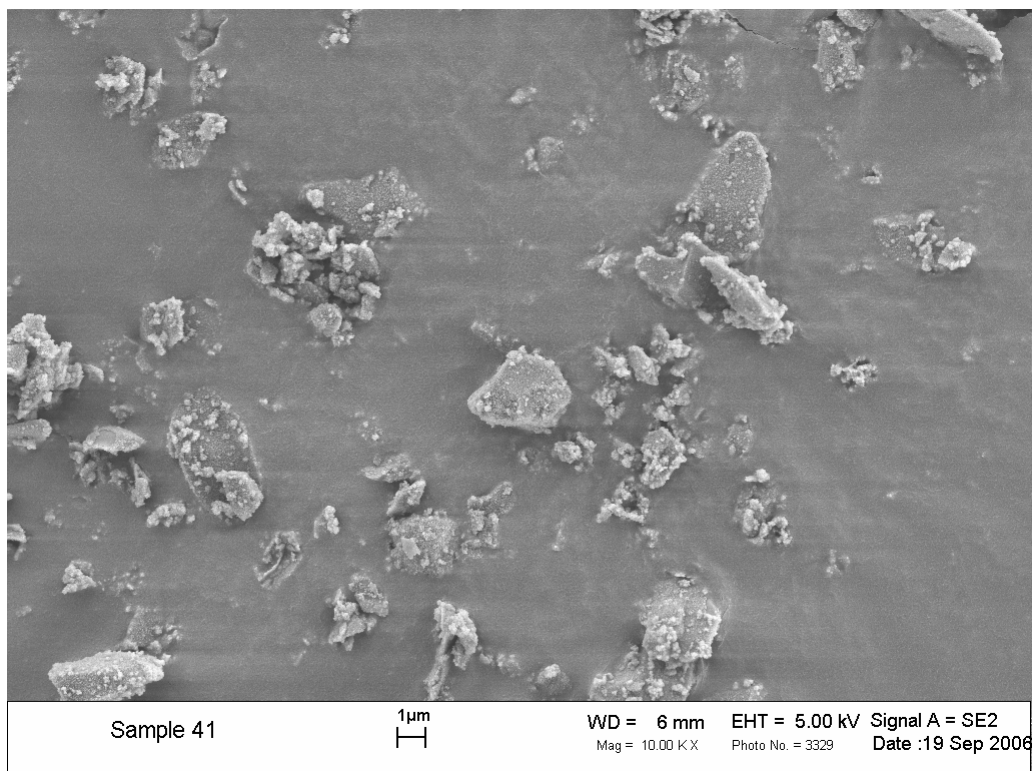


Figure 75: Commercial Powders – min pH 1.0 at 90°C – 10,000x magnification

## A.2 Particle Size Analysis

Particle size analysis was run on a Horiba LA-950 Laser Light Scattering particle size analyzer. Analysis for Mg-flake was reproduced from certificate of analysis form Reade Manufacturing.

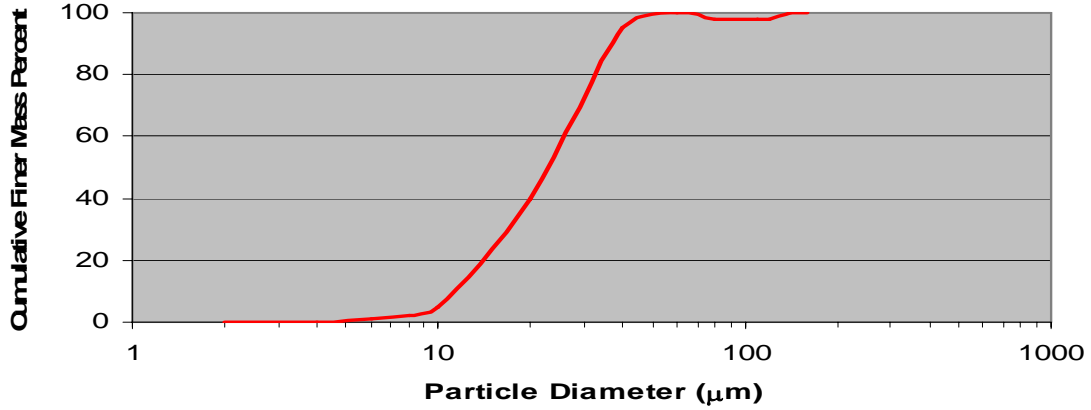


Figure 76: Mg flake particle size distribution from certificate of analysis

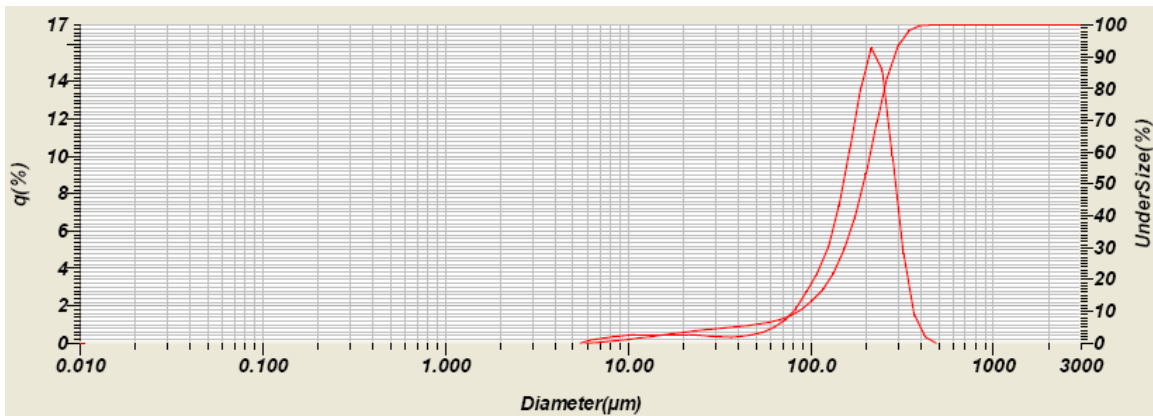


Figure 77: Amorphous B<sub>2</sub>O<sub>3</sub> particle size distribution

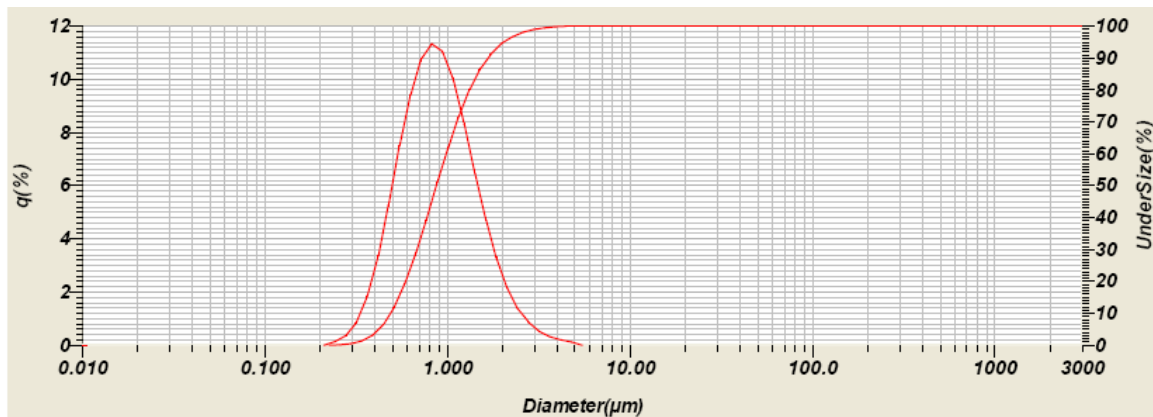


Figure 78: Pigment grade TiO<sub>2</sub> particle size distribution

### A.3 XRD

Powder x-ray diffraction analysis was done on a Siemens D5000 Diffractometer running Diffrac<sup>Plus</sup> EVA software (v 7.0.0.1). Dried powders were mounted on the stage using methanol to avoid preferred orientation. A standard Cu-K $\alpha$  diffraction pattern was produced scanning from 18°-104° (2 theta), with a step size of 0.01° at 2 s per step.

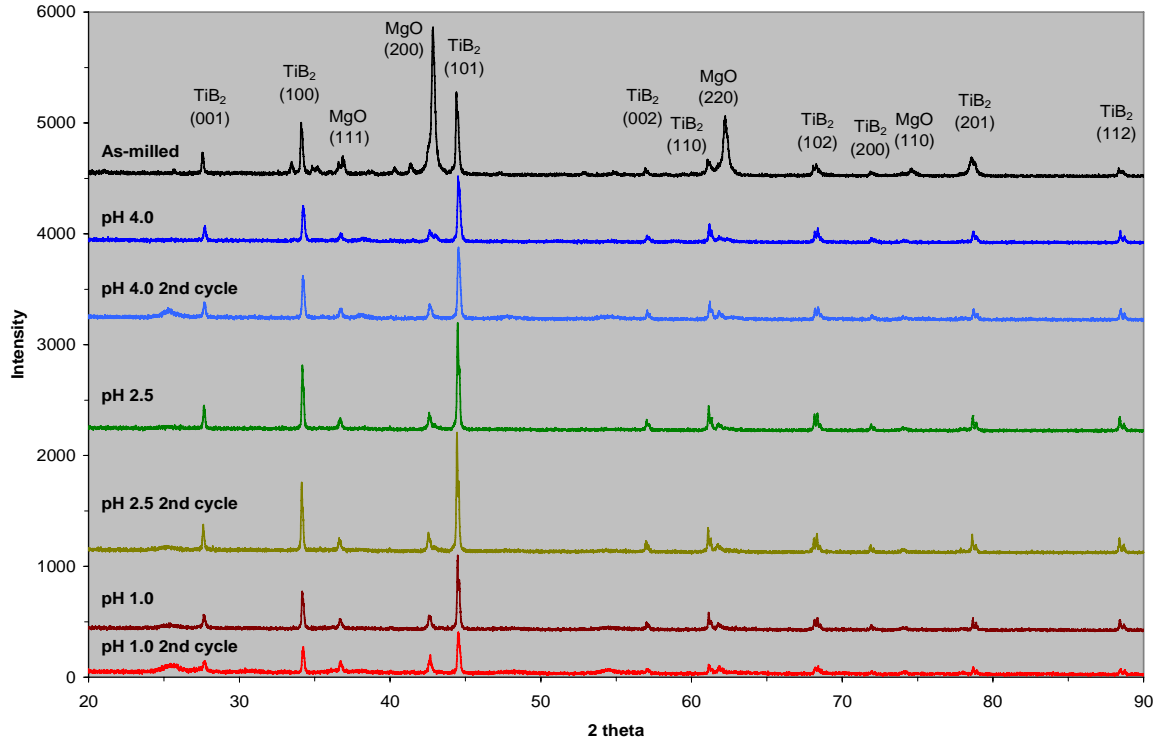


Figure 79: Summary of all scans with respect to diffraction scan of as-reacted SHS product

#### A.4 pH Strip Charts

The following strip charts are selected runs of pH and temperature versus time as recorded from the Accumet™ AB15+ recorder using Fisher Scientific CyberComm Pro 2.3.1 data acquisition software. They are representative of the respective triplicate set.

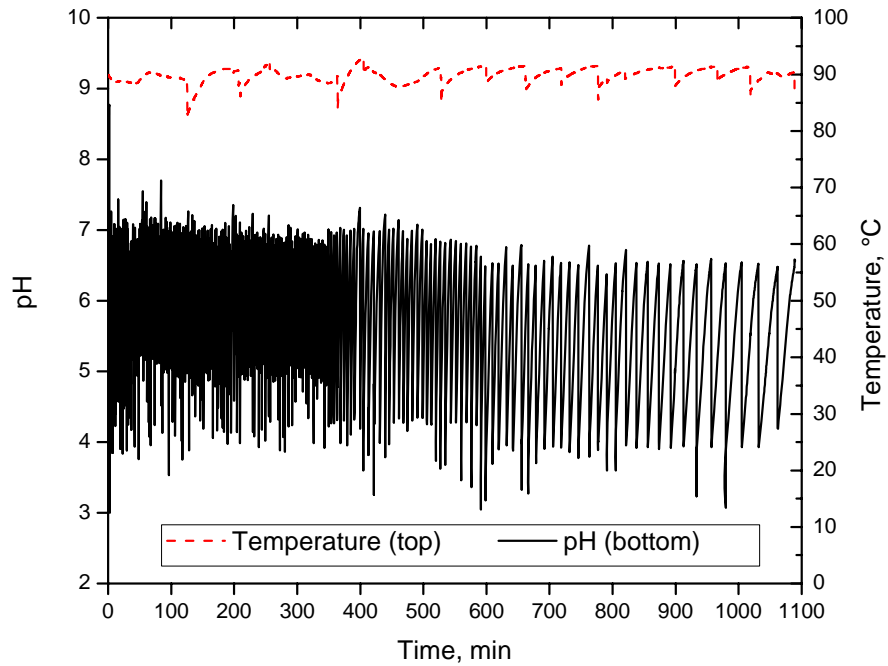


Figure 80: SHS MgO/TiB<sub>2</sub> leaching strip chart for minimum pH 4.0 at 90°C

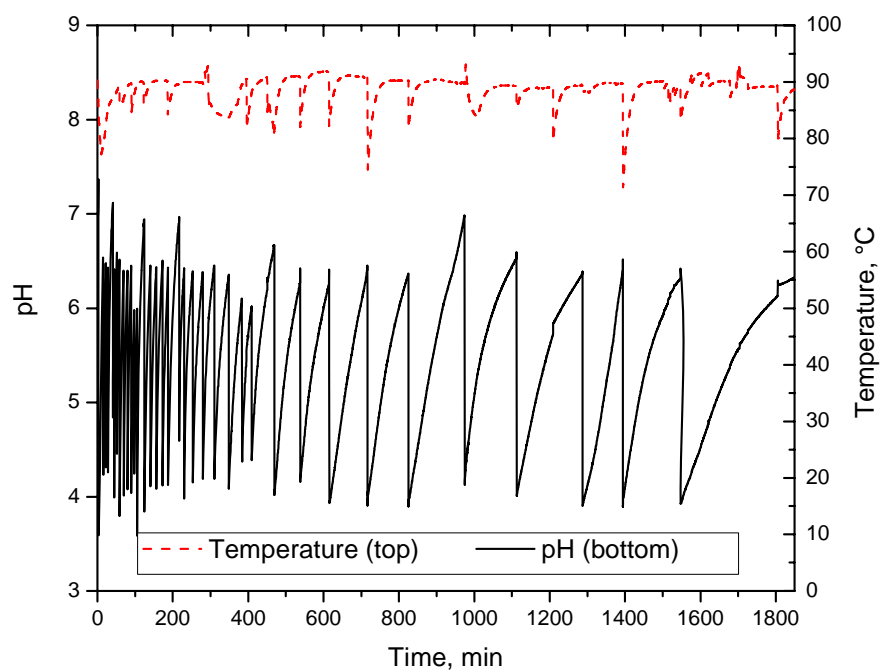


Figure 81: SHS MgO/TiB<sub>2</sub> leaching strip chart for minimum pH 4.0 at 90°C – 2<sup>nd</sup> Cycle

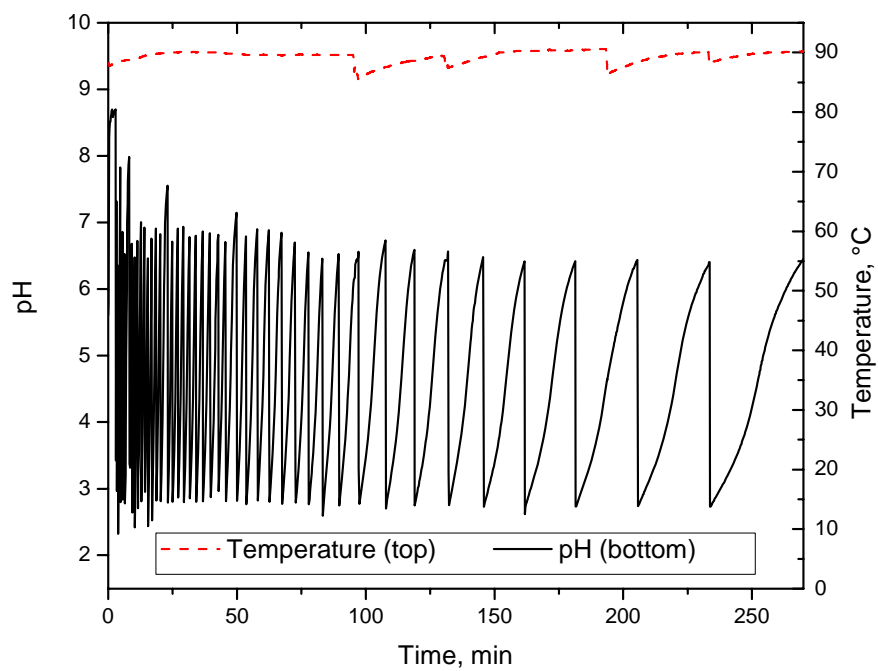


Figure 82: SHS MgO/TiB<sub>2</sub> leaching strip chart for minimum pH 2.5 at 90°C

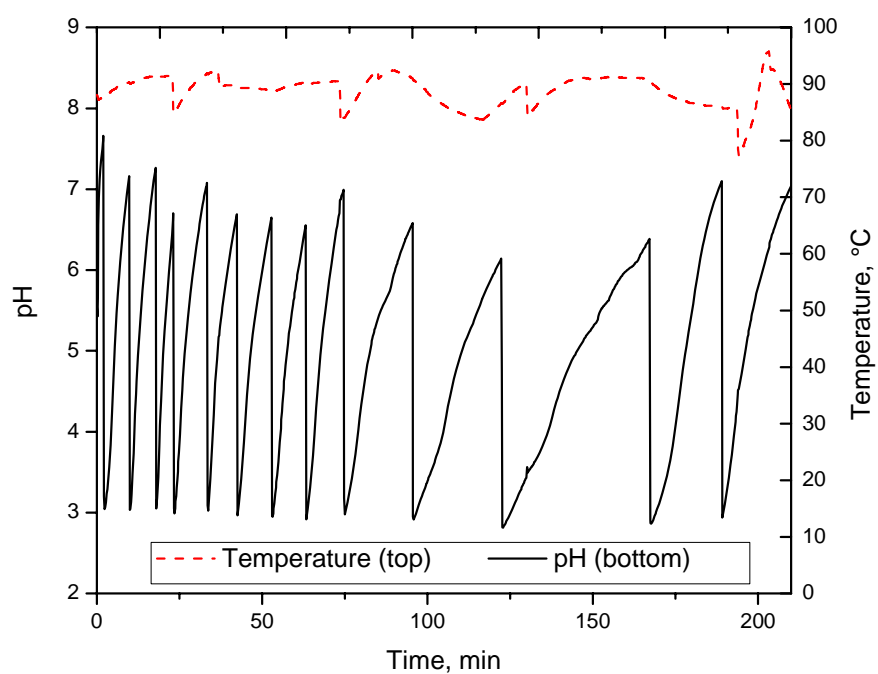


Figure 83: SHS MgO/TiB<sub>2</sub> leaching strip chart for minimum pH 2.5 at 90°C – 2<sup>nd</sup> Cycle

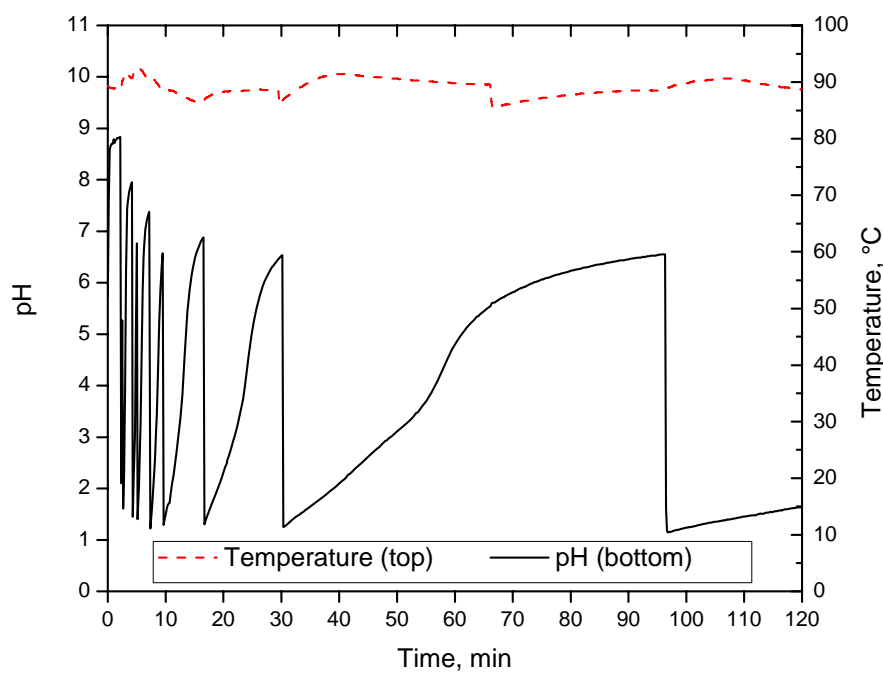


Figure 84: SHS MgO/TiB<sub>2</sub> leaching strip chart for minimum pH 1.0 at 90°C

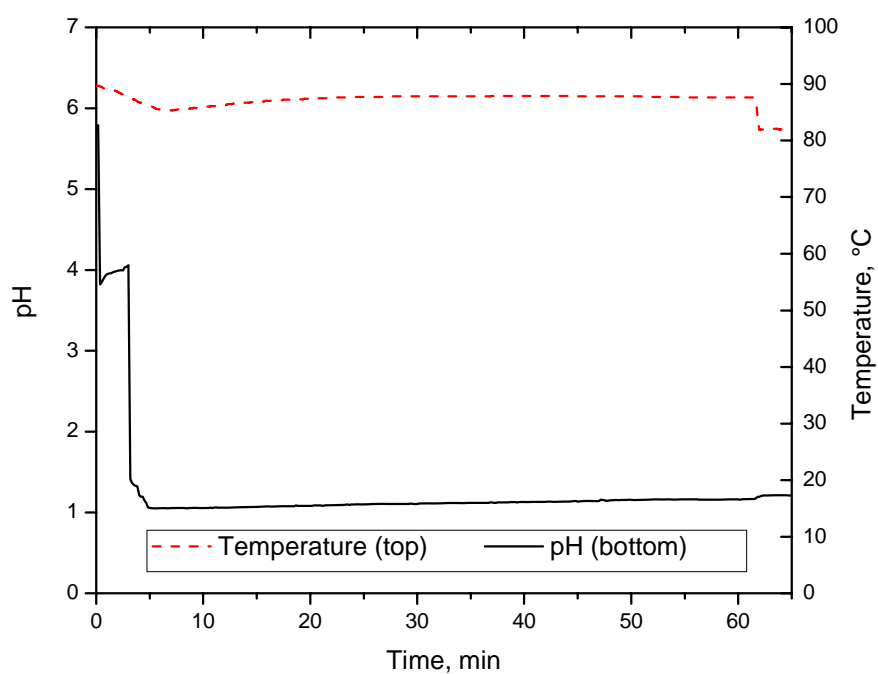


Figure 85: SHS MgO/TiB<sub>2</sub> leaching strip chart for minimum pH 1.0 at 90°C – 2<sup>nd</sup> Cycle

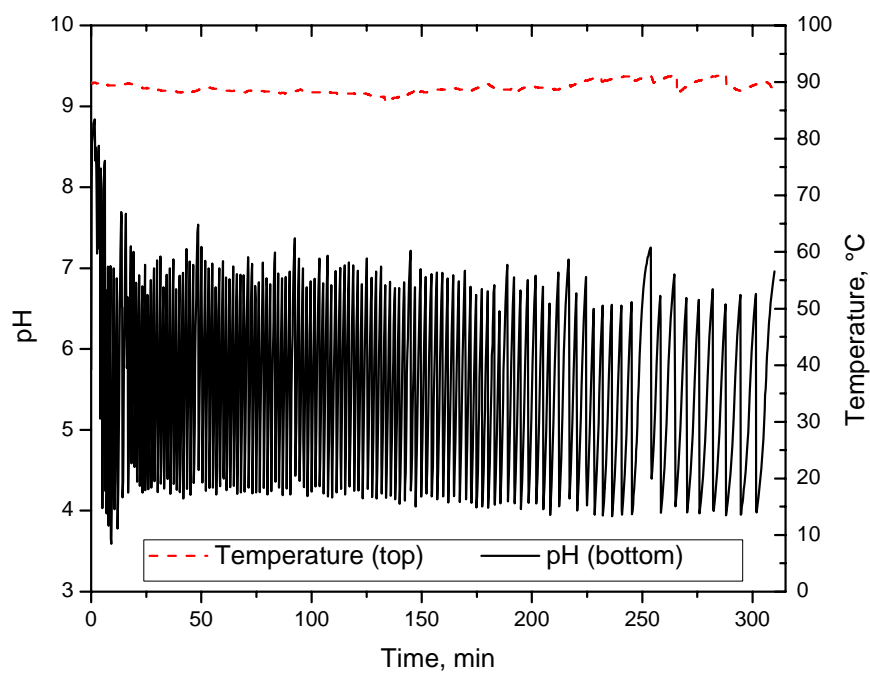


Figure 86: Commercial powder leaching strip chart for minimum pH 4.0 at 90°C

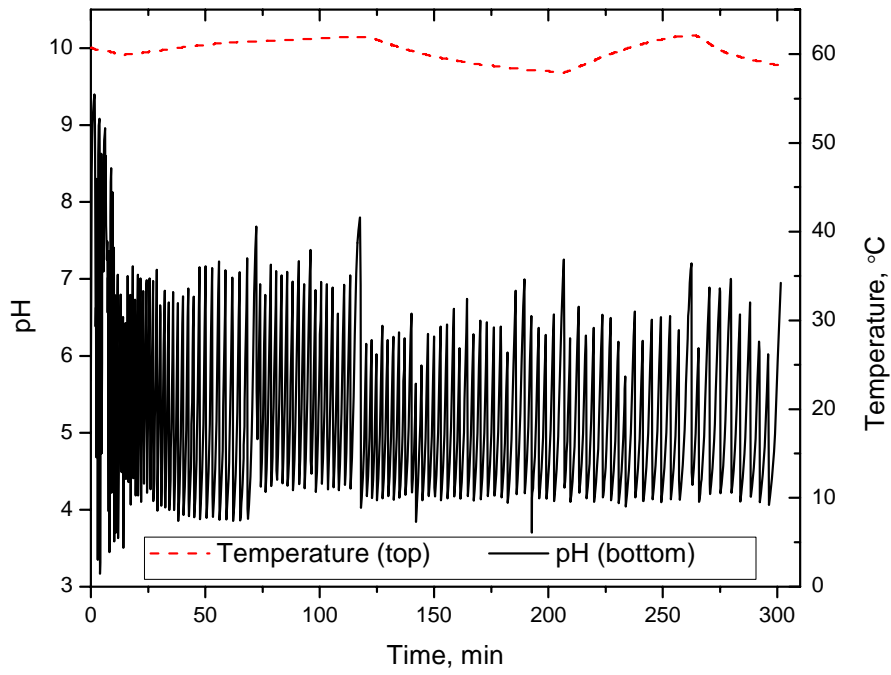


Figure 87: Commercial powder leaching strip chart for minimum pH 4.0 at 60°C

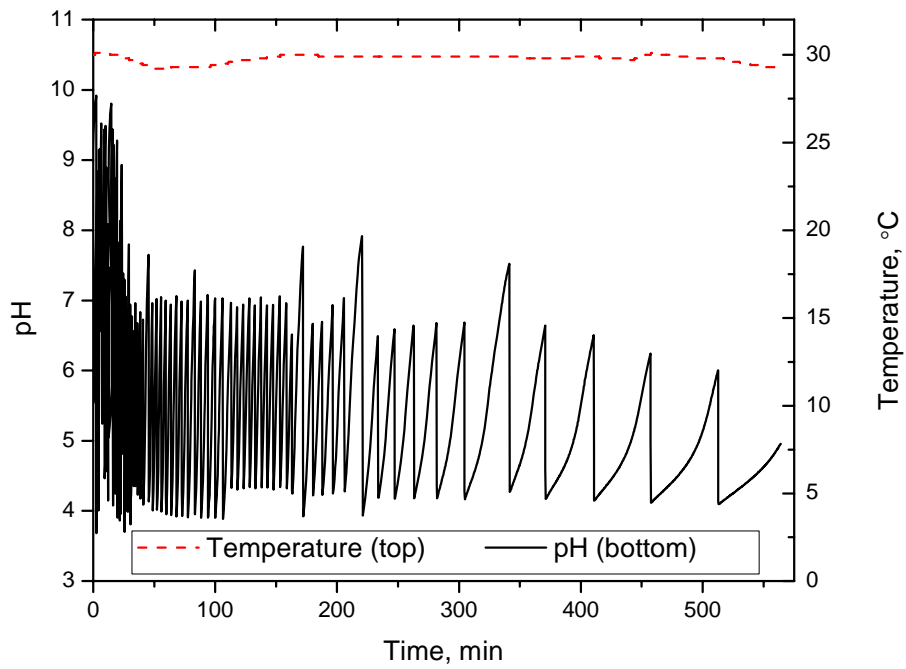


Figure 88: Commercial powder leaching strip chart for minimum pH 4.0 at 30°C

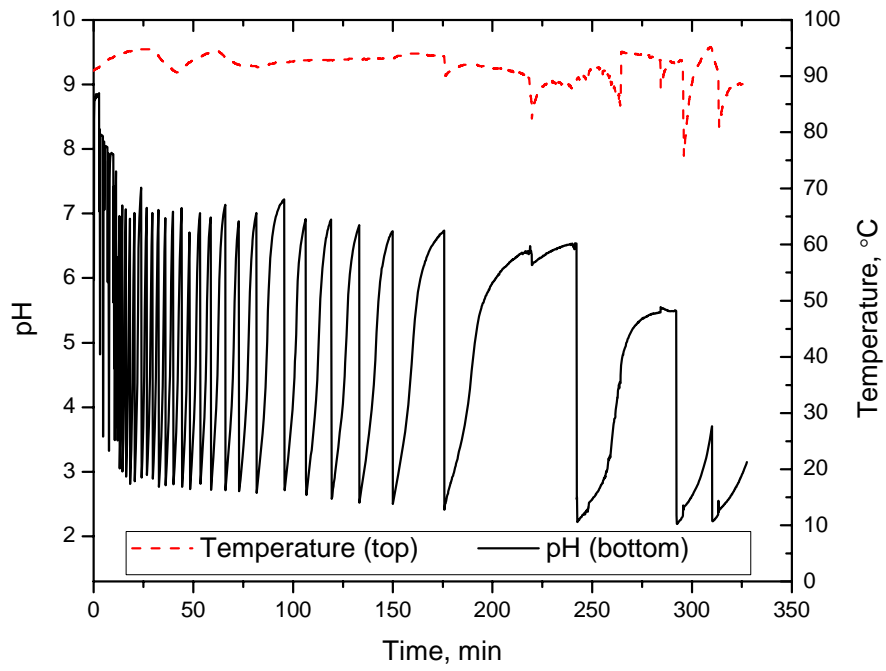


Figure 89: Commercial powder leaching strip chart for minimum pH 2.5 at 90°C

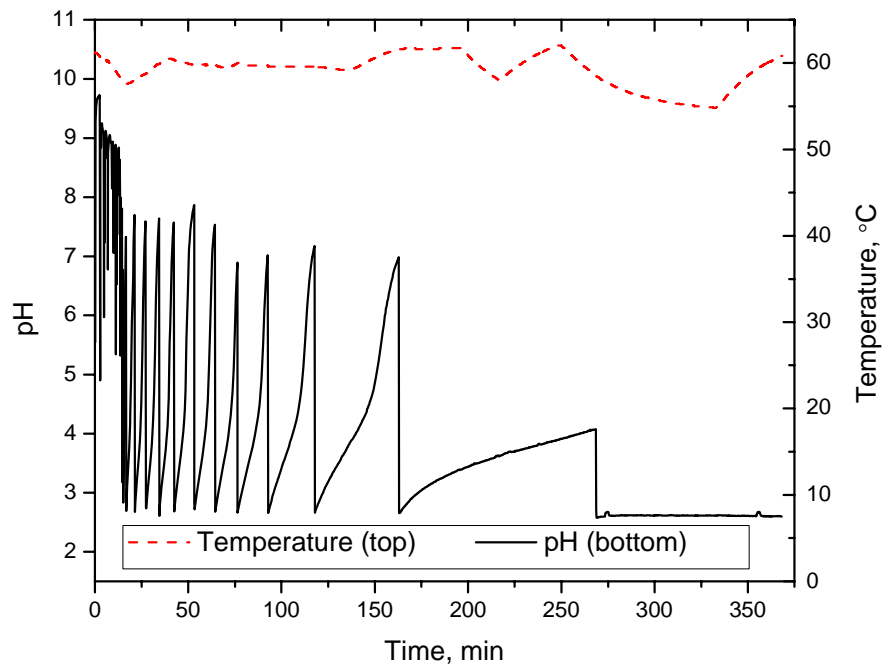


Figure 90: Commercial powder leaching strip chart for minimum pH 2.5 at 60°C

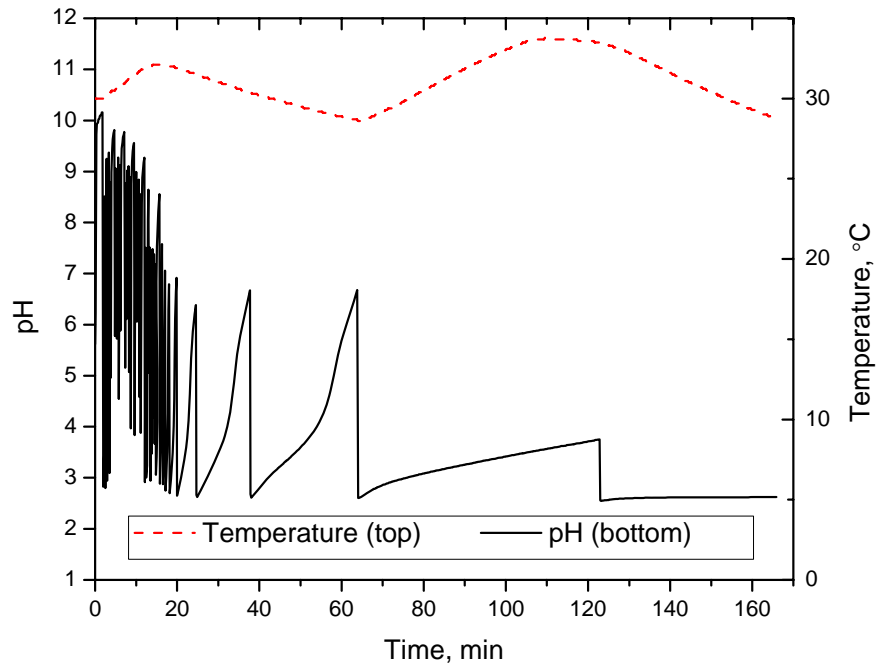


Figure 91: Commercial powder leaching strip chart for minimum pH 2.5 at 30°C

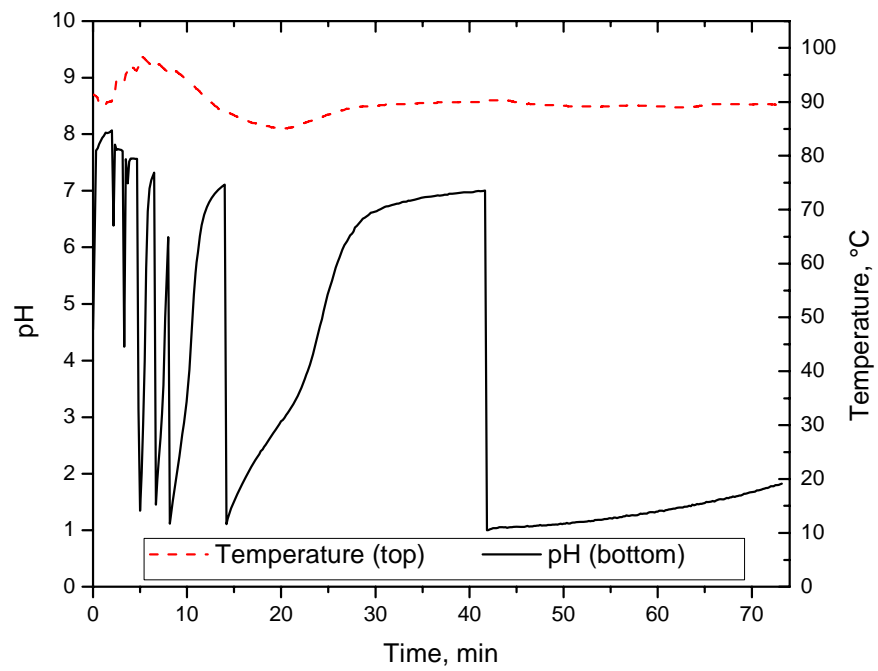


Figure 92: Commercial powder leaching strip chart for minimum pH 1.0 at 90°C

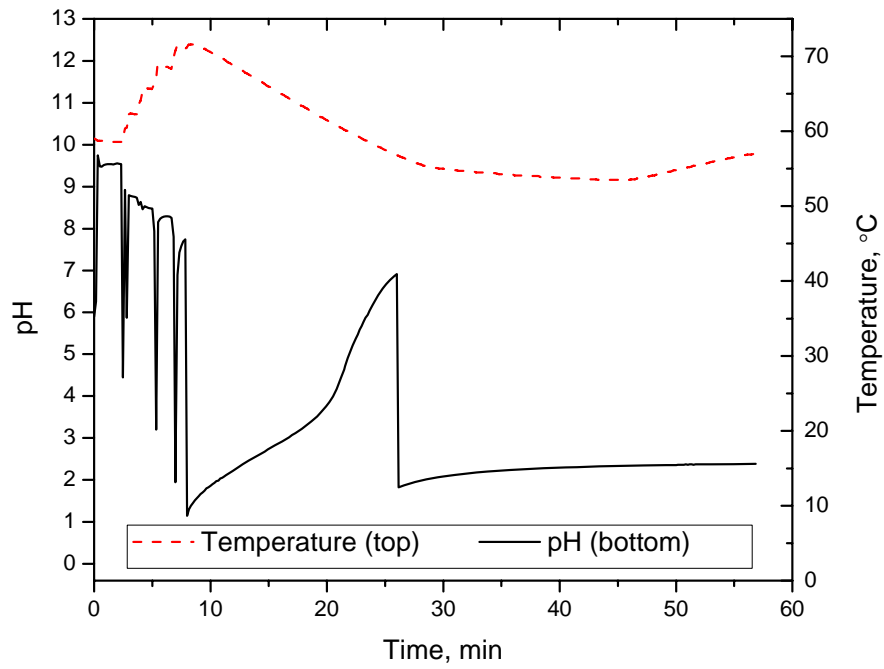


Figure 93: Commercial powder leaching strip chart for minimum pH 1.0 at 60°C

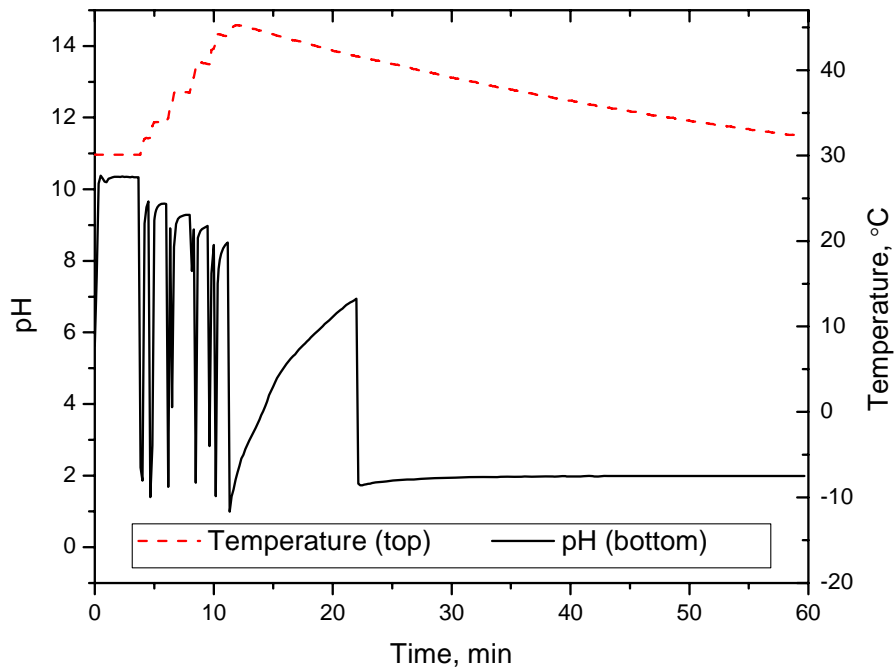


Figure 94: Commercial powder leaching strip chart for minimum pH 1.0 at 30°C

## REFERENCES

1. *CRC Handbook of Chemistry and Physics*. CRC Press, Boca Raton, FL, 2007.
2. Abbe, P.O. Principles of Grinding.
3. Abriou, D. and Jupille, J. Self-inhibition of water dissociation on magnesium oxide surfaces. *Surface Science*, 430 (1-3). L527-L532.
4. Birchall, V.S., Rocha, S.D.F., Mansur, M.B. and Ciminelli, V.S.T. A simplified mechanistic analysis of the hydration of magnesia. *Canadian Journal of Chemical Engineering*, 79 (4). 507-511.
5. Brynestad, J., Bamberger, C.E., Heatherly, D.E. and Land, J.F. Synthesis of Sub-Micron Titanium Diboride Powders. *High Temperature Science*, 19 (1). 41-49.
6. Callister Jr., W.D. *Materials Science and Engineering: An Introduction*. John Wiley & Sons, Inc., 2003.
7. Chen, L.Y., Gu, Y.L., Qian, Y.T., Shi, L., Yang, Z.H. and Ma, J.H. A facile one-step route to nanocrystalline TiB<sub>2</sub> powders. *Materials Research Bulletin*, 39 (4-5). 609-613.
8. Chen, L.Y., Gu, Y.L., Shi, L., Yang, Z.H., Ma, R.H. and Qian, Y.T. A reduction-boronation route to nanocrystalline titanium diboride. *Solid State Communications*, 130 (3-4). 231-233.
9. Dolnik, M., Gardner, T.S., Epstein, I.R. and Collins, J.J. Frequency control of an oscillatory reaction by reversible binding of an autocatalyst. *Physical Review Letters*, 82 (7). 1582-1585.
10. Foster, M., D'Agostino, M. and Passno, D. Water on MgO(100) - An infrared study at ambient temperatures. *Surface Science*, 590 (1). 31-41.
11. Fruhwirth, O., Herzog, G.W., Hollerer, I. and Rachetti, A. Dissolution and Hydration Kinetics of MgO. *Surface Technology*, 24 (3). 301-317.
12. Gaskell, D.R. *Introduction to the Thermodynamics of Materials*. Taylor & Francis, 1995.
13. Gu, Y.L., Qian, Y.T., Chen, L.Y. and Zhou, F. A mild solvothermal route to nanocrystalline titanium diboride. *Journal of Alloys and Compounds*, 352 (1-2). 325-327.
14. Hoekje, H. Submicron Titanium Diboride Powder and Method for Preparing Same. Patent, U.S. ed., PPG Industries, Inc., United States, 1981.
15. Johnson, M.A., Stefanovich, E.V., Truong, T.N., Gunster, J. and Goodman, D.W. Dissociation of water at the MgO(100)-water interface: Comparison of theory with experiment. *Journal of Physical Chemistry B*, 103 (17). 3391-3398.
16. Jones, C.F., Segall, R.L., Smart, R.S.C. and Turner, P.S. Initial Dissolution Kinetics of Ionic Oxides. *Proceedings of the Royal Society of London Series a-Mathematical Physical and Engineering Sciences*, 374 (1756). 141-&.
17. Jordan, G. and Rammensee, W. Dissolution rates and activation energy for dissolution of brucite(001): A new method based on the microtopography of crystal surfaces. *Geochimica Et Cosmochimica Acta*, 60 (24). 5055-5062.
18. Kershaw, M.G. Modernization of the Leaching Circuit at Pasmenco-Metals-Ez. *Hydrometallurgy*, 39 (1-3). 129-145.
19. Kim, J.J. and McMurthy, C.H. TiB<sub>2</sub> Powder Production for Engineered Ceramics. *Ceramic Engineering and Science Proceedings*, 6 (9-10). 1313-1320.

20. Logan, K.V., 2006.
21. Logan, K.V. and Villalobos, G.R. Thermodynamic Behavior of Selected SHS Reactions. *Heat Transfer in Fire and Combustion Systems*, 250. 249-257.
22. Munir, Z.A. Synthesis of High-Temperature Materials by Self-Propagating Combustion Methods. *American Ceramic Society Bulletin*, 67 (2). 342-349.
23. Munro, R.G. Material properties of titanium diboride. *Journal of Research of the National Institute of Standards and Technology*, 105 (5). 709-720.
24. Perry, R.H. and Green, D.W. *Perry's Chemical Engineers' Handbook*. McGraw-Hill, 1997.
25. Raschman, P. Leaching of calcined magnesite using ammonium chloride at constant pH. *Hydrometallurgy*, 56 (1). 109-123.
26. Raschman, P. and Fedorockova, A. Dissolution of periclase in excess of hydrochloric acid: Study of inhibiting effect of acid concentration on the dissolution rate. *Chemical Engineering Journal*, 117 (3). 205-211.
27. Raschman, P. and Fedorockova, A. Study of inhibiting effect of acid concentration on the dissolution rate of magnesium oxide during the leaching of dead-burned magnesite. *Hydrometallurgy*, 71 (3-4). 403-412.
28. Ricceri, R. and Matteazzi, P. A fast and low-cost room temperature process for TiB<sub>2</sub> formation by mechanosynthesis. *Materials Science and Engineering a-Structural Materials Properties Microstructure and Processing*, 379 (1-2). 341-346.
29. Rocha, S.D.F., Mansur, M.B. and Ciminelli, V.S.T. Kinetics and mechanistic analysis of caustic magnesia hydration. *Journal of Chemical Technology and Biotechnology*, 79 (8). 816-821.
30. Saito, T., Fukuda, T., Maeda, H., Kusakabe, K. and Morooka, S. Synthesis of ultrafine titanium diboride particles by rapid carbothermal reduction in a particulate transport reactor. *Journal of Materials Science*, 32 (15). 3933-3938.
31. Samsonov, G.V. *The Oxide Handbook*. IFI/Plenum, New York, 1982.
32. Samsonov, G.V. and Vinitskii, I.M. *Handbook of Refractory Compounds*. IFI/Plenum, New York, 1980.
33. Sangwal, K. Dissolution Kinetics of MgO Crystals in Aqueous Acidic Salt-Solutions. *Journal of Materials Science*, 17 (12). 3598-3610.
34. Sangwal, K. Mechanism of Dissolution of MgO Crystals in Acids. *Journal of Materials Science*, 15 (1). 237-246.
35. Sangwal, K. and Arora, S.K. Etching of MgO Crystals in Acids - Kinetics and Mechanism of Dissolution. *Journal of Materials Science*, 13 (9). 1977-1985.
36. Sangwal, K. and Patel, T.C. Etching Behavior to MgO Crystals in Relation to Chemical-Reactions. *Kristall Und Technik-Crystal Research and Technology*, 13 (12). 1407-1412.
37. Sangwal, K., Patel, T.C. and Kotak, M.D. Kinetics and Mechanism of Dissolution of MgO Crystals. *Journal of Materials Science*, 14 (8). 1869-1876.
38. Shi, L., Gu, Y.L., Chen, L.Y., Yang, Z.H., Ma, J.H. and Qian, Y.T. A convenient solid-state reaction route to nanocrystalline TiB<sub>2</sub>. *Inorganic Chemistry Communications*, 7 (2). 192-194.
39. Subrahmanyam, J. and Vijayakumar, M. Self-Propagating High-Temperature Synthesis. *Journal of Materials Science*, 27 (23). 6249-6273.

40. Sundaram, V., Logan, K.V. and Speyer, R.F. Reaction path in the magnesium thermite reaction to synthesize titanium diboride. *Journal of Materials Research*, 12 (10). 2657-2664.
41. Tielens, F. and Minot, C. DFT study of the water/MgO(100) interface in acidic and basic media. *Surface Science*, 600 (2). 357-365.
42. Walker, J.K. Synthesis of TiB<sub>2</sub> by the Borothermic Carbothermic Reduction of TiO<sub>2</sub> with B<sub>4</sub>C. *Advanced Ceramic Materials*, 3 (6). 601-604.
43. Wang, W.M., Fu, Z.Y., Hao, W. and Yang, R.Z. Chemistry reaction processes during combustion synthesis of B<sub>2</sub>O<sub>3</sub>-TiO<sub>2</sub>-Mg system. *Journal of Materials Processing Technology*, 128 (1-3). 162-168.
44. Welham, N.J. Formation of nanometric TiB<sub>2</sub> from TiO<sub>2</sub>. *Journal of the American Ceramic Society*, 83 (5). 1290-1292.
45. Welham, N.J. Formation of TiB<sub>2</sub> from rutile by room temperature ball milling. *Minerals Engineering*, 12 (10). 1213-1224.
46. Welham, N.J. Mechanical enhancement of the carbothermic formation of TiB<sub>2</sub>. *Metallurgical and Materials Transactions a-Physical Metallurgy and Materials Science*, 31 (1). 283-289.
47. Welham, N.J. and Llewellyn, D.J. Formation of nanometric hard materials by cold milling. *Journal of the European Ceramic Society*, 19 (16). 2833-2841.
48. Zhang, S.C., Hilmas, G.E. and Fahrenholtz, W.G. Pressureless densification of zirconium diboride with boron carbide additions. *Journal of the American Ceramic Society*, 89 (5). 1544-1550.

## **VITAE**

Jonathan Yun-Lum Lok was born in Kuala Lumpur, Malaysia and grew up in Tulsa, Oklahoma. He is a graduate of the University of Oklahoma where he earned his B.S. in Chemical Engineering and minor in Chemistry. Jonathan spent the next three years working for Marathon Oil Corporation as a process engineer, and for Kinder Morgan Inc. as a facilities engineer in West Texas. During his graduate studies at Virginia Tech, Jonathan married Elizabeth Thao Hien Phan on February 25, 2006.